POLITECNICO
MILANO 1863

SCUOLA DI INGEGNERIA INDUSTRIALE
E DELL'INFORMAZIONE

A Study on the Mechanical Behaviour of Ecoflex 00-50 Silicone Elastomer

Master Degree in
Materials Engineering and Nanotechnology

Author: **Jacopo Lavazza**

Student ID: 944618
Supervisor: Claudia Marano
Co-supervisor: Marco Contino
Academic Year: 2020-21

Abstract

Silicone elastomers have attracted considerable attention due to their wide range of applications in biomedical engineering and soft robotics. In this thesis work, an extensive thermo-mechanical characterization of Ecoflex Shore hardness 00-50, a commercially available silicone elastomer, has been carried out. The mechanical behaviour of the material has been characterized performing monotonic and cyclic loading tests, in different states of deformation, i.e. uniaxial tension, pure shear and biaxial tension, at different strain rates and different temperatures. Experimental findings allowed to highlight a time-dependent response of the material and to quantify the contribution of dissipative deformation phenomena to the overall strain energy. The applicability of constitutive equations proposed in literature to model the mechanical behaviour of similar silicone elastomers was verified for the material under study: the monotonic loading behaviour can be properly described for strains lower than 400% in uniaxial tension and pure shear, and up to failure in biaxial tension. The effect of temperature on the mechanical response and, in particular on ultimate stress and strain, has been studied in the range between -40°C and 140°C. Results showed that the material mechanical behaviour is sensitive to temperature, and in particular a decrease of ultimate stress and strain has been observed with increasing temperature. Finally, the data obtained at the various temperatures and strain rates has been used to define a failure envelope, a concept already proposed in literature for other elastomers and useful to predict the material ultimate stress and strain in any loading condition.

Keywords: Ecoflex Silicone Elastomer, Mechanical Behaviour, Deformation States, Constitutive Model, Temperature Effects.

Abstract in Lingua Italiana

Gli elastomeri siliconici attraggono sempre maggiore interesse in relazione al loro impiego in campo biomedicale e nella "soft robotics". In questo lavoro di tesi, è stata effettuata un'ampia caratterizzazione termo-meccanica del materiale Ecoflex con durezza Shore 00-50, disponibile in commercio. Il comportamento meccanico del materiale è stato caratterizzato attraverso prove di carico monotono e ciclico, in diversi stati di deformazione, ovvero trazione uniassiale, puro taglio e trazione biassiale, a differenti velocità di deformazione e diverse temperature. I risultati sperimentali hanno messo in risalto la dipendenza dal tempo della risposta del materiale ed hanno permesso di quantificare il contributo legato a fenomeni dissipativi dell'energia di deformazione. L'applicabilità di equazioni costitutive, proposte in letteratura per modellare il comportamento meccanico di elastomeri simili, è stata verificata per il materiale considerato: il comportamento a carico monotono viene descritto correttamente fino a deformazioni del 400% in trazione uniassiale e puro taglio, e fino a rottura in trazione biassiale. L'effetto della temperatura sulla risposta meccanica e, in particolare, su sforzo e deformazione a rottura del materiale, è stato studiato nell'intervallo da -40°C a 140°C. I risultati mostrano che il comportamento meccanico del materiale è sensibile alla temperatura, ed in particolare si osserva una progressiva diminuzione di sforzo e deformazione a rottura all'aumentare della temperatura. Infine, i dati ottenuti a varie temperature e velocità di deformazione sono stati utilizzati per definire un "failure envelope", concetto già proposto in letteratura per altri elastomeri e usato per prevedere sforzo e deformazione a rottura in una qualsiasi condizione di sollecitazione.

Parole chiave: Elastomero Siliconico Ecoflex, Comportamento Meccanico, Stati di Deformazione, Modello Costitutivo, Effetti della Temperatura.

Contents

List of Figures

List of Tables

1 | Introduction

Silicone elastomers have seen an increasing interest in applications fields such as soft robotics and biomedical engineering, thanks to their unique mechanical and physical properties. Although the chemical structure of most commercially available silicones is very similar, the crosslinking mechanism, reinforcement method and ultimately their mechanical properties strongly differ. Modelling the material response is therefore crucial to predict its mechanical behaviour and subsequently to exploit it in suitable applications. In order to obtain a constitutive relation, an extensive mechanical study of the material is to be performed.

Among this class of materials, Ecoflex products have become relevant due to their high extensibility, low stiffness and biocompatibility, in applications like flexible sensors and as substrates in the mechanobiology field. In particular, Ecoflex Shore hardness 00-30 has been extensively studied in order to understand the effects of time and temperature, cyclic loading and different deformation states on its mechanical behaviour, and in order to obtain a constitutive model for the material.

Ecoflex polymers of different Shore hardness, have been studied in a much more limited way, often assuming that their behaviour will be somewhat similar to that of Ecoflex Shore 00-30.

The aim of this thesis project is to provide an in-depth study on Ecoflex Shore 00-50 mechanical behaviour, starting from already available observations present in literature and including missing information such as the effect of different deformation states and of temperature on the material response. The data obtained during this experimental work will be used to model the constitutive relation of the material in the future.

The manuscript is structured as follows:

In **Chapter 2**, a brief overview of silicone elastomers structure, properties and applications is provided. Subsequently, a recall of solid mechanics basic concepts which will be used thoroughly during the work, is introduced. Finally, a general description of elastomers mechanical behaviour and a focus on Ecoflex materials are reported.

In **Chapter 3**, the material and experimental methods used in this work are reported. Preliminary structural characterization of Ecoflex Shore 00-50 and studies on Digital Image Correlation analysis are also provided in this chapter.

In **Chapter 4**, the experimental results are described and discussed in relation to already available data present in literature.

In **Chapter 5**, the main conclusions of this experimental work and some possible future developments are discussed.

2 | Theoretical Background

2.1. Overview of Silicone Elastomers

The term "elastomer" generally identifies a material showing rubber-like behaviour, which satisfies the following conditions [1]:

- High molecular weight (typically polymeric) with a glass transition temperature (T_g) below room temperature;
- Amorphous or negligibly crystalline in the unstrained state;
- Weak inter-chain interactions present between the polymer chains;
- Presence of crosslinking, either chemical or physical.

The term is derived from “elastic polymer”, which comes from the material ability to undergo large elastic strains, i.e. stretch and return to the original configuration in a reversible way [2].

Among this class of materials, polysiloxanes (or silicone elastomers) have seen an increasing interest due to their unique properties such as extremely low glass transition temperature (usually below -120°C), outstanding thermal stability (typically in the temperature range from -50°C to 250°C), high hydrophobicity, chemical resistance and biocompatibility. Furthermore, silicones are typically characterized by large stretchability and low stiffness, closely matching those of compliant biological tissues [3, 4, 5].

This set of properties led to a variety of applications such as tubes, pumps and catheters in biomedical engineering, in mechanobiology as substrates and for the impregnation of fabric tapes [5]; as actuators and sensors in soft robotics and flexible electronics [6]; and as gaskets, diaphragms and sealants in the aerospace and automotive industries [7].

Silicones consist of $(Si - O)$ chains, with two monovalent organic radicals (R_1 and R_2) bonded to each silicon atom, as shown in Figure 2.1. The most widespread silicone is Poly-(dimethylsiloxane) or PDMS, where the radicals R_1 and R_2 are methyl groups $-(CH_3)$. In order to obtain a silicone elastomer a crosslinking reaction is required [8].

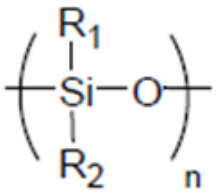

Figure 2.1: General structure of the silicone backbone.

According to the crosslinking process, silicones are divided into two main categories: RTV and HTV, in which the crosslinking occurs at room or at higher temperature respectively. The main features of the two classes are here reported:

- **Room Temperature Vulcanization** (RTV): the crosslinking reaction occurs at room temperature and involves the interaction of a crosslinking agent with the siloxanol terminal groups of each chain, in presence of a catalyst. One-component and two-component systems are commercially available and are usually in the liquid state. In the first case, the system consists of a mixture of all the components, and the reaction is triggered by humidity in the environment. In two-component systems, instead, a prepolymer (oligomeric chains that act as precursor) with filler (typically silica), have to be mixed with a crosslinker and catalyst (usually platinum based) containing component. The mixture then has to be stirred before the crosslinking reaction starts. The main advantage of this configuration compared to single component system are shorter curing times, easier processing and the absence of byproducts, even if the presence of Pt-based catalysts greatly increases the price of products [9]. A sketch of the RTV crosslinking process is shown in Figure 2.2.
- **High Temperature Vulcanization** (HTV): the crosslinking reaction arises from peroxides decomposition at around 150°C to create hydrogen and vinyl group radicals. In the first case, H* radicals are abstracted from the methyl group of PDMS and form reactive silymethyl radicals ($SiCH_2^*$), which undergo a crosslinking reaction; in the second method, vinyl groups are used to form a crosslinked network, being more reactive towards H* subtraction. The two processes are very similar and both lead to the formation of byproducts which need to be removed, although the first one is usually more efficient [9].

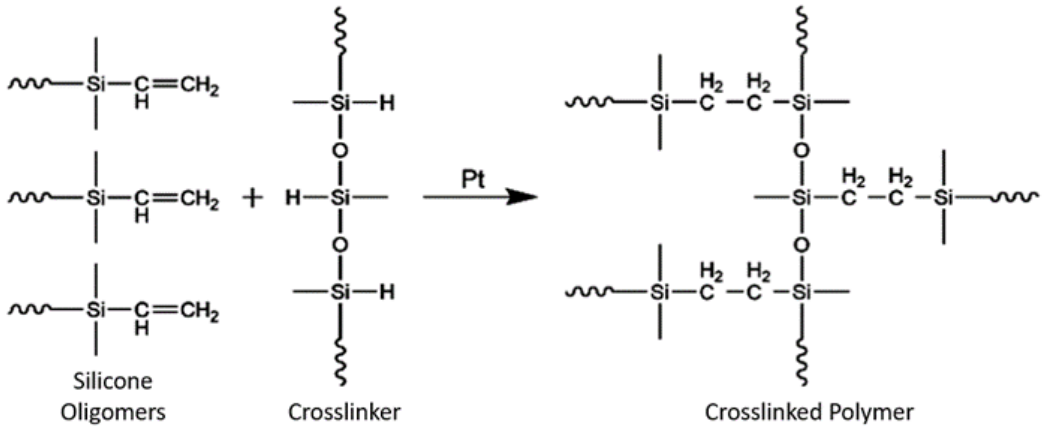

Figure 2.2: Pt catalysed addition reaction (silylation) of telechelic threefunctional polymers with a highly functional crosslinker with three remaining reaction sites [8].

A critical aspect of silicone elastomers concerns their relatively poor mechanical properties (even after crosslinking), compared to other elastomers [4]. Filler reinforcement is employed to obtain better mechanical performances, while preserving optical transparency and other important properties, such as biocompatibility and chemical resistance. Due to the strong filler-polymer interactions through hydrogen bonding between silanols on the filler surface and oxygen atoms in the polymer chain [9, 10], silica is the most used filler in this field.

The hydrodynamic effects arising from the inclusion of rigid particles in a soft matrix, lead to a great increase of the modulus of the compounded silicone elastomer. Furthermore, in the case of active fillers (such as silica in silicones), the filler-polymer interaction leads to an increase of the effective degree of crosslinking [2, 10].

The use of reinforcing filler, however, also carries some disadvantages: the filler particles aggregate tend to agglomerate due to very strong filler-filler interactions, and this can cause the loss of optical transparency, non-homogeneous properties of the final compound (i.e. anisotropy in the mechanical response of the material) and loss of biocompatibility; furthermore, incorporation of large fractions of fillers can affect energy dissipation of the polymer [10].

Although all silicone elastomers have very similar chemistry, the crosslinking mechanism and density, reinforcement method and ultimately their mechanical behaviour strongly differ. Therefore, an extensive mechanical characterization is needed to correctly understand each material mechanical response, in order to be exploited in its best application.

2.2. Recall of Solid Mechanics

2.2.1. Stress and Strain

The mechanical behaviour of a solid is analytically described as the relation between the applied deformation, or strain, ϵ and the reactive force acting across the unit area, called stress σ. The stress/strain state of an elementary volume must be expressed by the second order symmetric tensor components, which are represented in Figure 2.3.

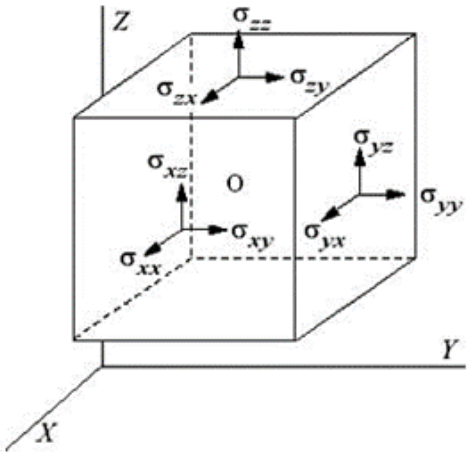

Figure 2.3: Elementary cube with stress tensor components representation.

The general stress and strain tensor definition are reported below:

$$\bar{\bar{\sigma}} = \begin{bmatrix} \sigma_{xx} & \tau_{xy} & \tau_{xz} \\ \tau_{xy} & \sigma_{yy} & \tau_{yz} \\ \tau_{xz} & \tau_{yz} & \sigma_{zz} \end{bmatrix} \tag{2.1}$$

$$\bar{\bar{\epsilon}} = \begin{bmatrix} \epsilon_{xx} & \gamma_{xy} & \gamma_{xz} \\ \gamma_{xy} & \epsilon_{yy} & \gamma_{yz} \\ \gamma_{xz} & \gamma_{yz} & \epsilon_{zz} \end{bmatrix} \tag{2.2}$$

Thanks to tensor properties with respect to rotation of the refence system, it is always possible to find an orthogonal reference system with respect to which the shear components (τ_{ij} and γ_{ij}) are null. The axis of this reference system are called principal and indicated with $i = 1, 2, 3$. The two tensors assume the following form:

$$\bar{\bar{\sigma}} = \begin{bmatrix} \sigma_1 & 0 & 0 \\ 0 & \sigma_2 & 0 \\ 0 & 0 & \sigma_3 \end{bmatrix} \tag{2.3}$$

$$\bar{\bar{\epsilon}} = \begin{bmatrix} \epsilon_1 & 0 & 0 \\ 0 & \epsilon_2 & 0 \\ 0 & 0 & \epsilon_3 \end{bmatrix} \tag{2.4}$$

Referring to the undeformed configuration, it is possible to define the stress tensor principal components as the ratio between the force F_i acting on the i-th face of the elementary volume, and the undeformed cross-sectional area A_{i0}. This is called engineering (or nominal) stress and can be evaluated as:

$$\sigma_i = \frac{F_i}{A_{i0}} \tag{2.5}$$

Strains with respect to the undeformed configuration are expressed as the ratio between the variation in length in the i-th direction ΔL_i and the corresponding undeformed length L_{i0}. This is called engineering (or nominal) strain and is evaluated as:

$$\epsilon_i = \frac{\Delta L_i}{L_{i0}} = \frac{L_i - L_{i0}}{L_{i0}} \tag{2.6}$$

When dealing with elastomers, draw ratios (or stretches) are often used instead of strains. They are defined as the ratio between the deformed length L_i and the corresponding undeformed length:

$$\lambda_i = \frac{L_i}{L_{i0}} = \epsilon_i + 1 \tag{2.7}$$

When dealing with finite strains (as it is often the case with elastomers) this description is no more accurate, due to the reduction of cross sectional area and strong change of current length. In this case the true (or Cauchy) stress and true (or Hencky) strain tensors are commonly used, both referring to the current configuration [11].

In the case of constant volume deformations, it is possible to show that engineering and true stress measures can be related as follows:

$$\sigma_{t,i} = \lambda_i \sigma_i \tag{2.8}$$

Whereas, engineering and true strain measures are always related as:

$$\epsilon_{t,i} = \ln(\epsilon_i + 1) \tag{2.9}$$

Incompressible elastomers have the peculiarity of deforming without changes in volume, and this property can be expressed considering a cube wiht edge length l_0 which deforms into a parallelepiped with edge lengths l_1, l_2 and l_3 and by equating volumes and applying definition (2.8) we obtain:

$$l_1 l_2 l_3 = l_0^3 \tag{2.10}$$

$$\frac{l_1 l_2 l_3}{l_0^3} = 1 \tag{2.11}$$

$$\lambda_1 \lambda_2 \lambda_3 = 1 \tag{2.12}$$

2.2.2. Deformation States

During this thesis work, some specific test configurations will be often referred to and will be briefly described in the following, assuming constant volume deformations (i.e. equation (2.12) is valid) and plane stress conditions (i.e. the stress in the thickness direction, σ_3, is null).

The state of simple or uniaxial tension (***UT***) is such that the elementary volume is deformed along one principal direction and left free to contract in the other two. In terms of draw ratios this is described by:

$$\begin{cases} \lambda_1 = \dfrac{L}{L_0} = \lambda \\ \lambda_2 = \lambda_3 = \lambda_t = \dfrac{1}{\sqrt{\lambda}} \end{cases} \tag{2.13}$$

The state of pure shear deformation (***PS***), is a particular case of biaxial tension (***BT***). It can be defined as "constrained tension" [11], meaning a state of uniaxial tension in which one of the two transverse directions is constrained and forced not to change in length, or in terms of draw ratios:

$$\begin{cases} \lambda_1 = \dfrac{L}{L_0} = \lambda \\ \lambda_2 = 1 \\ \lambda_3 = \dfrac{1}{\lambda} \end{cases} \tag{2.14}$$

The reason behind the name "pure shear" is that "shear" refers to a state of deformation in which parallel lines to one of the principal axes do not change in length, and this is the case along direction 2. The prefix "pure" indicates that principal axis do not rotate during the deformation [11].

From the measured stress in the first principal direction, it is possible to determine the equivalent shear stress in the equivalent simple shear (***SS***) state [1]: this deformation state is represented by the sliding of planes which are parallel to a given plane (the plane of shear) through a distance proportional to their distance from a given plane [11].

This is a constant volume deformation, independently of the incompressibility of the material. In terms of draw ratios, this state is equal to pure shear (eq. (2.14)) while the amount of shear is measured by the tangent of the angle ϕ, which indicates how much a vertical edge of the elementary volume is tilted during the deformation, and it can be related to the shear deformation γ, and the principal stretches:

$$\gamma = \tan\phi = \lambda - \frac{1}{\lambda} \tag{2.15}$$

The shear strain is related to the shear stress τ via a proportionality constant called "shear modulus" G, through the following relationship:

$$\tau = G\gamma \tag{2.16}$$

Considering the work of deformation, it can be proven that in ***PS*** the only work done is that of the stress σ_1, whereas for ***SS*** the work is done by the shear stress τ. For an infinitesimal deformation this means:

$$dW_{PS} = \sigma_1 d\lambda_1 \tag{2.17}$$

$$dW_{SS} = \tau d\gamma \tag{2.18}$$

The two expressions must be equal and by introducing the definition of Eq. (2.15), we

obtain:

$$\tau = \frac{\sigma_1 \lambda_1^2}{1 + \lambda_1^2} \tag{2.19}$$

Plotting the shear stress in function of the equivalent shear strain (see Figure 2.4), we obtain a curve which follows the theoretical linear trend (i.e. Eq. (2.16)) up to $\gamma = 1$, whereas for larger deformations the curve falls below the theoretical prediction. The slope of the linear region corresponds to the shear modulus.

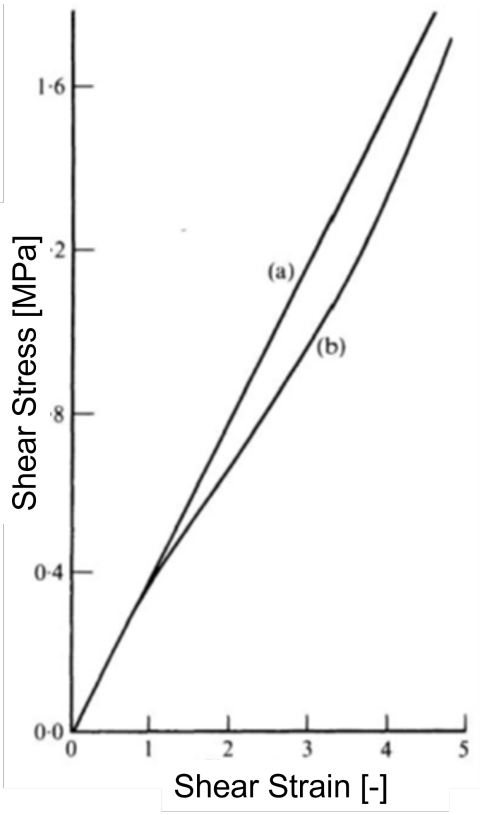

Figure 2.4: Simple shear plot, with theoretical (a) and equivalent (b) trends [1].

The final deformation state worth mentioning is equibiaxial tension (***ET***): in this case two of the three principal strains are equal to each other, whereas the third one can be obtained from Equation (2.12). In terms of draw ratios this means:

$$\begin{cases} \lambda_1 = \lambda_2 = \lambda \\ \lambda_3 = \dfrac{1}{\lambda^2} \end{cases} \tag{2.20}$$

A visual representation of the deformation states illustrated is presented in Figure 2.5:

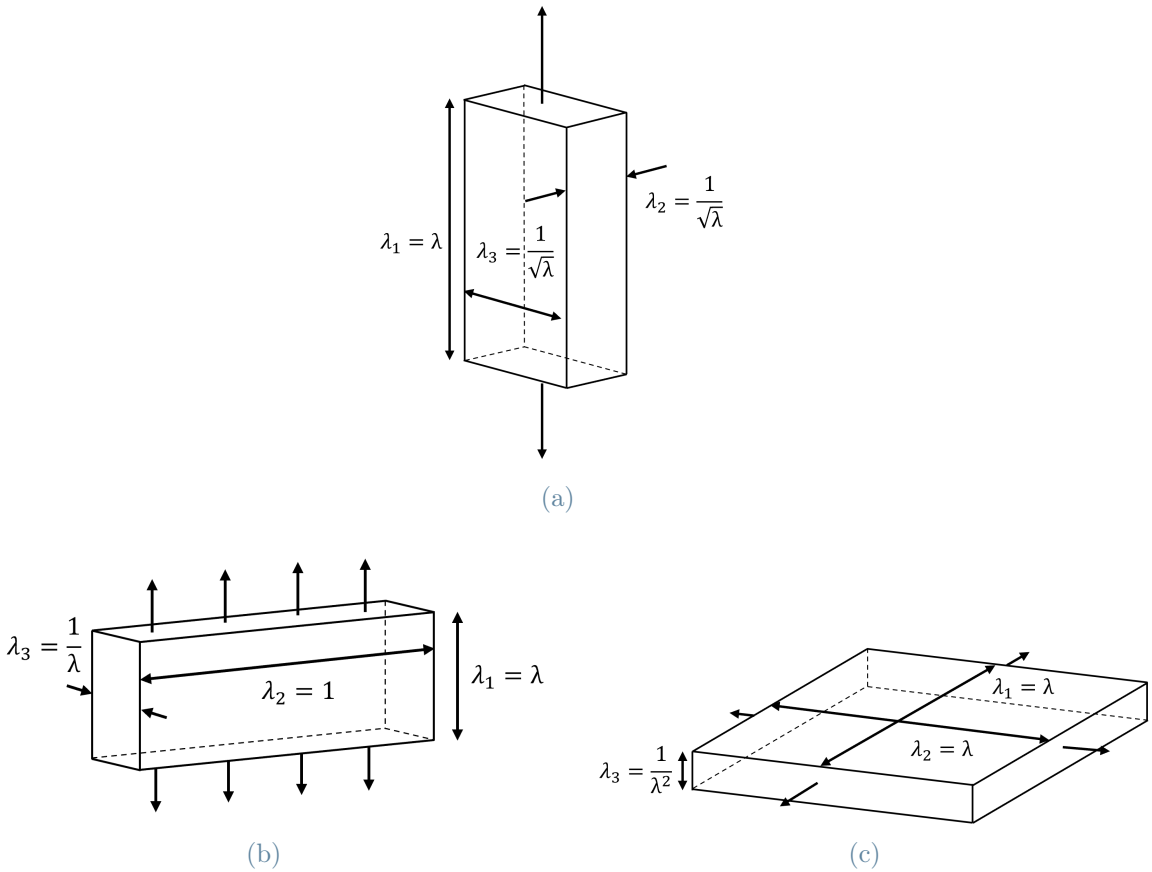

Figure 2.5: Visual representation of a) Uniaxial Tension, b) Pure Shear and c) Equibiaxial Tension deformation states [11].

In order to describe the deformation state by means of a single number, a parameter called Biaxiality (B) can be defined as:

$$B = \frac{\epsilon_1 - \epsilon_2}{\epsilon_1} \tag{2.21}$$

where ϵ_1 and ϵ_2 are the components of the principal engineering strain tensor. To expand on this concept, the Poisson ratio (ν) is introduced: it quantifies the degree of transversal shrinkage (or expansion) that the material experiences during a unidirectional longitudinal extension (or compression), or in mathematical form:

$$\nu = -\frac{\epsilon_2}{\epsilon_1} \tag{2.22}$$

where the longitudinal direction is identified by the first principal direction, while the transverse one coincides with the second principal direction.

This definition is valid only in the linear elastic regime of the material behaviour but can be extended to finite strains knowing the relationship between longitudinal and transverse draw ratios in uniaxial tension, reported in Eq. (2.13) [12]. Therefore, one can express the ratio between the transverse and longitudinal strain as a function of only the longitudinal one:

$$-\frac{\epsilon_2}{\epsilon_1} = \frac{1}{\epsilon_1}\left(1 - \frac{1}{\sqrt{\epsilon_1 + 1}}\right) \tag{2.23}$$

Furthermore, it can be proven that for infinitesimal strains:

$$\lim_{\epsilon_1 \to 0}\left(-\frac{\epsilon_2}{\epsilon_1}\right) = \nu = 0.5 \tag{2.24}$$

which is in accordance with the linear elastic definition of Poisson ratio for incompressible materials. It is possible to represent Eq. (2.23) as shown in Figure 2.6, highlighting two different regions: the upper area characterizes deformations with a volume contraction and the lower one which is associated with an increase in volume during the deformation.

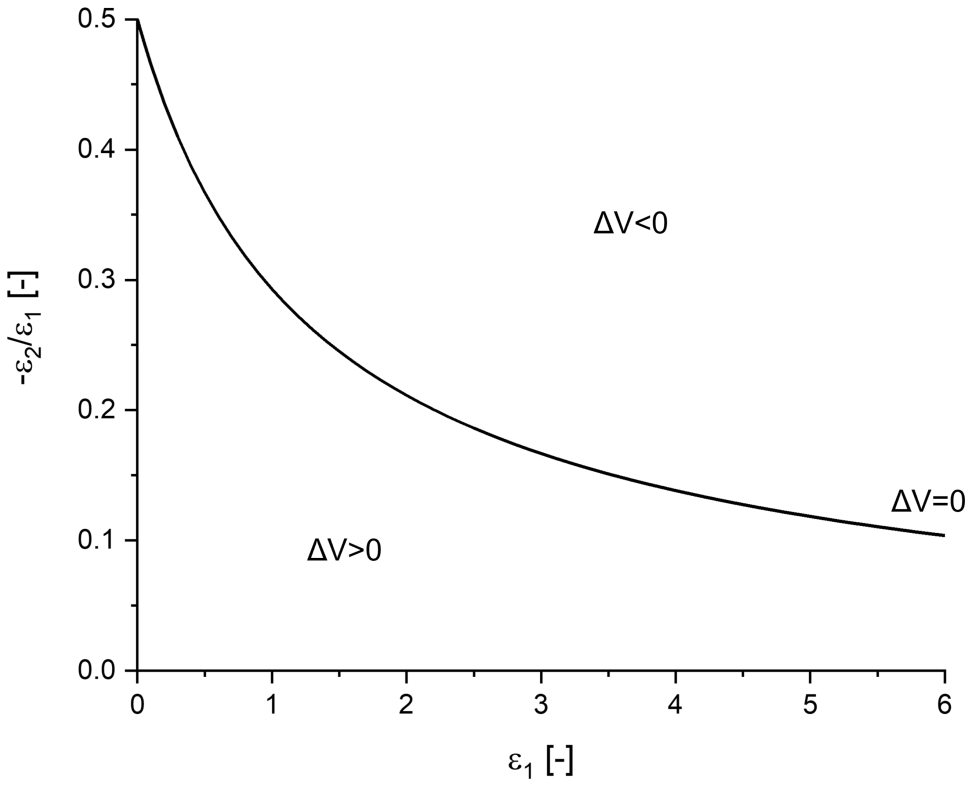

Figure 2.6: Transverse and longitudinal strain ratio versus applied longitudinal strain plot (for UT deformation state).

Combining Eq. (2.21) and (2.23) it is possible to express the Biaxiality for an element subjected to uniaxial tension as a function of the longitudinal strain:

$$B = 1 - \frac{\epsilon_2}{\epsilon_1} = 1 + \frac{1}{\epsilon_1}\left(1 - \frac{1}{\sqrt{\epsilon_1 + 1}}\right) \tag{2.25}$$

From this definition it is possible to see that the biaxiality for ***UT*** is a decreasing function of ϵ_1, which varies between 1.5 (the maximum theoretical value) to 1 (for longitudinal strains tending to infinity).

It is possible to define the Biaxiality also for ***PS*** and ***ET*** deformation states from the relationship between the principal draw ratios, obtaining the following values:

$$B = \begin{cases} (1; 1.5] \; for \; \boldsymbol{UT} \\ 1 \; for \; \boldsymbol{PS} \\ (0; 1) \; for \; \boldsymbol{BT} \\ 0 \; for \; \boldsymbol{ET} \end{cases} \tag{2.26}$$

These boundaries are obtained as a consequence of using engineering strain as deformation measure and to define the Biaxiality coefficient.

2.3. Mechanical Behaviour of Elastomers

2.3.1. Basic Concepts of Hyperelasticity

Elastomers behave mechanically as non-linear viscoelastic isotropic incompressible materials. The origin of this nature directly derives from the properties of the polymer chains and from the structure they form when bound together. The structure of an elastomer is in fact based on long flexible polymer chains interconnected by “bridges” called crosslinks, to form a network through a curing process, which is called "vulcanization" for natural rubber [11]. In the ideal case, this process prevents the relative sliding of polymer chains, allowing for a purely elastic behaviour as shown in Figure 2.7.

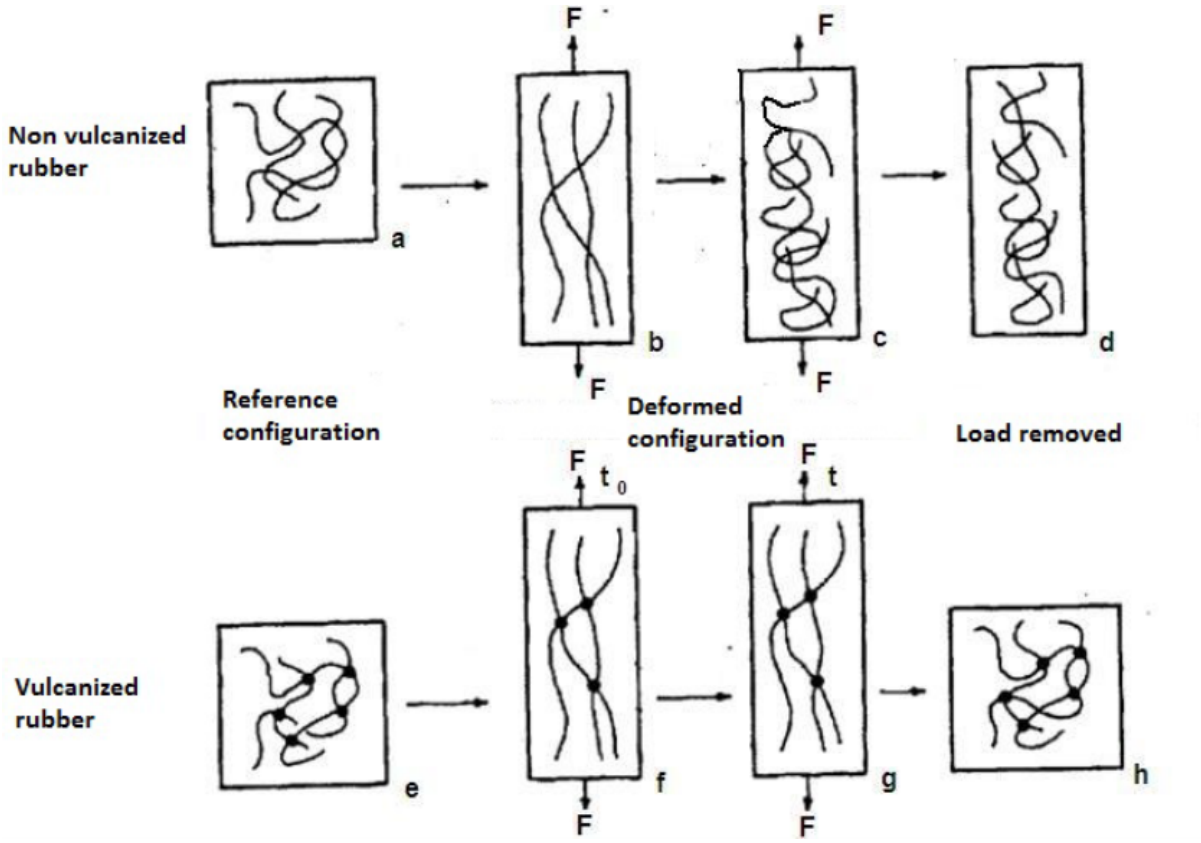

Figure 2.7: Schematic representation of a loading-unloading cycle performed on not crosslinked (top) and crosslinked (bottom) rubber [13].

In order to quantitatively describe the stress-strain behaviour of elastomers, the concept of hyperelasticity must be introduced: a Cauchy-elastic (or simple elastic) material is one in which a bijective relation exists between the stress at each point and the current state of deformation [14]. This means that the stress value depends only on the strain value, but the work of deformation may depend on the deformation path and stress cannot be derived from a scalar potential function. On the other hand, if the material is conservative with respect to the strain energy density (defined in Eq. (4.24)), it is called hyperelastic (or Green-elastic) [14].

The first attempt to describe analytically the problem of elastomers elasticity is Rivlin's theory of large elastic deformations [15]. Considering a **single chain**, its elastic properties can be described starting from statistical thermodynamic considerations about its allowed configurations. The undeformed and highly disordered state is referred to as "random coil" and is described by the average end-to-end distance r_0 (the vector joining the two free ends of the molecule), which increases to r_x once the chain is stretched along the x-direction, as illustrated in Figure 2.8.

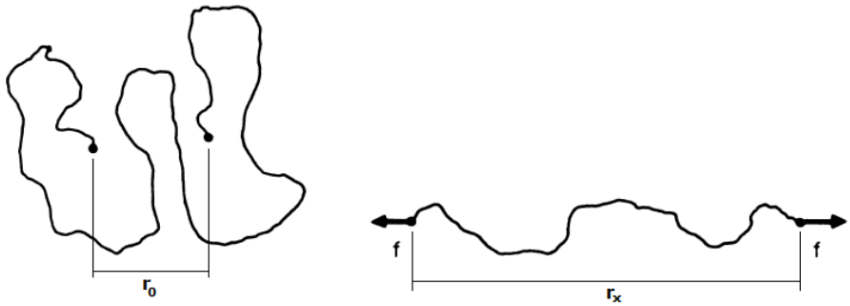

(a) (b)

Figure 2.8: Single polymer chain in a) random coil configuration and b) uniaxially stretched configuration [2].

The chain is described in terms of n freely-rotating rigid sections connected to each other, with a length of l. It can be proven that, for small values of r, the end-to-end distance distribution obeys a gaussian probability function:

$$P(r) = Cexp(-\beta^2 r^2) \tag{2.27}$$

where the factor β^2 is equal to $3/2nl^2$, and r^2 corresponds to the mean square end-to-end distance:

$$r^2 = nl^2 \tag{2.28}$$

The Helmholtz free energy that describes this system (δF) is equal to $-Ts$, where T is the absolute temperature and s is the entropy of the chain, and can be obtained from Boltzmann's law [1, 16]:

$$\delta F = -kTln(P(r)) = kT\beta^2 r^2 = \frac{3kTr^2}{2nl^2} \tag{2.29}$$

where k is the Boltzmann constant. The relationship between the reactive force f arising from a variation in length δr is obtained as follows:

$$f = \left(\frac{\partial \delta F}{\partial r}\right) = \frac{3kTr}{nl^2} = Kr \tag{2.30}$$

It is evident from Eq. (2.30) how a macromolecule following a gaussian distribution, behaves mechanically as an ideal spring described by Hooke's law (which relates stress

and strain through a proportionality constant E, the Young modulus of the material), whose proportionality constant K is linearly dependent on temperature and inversely proportional to the number of sub-chain segments n.

These concepts can be generalized to a **molecular network**, by expressing the Helmholtz free energy of an unitary cube of material as a function of the principal draw ratios. The following hypothesis are made [1, 13, 15]:

1. The network contains N chains per unit volume, being a chain a segment of molecule between two crosslinks.
2. The mean square end-to-end distance in the unstrained configuration (r_0^2) is the same as for a corresponding set of free chains, and is defined by Eq. 2.28.
3. There is no change in volume during deformation (incompressibility).
4. The junction points move as if they are embedded into an elastic continuum upon deformation, resulting in the components of length of each chain changing in the same ratio as the corresponding dimension of the bulk elastomer (affine deformations).
5. The total entropy of the network is the sum of the entropies of the individual gaussian chains.
6. Temperature is constant during the deformation process.

Under these assumptions, it can be shown that the total work of deformation of the network (W) is equal to [1, 16]:

$$W = \Delta F = -T\Delta S \tag{2.31}$$

$$W = \frac{G}{2}\left(\lambda_1^2 + \lambda_2^2 + \lambda_3^2 - 3\right) \tag{2.32}$$

where the shear modulus G is linked to the density of the elastomer ρ, the ideal gas constant R and the average chain molecular weight between crosslinks M_C:

$$G = NkT = \frac{\rho RT}{M_C} \tag{2.33}$$

It is evident how the rigidity of the material is strongly related to the crosslinking density and the temperature, by increasing M_C (i.e. decreasing the crosslinking density) the shear

modulus decreases, whereas by increasing T the stiffness increases.

Equation (2.32) represents the simplest example of hyperelastic strain energy potential and is usually referred to as **Neo-Hookean model**. In the case of uniaxial tension, combining Eq. (2.32) and (2.13), the work of deformation takes the form:

$$W = \frac{G}{2}\left(\lambda^2 + \frac{2}{\lambda} - 3\right) \tag{2.34}$$

The stress-strain relationship for uniaxial tension, can be obtained by derivation of Eq. (2.34) as follows:

$$\sigma = \left(\frac{\partial W}{\partial \lambda}\right) = G\left(\lambda - \frac{1}{\lambda^2}\right) \tag{2.35}$$

The first consequence of this constitutive law is the non-linearity of the mechanical response; making reference to Figure 2.9, it can be seen that the Neo-Hookean model and experimental data show good agreement up to $\lambda \approx 2$, whereas for intermediate stretches ($2 < \lambda < 5$) the theoretical model appears to be stiffer than the real elastomer: this is because an ideal network is assumed during the derivation, while in reality a multitude of defects are present in the material (e.g. dangling bonds, uncured chains, imperfect entanglements etc.). For high strain levels, at $\lambda > 5$, the chains reach their extensibility limit and become more rigid, giving rise to a phenomenon known as upturn or strain hardening; this occurrence cannot be predicted by Rivlin's theory because the ideal model doesn't take into account the finite extensibility of real polymer chains.

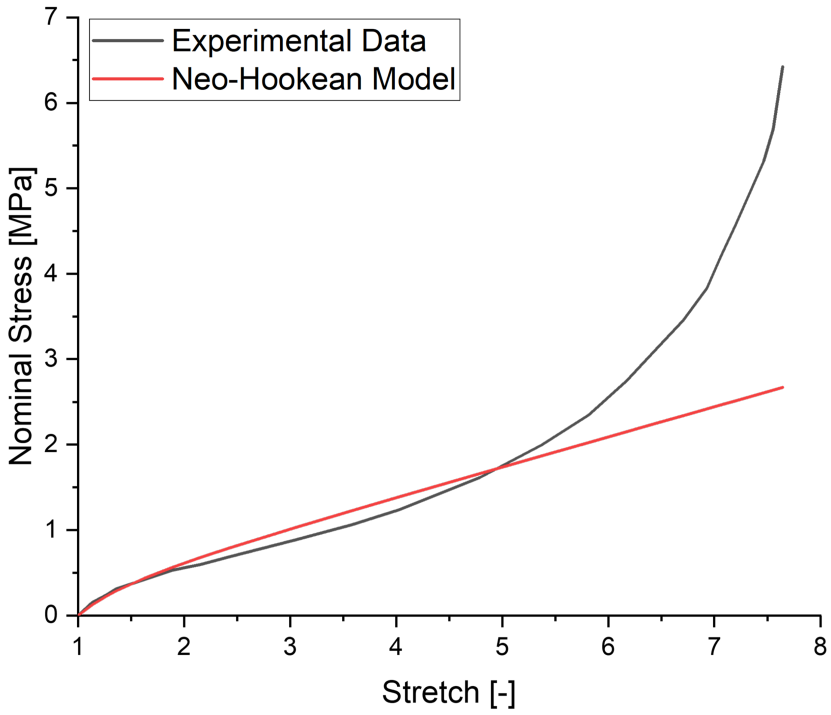

Figure 2.9: Comparison between UT experimental data obtained from [1] and Neo-Hookean model, with $G = 0.35$ MPa.

In order to better describe the mechanical response of elastomers, a series of model has been proposed to address the various shortcomings of the Neo-Hookean model. Among these, the **phenomenological models** are the most commonly found in literature: they are purely mathematical models, aimed at the fitting of experimental data without regard of the physical origin of the phenomenon.

The first ever example of phenomenological model is the **Mooney-Rivlin model**, proposed by Mooney as an improvement of the original Neo-Hookean model, by introduction of two fitting parameters. In this case, the hyperelastic strain energy potential is expressed as [1, 13]:

$$W = C_{10}(I_1 - 3) + C_{01}(I_2 - 3) \tag{2.36}$$

Where C_{10} and C_{01} are material constants which can be experimentally determined , while I_1 and I_2 are the first and second strain invariants, which can be written as function of the principal stretches as:

$$I_1 = \lambda_1^2 + \lambda_2^2 + \lambda_3^2 \tag{2.37}$$

$$I_2 = \lambda_1^2\lambda_2^2 + \lambda_2^2\lambda_3^2 + \lambda_3^2\lambda_1^2 \tag{2.38}$$

It can be shown that, for an incompressible material subjected to uniaxial tension, the stress-strain relationship derived from Eq. (2.36) is:

$$\sigma = \left(2C_{10} + \frac{2C_{01}}{\lambda}\right)\left(\lambda - \frac{1}{\lambda^2}\right) \tag{2.39}$$

It is possible to define a reduced Mooney-Rivlin stress as follows:

$$\sigma^* = \frac{\sigma}{2\left(\lambda - \frac{1}{\lambda^2}\right)} = \left(C_{10} + \frac{C_{01}}{\lambda}\right) \tag{2.40}$$

By plotting Eq. (2.40), the constant C_{10} and C_{01} are obtained respectively as the intercept and slope of the linear fit shown in Figure 2.10. In the case presented, the two constants are $C_{10} = 0.104$ MPa and $C_{01} = 0.117$ MPa. The presence of an inflection point at $1/\lambda \approx 0.2$ is indicative of the upturn present in Figure 2.9 at $\lambda \approx 5$.

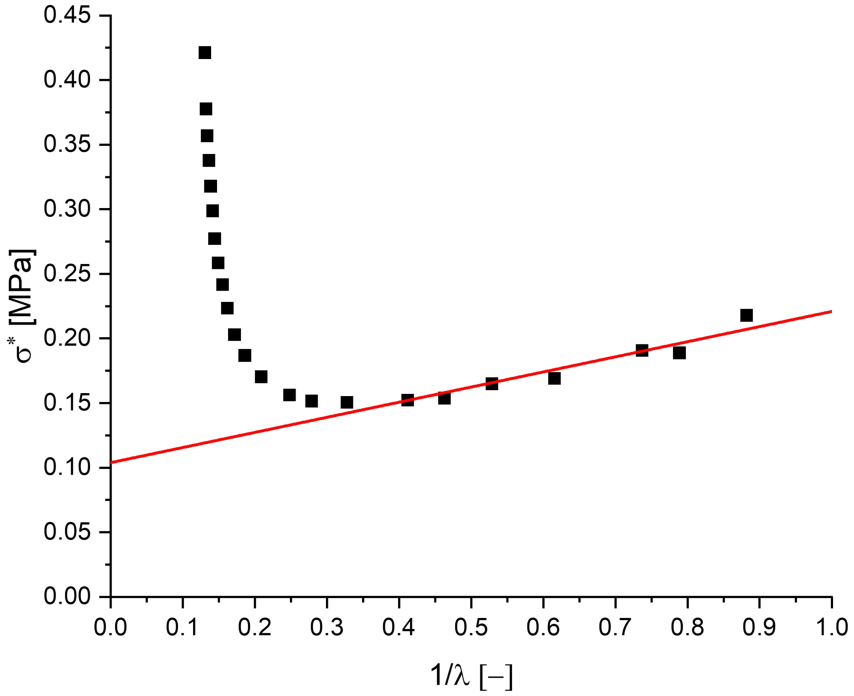

Figure 2.10: Mooney-Rivlin plot of the UT data obtained from [1], with linear fit (in red) of the linear region.

2.3.2. Dissipative Phenomena

Elastomeric materials, both filled and unfilled, show an hysteretic behaviour which is due to dissipative phenomena associated with deformation. These effect can be evaluated from loading-unloading cyclic tests: the area enclosed by the stress-strain curve of the cycle is the dissipated strain energy density of the material. Furthermore, residual strain at the end of unloading is present and, if the material is loaded again, a reduction in the stress, which is often referred to as stress softening or Mullins effect, is observed. These aspects are reported in Figure 2.11.

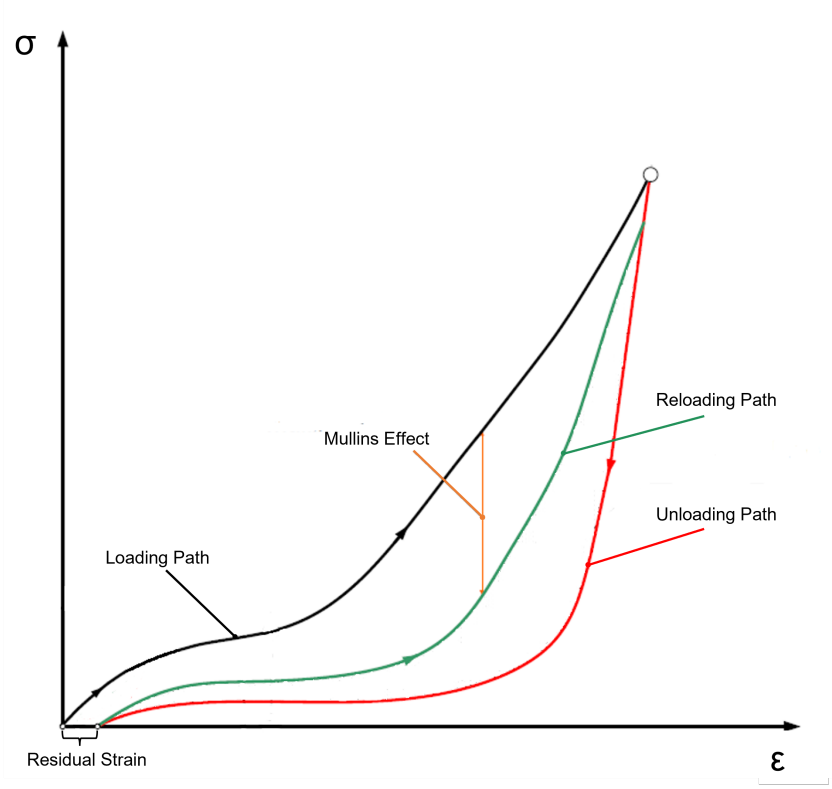

Figure 2.11: Cyclic stress-strain curve, with the principal features highlighted (adapted from [17]).

Hysteresis

Filled elastomers have the ability to dissipate a significant fraction of energy during deformation, as illustrated in Figure 2.12. It is possible to distinguish between two different types of hysteresis: the first or major hysteresis, associated with the first loading-unloading cycle on the pristine material, and the stabilized or minor hysteresis, related to the second cycle or any subsequent one [18].

As well as with the softening effect, a significant reduction of the dissipated energy is observed after the first cycle. After a certain amount of cycles, the material response will become stationary and the hysteresis will remain the same as long as the strain does not exceed the maximum value imposed in the previous cycle [19].

Another feature of this phenomenon, as well as softening, is the dependence of the hysteresis on the amount of filler. In [20], for Styrene Butadiene Rubber (SBR) and Ethylene Propylene Diene Monomer (EPDM) filled with carbon black and silica, an increase of dissipation is observed with increasing filler content. The breakdown and reaggregation of the filler clusters during each cycle is considered to be the main mechanism responsible for hysteresis, because of the stress amplification effect of clusters. Filler-rubber interactions play a fundamental role in softening and dissipation mechanisms.

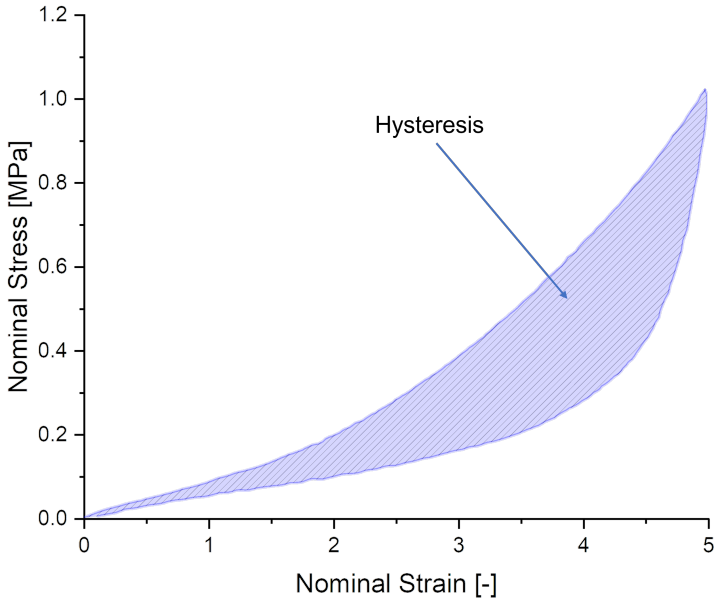

Figure 2.12: Representation of the hysteresis area of Ecoflex 00-50.

The Mullins Effect

Mullins effect refers to the strain induced softening of the rubber compound, detailed in Figure 2.13 [21, 22].

This phenomenon, which is due to a change in the structure of the material with increasing strain, can be summarized by three main effects [23]:

- A lower stress is observed at same applied strain level after the first cycle.
- The softening increases progressively as the maximum stretch is increased.

- The material response becomes stationary after a small amount of repeated cycles at the same extension level.

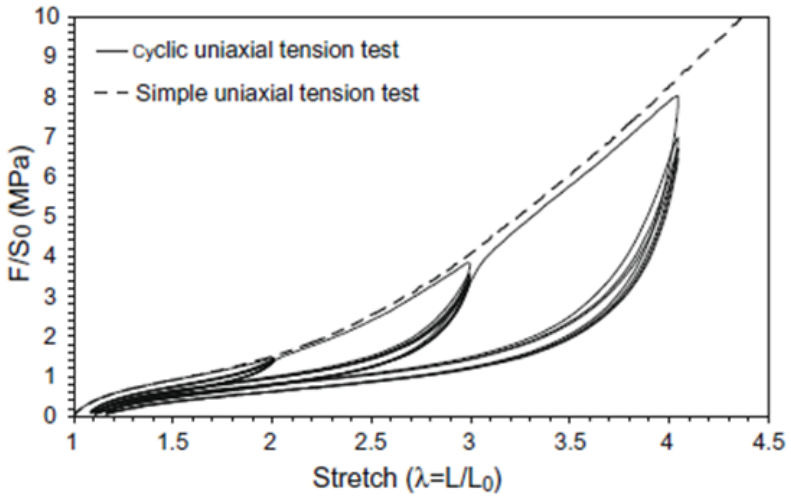

Figure 2.13: Stress–stretch responses of a 50 phr carbon-black filled SBR subjected to monotonic uniaxial tension (dotted line) and to cyclic uniaxial tensle tests (continuous line) with increasing maximum stretch every 5 cycles [23].

Inducing deformation in a polymer network can bring about some alignment and reorientation of chains, leading to anisotropy. After an uniaxial tensile test, the softening is higher along the axis of deformation compared to other directions, being almost negligible in the perpendicular one [24, 25].

The Mullins effect is controlled by the structure of the material: for unfilled elastomers, the material is idealized as a two phase system, with a "hard phase" and a "soft phase": before being subjected to the test, the virgin material only consists of the "hard phase" but, when greater deformation is applied, more and more material degrades to the "soft phase" [22]. In [26], in the case of EPDM, this softening is attributed to the bond scission of chemical crosslinks and main chain bonds of elastomers.

In filled elastomers the phenomenon is even more complex, since also the filler-polymer and filler-filler interactions could play a fundamental role in the Mullins effect: first of all elastomer molecules can slip over the surface of filler particles and reattach elsewhere, because of the applied deformation, causing a change of material entropy and resulting in stress softening, as noted in [23] for rubber vulcanizates filled with carbon black.

In the case of highly filled systems, it is suggested in [27] for carbon black filled rubbers, that the filler tends to form physically connected networks that, upon rupture caused by deformation, may explain the Mullins effect in filled elastomers.

Another possible explanation is attributed in [28], for silica filled PDMS, to the removal of chain entanglements between particles, associated with the strain axis, which is due to chains sliding under each other at filler-rubber interfaces. In this case the number of active chains is assumed constant, while the entanglement density changes with respect to the applied extension. This explanation gives also insight in the mechanism behind induced anisotropy.

One of the most recent theories, reported in [29] for carbon black reinforced elastomers, involves the presence of a double layer structure of rubber (composed of an inner glassy layer and an outer constrained layer) which surrounds the filler spherical particles. During extension, the outer layers are able to connect to each other, forming a so called "super-network" which, during unloading, is not able to hold the stress and it is forced to return to the previous state. The entropic forces of the super-network may be responsible for the Mullins effect.

A summary of the different theories presented is reported in Table 2.1.

Table 2.1: Summary of the different possible mechanisms causing the Mullins effect [26].

Mechanism	Graphical Representation
Bond Rupture [26]	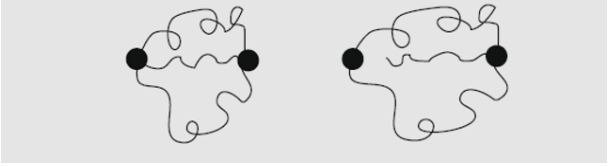
Molecule Slipping [23]	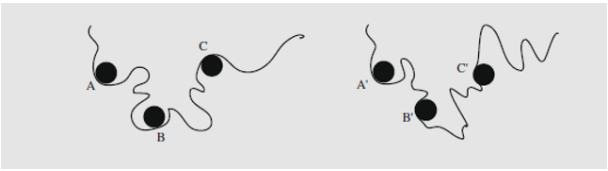
Filler Rupture [27]	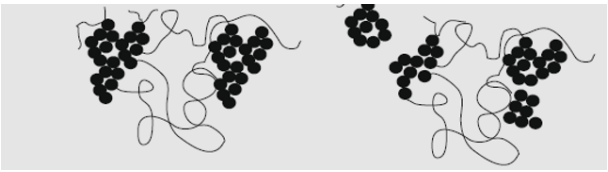
Disentanglement [28]	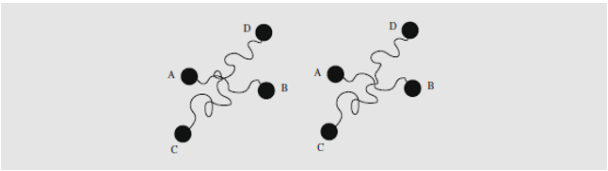
Double Layer [29]	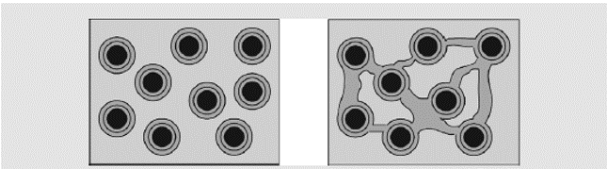

Residual Deformation

The residual deformation, or permanent set, identifies the remaining extension of the material after a loading-unloading test, due to a change in the material structure. The residual deformation is usually present from the first cycle and slightly increases its level in subsequent ones, becoming constant after a few cycles as shown in Figure 2.14. This was not considered in the original description of the Mullins effect [30, 31].

Later studies showed that a relationship exists between residual set and stress softening. Likewise the set is dependent on the applied strain, increasing as the stretch increases (not following a linear relation) [30].

The residual strain is not completely permanent, and, in fact, it continuously decreases with time during a recovery process. It has been shown that an increase of temperature leads to higher recovery rates, highlighting the viscoelastic nature of the process [30, 32]. At the same time a permanent component is present, which is due to permanent changes in the material, such as chain scission [33, 34].

From a structural point of view, in [33, 34], for various rubber vulcanizates, the residual set is considered to be caused by the simultaneous effects of scission and crosslinking of the chains at high temperatures: during stretching, polymer chains are moved from an equilibrium position, promoting scission but at the same time forming new crosslinks which are in equilibrium with the deformed sample. As a consequence, when load is removed, a residual deformation is observed.

It has been shown in [32], in the case of carbon black filled rubbers, that the magnitude of residual set is larger for filled elastomers, compared to nearly negligible values for unfilled ones, and it tends to increase with filler conten.

One possible cause for the set in filled elastomers, is typically assumed to be the anisotropy of filler disposition which results from stretching the material: as a matter of fact, the residual strain also shows an increase with increasing applied extension which lead to higher filler anisotropy. Also shape, size and chemical nature of filler particles have been reported to play a role in the residual strain magnitude [30].

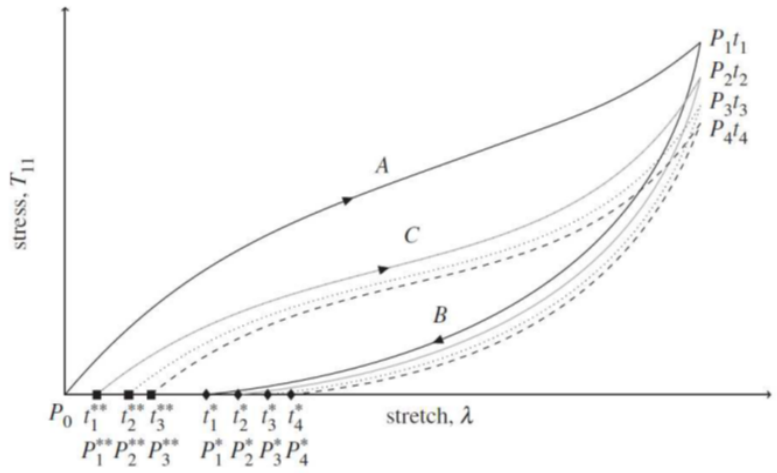

Figure 2.14: Cyclic tests with the presence of residual strain in a filled elastomer [31].

2.3.3. Time and Temperature Effects

Elastomers, being polymeric materials, have a viscoelastic behaviour and thus when it is subjected to a deformation, a contribution of both elastic and viscous responses are involved. The elastic response is instantaneous and contributes to the recovery capability after the stretch is released. The viscous response is the resistance of the material to flow under stress, and it is strain rate and temperature dependent.

Stress relaxation can be observed when a constant stretch is applied, and it is related to various forms of molecular re-adjustments associated with different relaxation times: intra-chain relaxation phenomena takes place at relatively short times, while at longer times inter-chain relaxation can occur [35]. It has been shown that low deformation rates allow a simultaneous short and long-range re-adjustment, reducing the relaxation response at the end of stretching. High deformation rates can limit the re-adjustment of polymer chains, because of the longer relaxation times required for inter-chain relaxation [36]. Also the presence of reinforcing filler particles plays a role on the relaxation behaviour: higher values of stress relaxation are reported for filled elastomers, although a similar time dependence is observed within both filled and unfilled [37]. Relaxation also shows temperature dependence, as one would expect, with an increase in the stress relaxation and relaxation rate when the temperature is increased, due to higher chain mobility [38].

Only a few attempts have been made at understanding the influence of temperature on the mechanical response of filled and unfilled elastomers: first of all it must be emphasized how the filler-rubber and filler-filler interactions decrease with temperature, leading to lower filler reinforcing effect at higher temperatures [39]. As shown in [40] for natural rubber, the

stiffness of the unfilled rubbers depends on temperature in a quasi-linear trend, whereas filled rubbers present a more complex trend, showing a non-linear decrease followed by increase of stiffness with temperature. This complex dependence can be explained by an increase of the entropy-related energy (which explains the linear trend of unfilled, purely entropic elastomers) and a simultaneous decrease in the contribution of enthalpy-related energy (which is associated with the incorporation of filler), with the increase of temperature .

2.4. Literature Review on Ecoflex Mechanical Behaviour

Ecoflex™ elastomers are commercially available RTV silicones, produced by Smooth-On inc., characterized by different Shore hardnesses ranging from Shore 00-10 to Shore 00-65. Due to low viscosity, high biocompatibility and high stretchability, Ecoflex products are ideal candidates for applications in the areas of flexible sensors and biomedical actuation systems.

Within this series of silicone rubbers, the mechanical behaviour of Ecoflex 00-30 has been deeply studied in literature, and in particular in [5] an extensive mechanical investigation was carried out through cyclic loading-unloading tests and single-step relaxation tests.

The material results to be highly hysteretical, characterized by a significant strain-induced stress softening (or Mullins effect) during cyclic loading, as well as by a time-dependent behaviour, as clearly shown in stress relaxation tests. Furthermore, the study highlights that the material hysteretical behaviour is significantly reduced if the material is pre-stretched or undergoes a preliminary relaxation test before a tensile test is performed. It is suggested that this may be caused by material structural changes occurring when the material is deformed, such as chain scission.

In this paper, the approach followed to describe the observed mechanical behaviour is based on the idea that the total strain energy, necessary to deform the material, can be described as sum of an elastic component and a viscous, or dissipative, component. For modelling purposes, the material response is described in terms of stress, which is considered to be the sum of an equilibrium component (associated with the elastic energy component) that is time-independent and of a non-equilibrium one associated with the viscous/dissipative energy component) that, on the contrary, is time dependent. The latter component is null if a loading-unloading cycle or a stress relaxation tests are preliminarly performed. However, it is reported that this stress contribution can be mostly

recovered in long enough periods of time. It was observed that no residual strain is present after the unloading of the material which actually is in contrast with what is reported in [41], where significant residual set was observed for both Ecoflex Shore 00-30 and 00-50. Finally, a very limited strain rate and temperature dependence of the mechanical response was observed in the work present in literature.

In [42], tests similar to the the previously described ones were performed on Ecoflex Shore 00-10, 00-20 and 00-50, and the results were compared to those of Ecoflex 00-30, as shown in Figure 2.15. It was found that all the Ecoflex grades considered have a similar behaviour with respect to time and temperature dependence, and that material stiffness, hysteretical behaviour, the range of time over which stress-relaxation phenomena occur, and strain induced or relaxation induced softening, increase with the increase of Shore hardness.

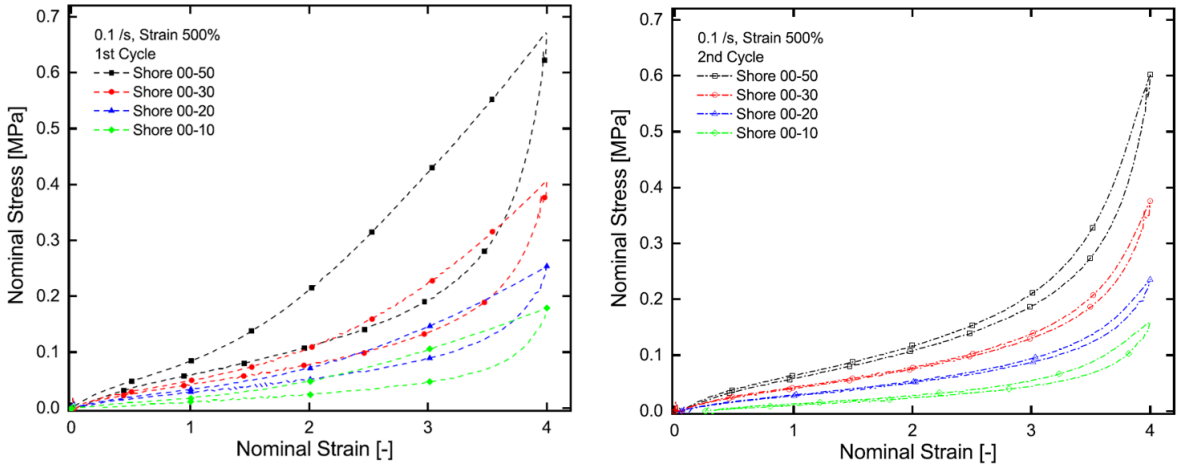

(a) (b)

Figure 2.15: Uniaxial cyclic tensile tests on different Ecoflex rubbers deformed up to 400% imposed strain [42]. a) First cycle and b) second cycle.

The results previously described, although insightful of the mechanical behaviour of Ecoflex materials, are limited to uniaxial tension deformation state; in order to completely describe the material response, other deformation states more resembling of real application conditions, should be tested.

Some preliminary results for pure shear and equibiaxial deformation states are reported in [43], where it is observed that a reduction of the loading Biaxiality (as defined in Eq. (2.21)) causes a larger apparent stress softening and the presence of a residual deformation after unloading, which was not observed in uniaxial tensile tests in [5].

3 | Materials and Methods

3.1. Material Used

The material characterized during this work is Ecoflex™ Shore Hardness 00-50 (from now on, simply referred to as "Ecoflex 00-50") produced by Smooth-On inc.

Ecoflex 00-50 is a RTV silicone elastomer, provided in two liquid parts to be mixed together at room temperature. The crosslinking reaction is catalysed by a Platinum based catalyst. No information is provided by the producer on the chemical structure or on the filler content of the material, but some studies suggest it may be a PDMS elastomer, filled with silica to some extent [7, 41]. These results have been confirmed in this work, through a preliminary characterization of the material whose main results are reported in the following paragraphs, together with the description of the tests that have been performed. Some material properties are reported in Table 3.1.

Table 3.1: Ecoflex 00-50 main properties, as reported in the material data sheet [44].

Property	**Value**	**Normative**
Mixed Viscosity	8000 cps	ASTM D-2393
Density	1.07 g/cm^3	ASTM D-1475
Pot Life	18 $minutes$	ASTM D-2471
Cure Time	3 $hours$	-
Shore Hardness	$00-50$	ASTM D-2240
Tensile Strength	2.15 MPa	ASTM D-412
Tensile Modulus at 100%	0.08 MPa	ASTM D-412
Elongation at Break	980%	ASTM D-412

3.1.1. Specimen Preparation

The two liquid parts were mixed in a 1:1 weight ratio, and thoroughly mixed for 5 minutes with the aid of a mechanical mixer, working at 600 rpm. Afterwards, the mixture was

casted in one half of a mould which was placed for 10 minutes in a vacuum oven at 23°C and at 700 mmHg of pressure, to remove air and therefore minimize bubble presence in the material. Finally, the mould extracted from the vacuum chamber, was closed with the second half of the mould and the material was let to polymerize and crosslink for 3 hours. All the preparation steps were performed at room temperature and the times indicated respect the pot life of the material, corresponding to 18 minutes (see Table 3.1) [44].

The available moulds were optimized for compression moulding, where the material is already in solid state and the mould is used to impart the final shape of the specimen during the final stage of crosslinking; during this thesis work, a new set of male-female moulds was designed, in order to facilitate cast moulding of liquid Ecoflex 00-50. Detailed schematics of the mould geometries and dimensions are reported in Appendix A.

3.1.2. Differential Scanning Calorimetry (DSC)

Differential Scanning Calorimetry (**DSC**) was used to obtain information about the thermal properties of Ecoflex 00-50, such as glass transition (T_g), melting (T_m) and crystallization (T_c) temperatures. The three characteristic temperatures listed above are typically below 0°C in the case of elastomers. In particular, the glass transition temperature represents the lower end use temperature of the material, being the critical temperature at which we observe a transformation from the rubbery to the glassy state of the polymer, losing the elastomeric distinctive properties below this temperature.

DSC analyses were performed on a DSC3 machine by Mettler Toledo, using samples of around 13 mg, obtained from the sheets prepared in the mould. All tests were performed from -140°C (the minimum temperature reachable by the machine) to 30°C, at a rate of 20°C/min and in nitrogen atmosphere. The output of the analysis, known as thermogram, is an heat flow (or enthalpy variation) as a function of temperature plot.

The results of a heating-cooling-heating ramp are reported in Figure 3.1. The sample was quenched to -140°C before the test begun and then heated up to 30°C; afterwards, the sample was cooled down to -100°C and the heating ramp was repeated.

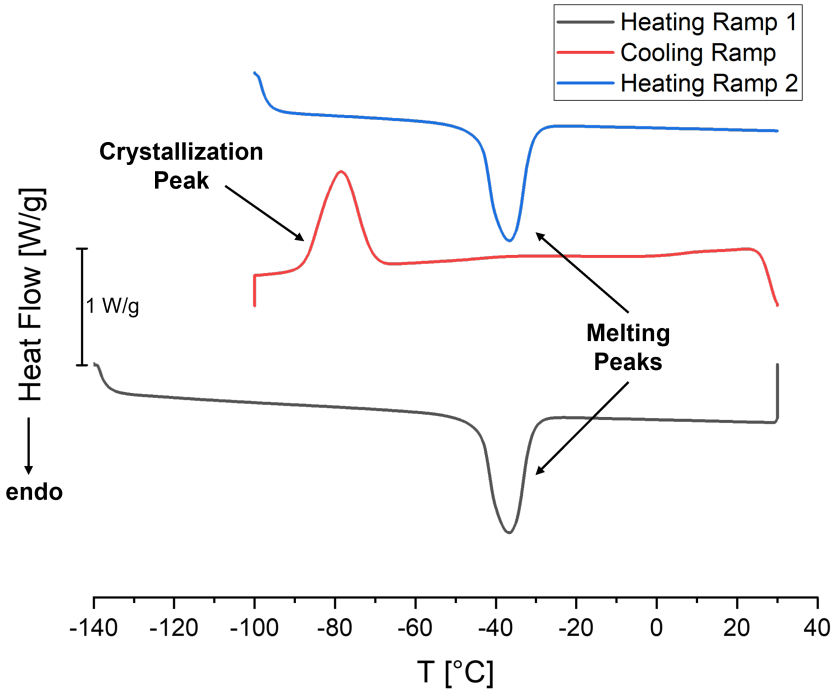

Figure 3.1: DSC output for heating-cooling-heating ramps of Ecoflex 00-50.

The plot shows an endothermal peak, associated with melting at -37°C (peak value) in both heating ramps, whereas an exothermal cold crystallization peak is registered at -78.5°C in the cooling ramp. The melting temperature value strongly resembles those found in literature for Ecoflex 00-30 and RTV silicones which are in the range of -40°C to -45°C [4, 45]. The crystallization temperature is shifted towards lower temperatures compared to that of Ecoflex 00-30 of -64.5°C [45], but is very close to the value of -80°C reported in [4] for RTV silicones. No glass transition endothermal step is observed, which suggests that the T_g of the material may be below -140°C (as noted also in [45]).

Furthermore, the DSC output provides values of the enthalpy of melting and crystallization, calculated from integration of the area underneath the respective peak. The two values obtained are $\Delta H_f = 28.99\ J/g$ (from the first heating ramp), $\Delta H_c = 26.82\ J/g$ and $\Delta H_f = 27.07\ J/g$ (from the second heating ramp). The first value of melting enthalpy is used to obtain the crystallinity degree of the polymer α as:

$$\alpha = 100 \times \frac{\Delta H_f}{\Delta H_0} \tag{3.1}$$

Where ΔH_0 is the melting enthalpy value for a pure crystalline PDMS (i.e. with $\alpha = 100\%$). Assuming Ecoflex 00-50 is a crosslinked PDMS, a value of $\Delta H_0 = 60.8\ J/g$ [4] can be used and a crystallinity degree of $\alpha = 47.6\%$ is obtained. No information regarding

the crystallinity of Ecoflex polymers was found in literature.

3.1.3. Thermogravimetric Analysis (TGA)

Thermogravimetric Analysis (**TGA**) was used to further investigate the thermal properties of Ecoflex 00-50 at high temperatures, determining the upper service temperature and the presence of filler in the material.

TGA analyses were performed on TGA Q500 machine by TA Instruments, using samples of around 20 mg, obtained from the sheets prepared in the moulds. All tests were performed from 23°C to 900°C, at a rate of 10°C/min in both nitrogen and air atmospheres. The output of the analysis were both mass loss (m/m_0) and mass loss rate $(dm/dt) \times (1/m_0)$, often referred to as Differential Thermogravimetric Analysis (**DTGA**), versus temperature plots.

The results of a TGA performed in nitrogen atmosphere are reported in Figure 3.2.

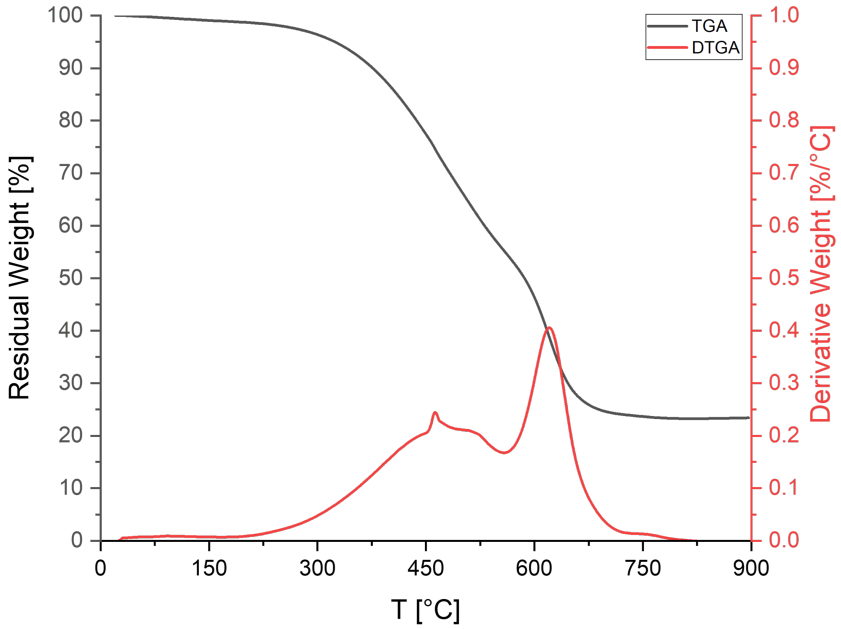

Figure 3.2: TGA and DTGA plot of Ecoflex 00-50 at 10°C/min. in nitrogen atmosphere.

The Ecoflex 00-50 sample shows thermal stability up to around 300°C, with a negligible weight loss of around 5%, and a weight residue of 23.4% at 900°C. It has been shown in [46, 47] that, for pure PDMS networks, the residue at 700°C is nearly 0%, meaning that all the material is thermally degraded through decomposition of the polymer into cyclic oligomers, by $(Si - O)$ bond scission, which are volatile. This observation leads to the conclusion that Ecoflex 00-50 contains some filler, although some residual of the Pt-based

catalyst may still be present.

The residue value obtained is similar, although lower, than the one reported in [41] (31% in weight) for Ecoflex 00-50, and the one reported in [7] (40% in weight) for Ecoflex 00-30.

To understand if the filler is present in the material as it is supplied by Smooth On, or it is formed due to some specific degradation mechanism, a second analysis was performed on a new specimen: from 23°C up to 700°C the test was carried out in nitrogen atmosphere, while from 700°C to 900°C the test was performed in air. The results of the analysis are reported in Figure 3.3

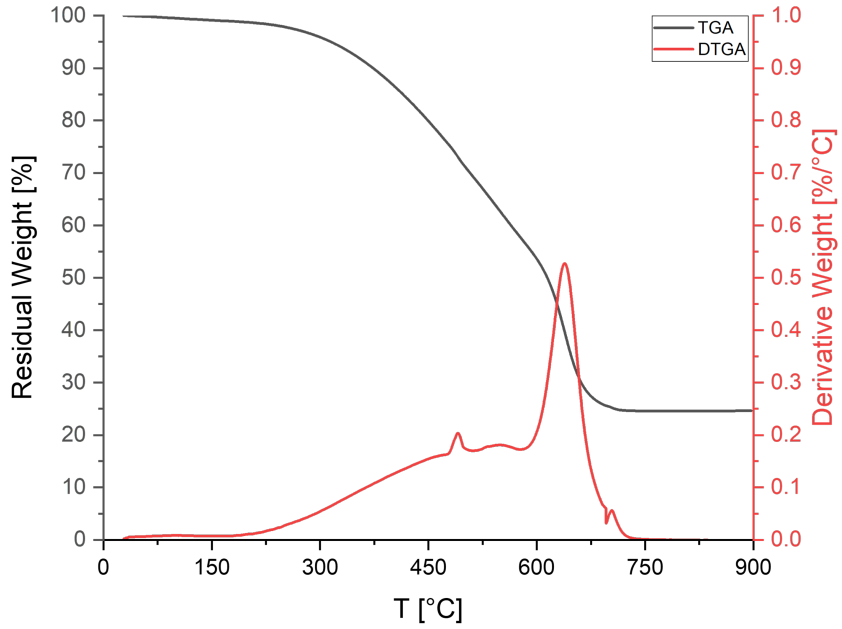

Figure 3.3: TGA and DTGA plot of Ecoflex 00-50 at 10°C/min. Test performed in nitrogen atmosphere up to 700°C and in air atmosphere from 700°C up to 900°C.

In this case, the residue obtained at 900°C is of around 24.6%, which closely matches the value obtained in the test performed in nitrogen atmosphere. This suggests that no silica is formed by interactions between the silicon present in the polymer chains and the oxygen present in the atmosphere. This evidence leads us to the conclusion that Ecoflex 00-50 is fully degraded at 700°C and the residual weight obtained is mainly due to filler presence in the material. No information is provided by the producer on the presence and amount of filler in its materials, but the TGA results in [7, 41], obtained in similar conditions, seem to further support this conclusion.

3.1.4. Raman Spectroscopy

Raman spectroscopy was used to further investigate the structure of Ecoflex 00-50. These analyses were not performed directly during this thesis work, but in collaboration with the work performed for a bachelor degree thesis project, illustrated in [48].

Spectroscopic analyses were performed on a Jobin Yvon Labram HR 800 spectrometer, coupled with an Olympus Bx 41 microscope with a 50x camera lens. A HeNe laser was used to produce the exciting radiation with a wavelength of 632.8 nm (red radiation) and 50 W power. The obtained spectra are obtained with a 2 cm^{-1} resolution and a 10 s acquisition time.

The results obtained, measured in four different regions of a pristine Ecoflex 00-50 specimen, are illustrated in Figure 3.4.

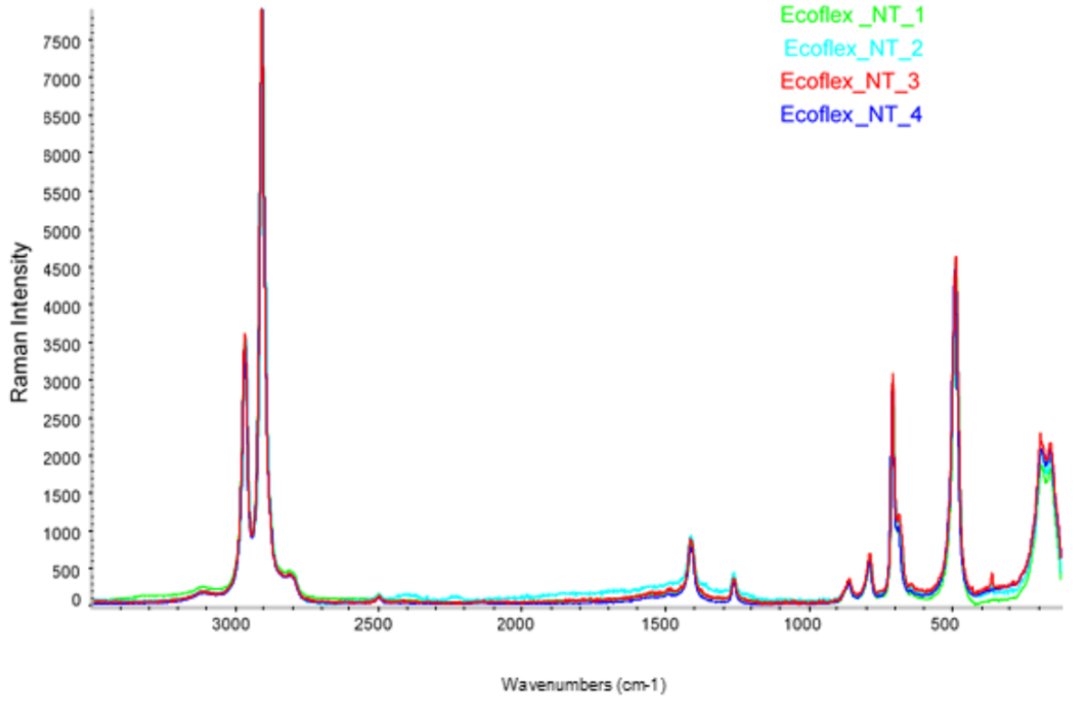

Figure 3.4: Raman spectra of four different measurements performed on a pristine Ecoflex 00-50 specimen [48].

The obtained spectra were compared with those available in literature for pristine PDMS, showing very similar band disposition, and in particular highlighting the presence of frequencies associated with molecular movements of (CH_3) side groups (frequencies between 860 cm^{-1} and 2965 cm^{-1}), those attributed to ($Si-O-Si$) stretching in the main chain (at 489 cm^{-1}) and also ($Si-C$) stretching (at frequencies between 689 cm^{-1} and

788 cm^{-1}). Although Ecoflex producer does not provide any information on the type of silicone elastomer, these results confirm that Ecoflex 00-50 is a PDMS elastomer, as also reported in [7, 41] as a result of Fourier Transform Infrared Spectroscopy analysis.

3.2. Mechanical Tests

3.2.1. Uniaxial Tension Tests

Uniaxial tensile tests were performed on dumbbell specimen, die-cut from square shaped sheets of dimensions 131x131x3 mm. Figure 3.5 reports the dimensions of the specimen which are prescribed by EN ISO 527-2:2012 standard, specimen type 5A [49].

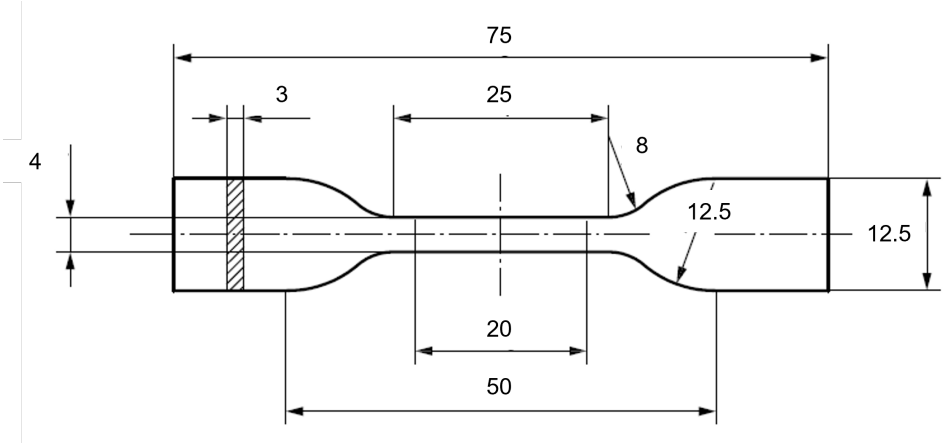

Figure 3.5: Geometry and dimensions of dumbbell specimens used [49]. All dimensions in millimeters.

Uniaxial tensile tests were performed on an Instron 5967 screw driven dynamometer equipped with a 2 kN load cell, using a pneumatic clamping system, to avoid slippage of the specimen during the test.

Tests were video recorded to evaluate the strain by the variation (ΔL) of the relative distance between two black marks drawn on each specimen at a distance of $L_0 \approx 20mm$:

$$\epsilon = \frac{\Delta L}{L_0} \tag{3.2}$$

A 10 MPixel uEye UI 5490 SE camera with a framerate varying between 1 and 20 fps (defined to obtain at least 1000 frames for each test, depending on the their duration) was used. Uniaxial tension tests were performed at different crosshead displacement rates, which are converted to strain rates according to what is reported in Table 3.2.

Table 3.2: Conversion between crosshead displacement rate and strain rate for uniaxial tension tests.

Displacement Rate $[mm/min]$	Strain Rate $[s^{-1}]$
30	0.005
75	0.01
750	0.1

3.2.2. Pure Shear Tests

Tests in pure shear deformation were performed on specimens having thickness of 1 mm, width of 100 mm and gauge length of 20 mm (see Figure 3.6.a). Thicker edges, with a square section of increased thickness of 5 mm, of the specimens allow to properly fix the specimen in the clamping system schematically drawn in Figure 3.6.b. Further information on the clamping systems (called interference clamping) and the specimen specifics can be found in [50].

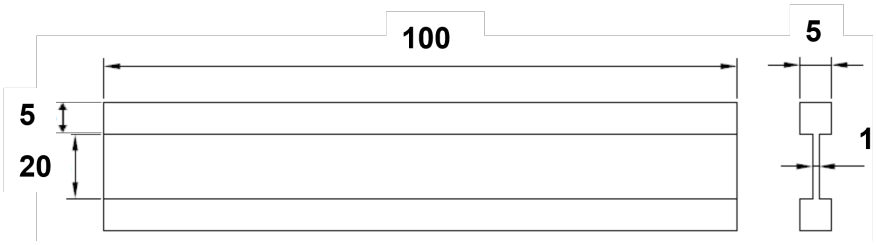

(a)

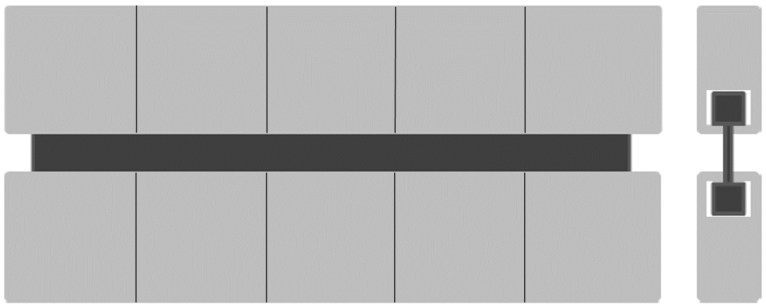

(b)

Figure 3.6: a) Geometry and dimensions of the PS specimen. Dimensions in millimeters. b) Clamping system schematization [50].

Pure shear tests were performed on an Instron 5967 screw driven dynamometer, using a 5 kN pneumatic clamping system in combination with the aluminium clamping system described in [50].

Strains were optically measured using a 10 MPixel uEye UI 5490 SE camera with a framerate varying between 1 and 20 fps (defined to obtain at least 1000 frames for each test, depending on the their duration). For pure shear tests, a speckle pattern was applied on the specimen in order to determine deformation through **Digital Image Correlation** analysis, which is described in detail in Section 3.3. Pure shear tests were performed at different crosshead displacement rates, which are converted to strain rates according to what is reported in Table 3.3.

Table 3.3: Conversion between crosshead displacement rate and strain rate for pure shear tests.

Displacement Rate [mm/min]	**Strain Rate [s^{-1}]**
15	0.01
75	0.05
150	0.1

3.2.3. Biaxial Tension Tests

Biaxial tensile tests were performed on square shaped specimen (Figure 3.7), designed in relation to the custom built biaxial dynamomter described in [50]. The specimen edges are 5mm thick, while the inner thickness is 3 mm. Cuts were introduced in the specimen (see Figure 3.7) to allow the sliding of the clamps during the test and circular holes were made to avoid a premature specimen rupture due to stress intensification at the tip of each cut. Further details are reported in [50].

Biaxial testing was performed on the CLUSTex Biaxial dynamometer, using of a proper clamping system designed in [50] for the application of high strains (see Figure 3.8). The machine is equipped with 12 axial motors controlled independently, six of them equipped with a 25 kN load cell and the remaining six equipped with a 50 kN load cell. The machine is also equipped with an ad-hoc fixture for the camcorder in order to record the surface of the specimen. In this work, only a motor on each side was used and the clamping system was fixed onto central motor of each side. The clamping system consists of four bars, two single and two double ones. Five clamps for each side are mounted on rails on each bar and are free to slide during the test, in order to adapt to the deformation in different directions.

For this thesis work, strains were optically measured, using a 10 MPixel uEye UI 5490 SE camera with a framerate varying between 1 and 20 fps (defined to obtain at least 1000 frames for each test, depending on the their duration). Also in this case, a speckle

pattern was applied on the specimen in order to determine deformation through **Digital Image Correlation** analysis. Biaxial tension tests were performed at different crosshead displacement rates, which are converted to strain rates according to what is reported in Table 3.4.

Table 3.4: Conversion between crosshead displacement rate and strain rate for biaxial tension tests.

Displacement Rate $[mm/s]$	**Strain Rate** $[s^{-1}]$
0.065	0.001
3.5	0.05

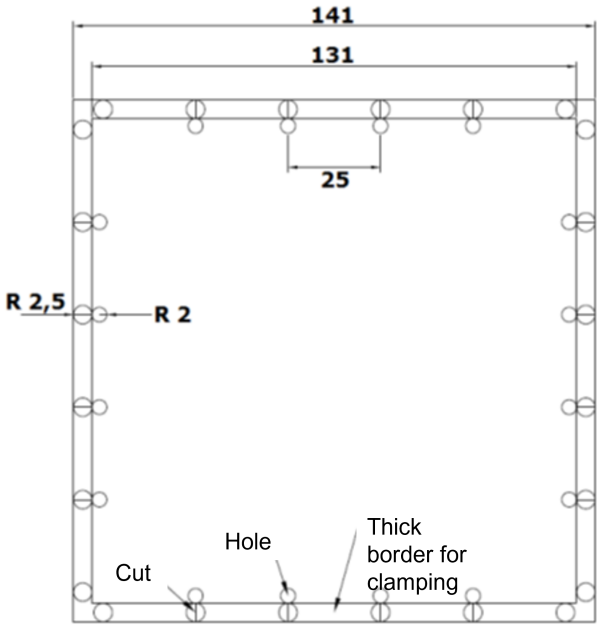

Figure 3.7: Geometry and dimensions of the square shaped specimen for biaxial testing [50]. Dimensions in millimeters.

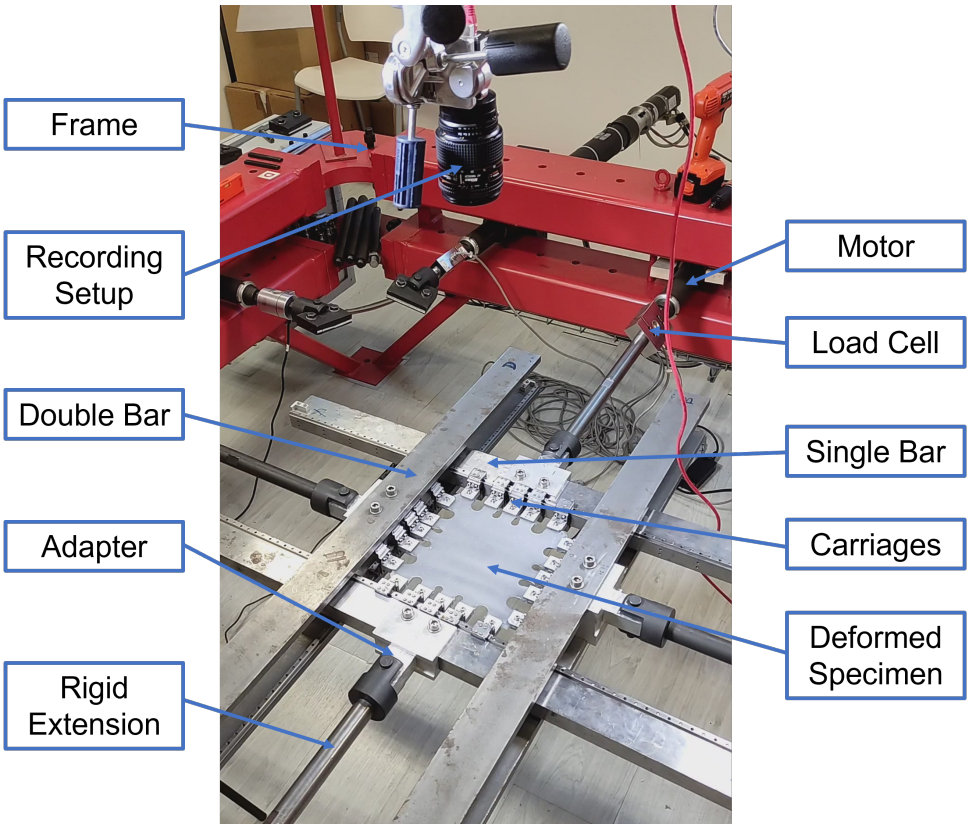

Figure 3.8: The CLUSTex biaxial test setup with the clamping system.

3.2.4. Tensile Tests: Effect of Temperature

The effect of temperature on the mechanical response of the material was evaluated through tensile tests performed on an Instron 5967 dynamometer equipped with an environmental chamber, with strip specimen obtained from PS specimens, by cutting them perpendicularly to the long side. The specimen are 13 mm wide, whereas height and thickness are the same as for PS specimen (see Figure 3.9.a). This particular geometry was adopted instead of the dumbbell specimen previously described, in order to be able to break the various specimens despite the reduced crosshead displacement available in the environmental chamber.

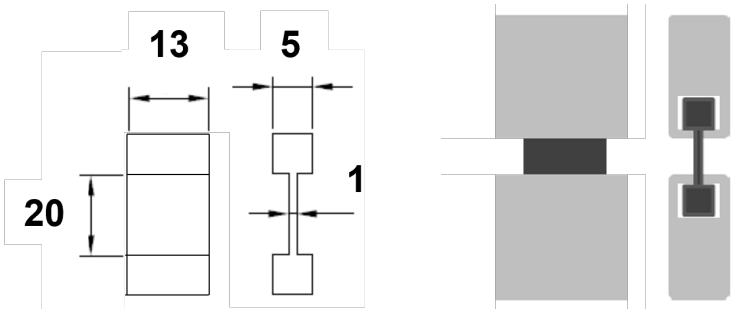

(a) (b)

Figure 3.9: a) Geometry and dimensions of the strip specimen used. All dimensions in millimeters. b) Clamping system schematization.

These tests were performed using a mechanical clamping system to fix the position of the interference clamp which held the strip specimen (see Figure 3.9.b). The test were performed at constant temperature, ranging between -40°C and 140°C: for temperatures below room temperature a liquid CO_2 based cooling system was used, whereas the higher ones were obtained through the integrated heating system of the environmental chamber.

In this case, strains were evaluated as

$$\epsilon = \frac{\Delta L}{L_0} \tag{3.3}$$

where ΔL was obtained directly from the crosshead displacement and L_0 is the initial length of the specimen, equal to 20 mm. This solution was adopted because optical measurements were unfeasible, due to the tarnishing of the temperature chamber front glass at low temperatures. However, preliminary test performed at room temperature with the adopted test configuration highlighted that the machine compliance is negligible and Eq. (3.3) is a very good approximation of the nominal strain.

3.3. Digital Image Correlation (DIC) Analysis

Digital Image Correlation (**DIC**) is a non-contact, optical motion tracking technique which allows to measure the full-field of deformation of an object. During testing, the portion of the specimen of which the deformation measurement is desired must remain within the image and in focus and takes the name of area of interest (**AOI**). The measurement is based on the determination of the displacement field of a surface by means of subdivision of the AOI into smaller square regions, called **subsets**. The spacing between

sub-images is referred to as **step** and defines the measurement grid density.

The test is video-recorded and the image of the undeformed specimen at time zero is used as reference in the analysis of displacements. The displacement field is determined by a comparison process called "correlation" between the reference image and the subsequent ones. In this work, the displacements recorded between the reference and deformed images are large (since we are dealing with an elastomer) and therefore the correlation does not reach convergence, leading to wrong or incomplete measurements. The solution is to perform an **incremental correlation**, determining the displacement of each subset with reference to the previous image, and therefore changing the reference image at each iteration of the analysis.

The most important parameter to obtain a correct and convergent measurement of deformation trough DIC, is the greyscale histogram of the image, which is a measurement of the quantity of information contained in an image. To obtain a suitably wide and spread grey distribution, each subset must be unique and optically distinguishable from the others: this is obtained by drawing on the surface of the specimen a random distribution of spots, called speckles, through the use of an airbrush. The amount of speckles that can be deposited per unit area strongly depends on the operational parameters of the painting process (such as specimen surface-airbrush nozzle distance, airbrush nozzle inclination angle with respect to the specimen surface, number of applied coating layers and user ability) and therefore a set of optimal parameters was determined during preliminary testing. The speckle density determines the spacing of deformation measurements and is reflected on the minimum subset size which can be used.

In [51] it is suggested to use an optical system resolution which allows having 3x3 pixels in each speckle and not less than 3x3 speckles in each subset. Subset step is typically lower than subset size, and for this reason overlapping is present. The suitable degree of overlapping depends on how the surface is structured, since the non-overlapping regions of the subsets must be sufficiently distinguishable. In [52] an in-depth study of the accuracy of the displacements measured with the DIC technique as a function of the subset size is reported; it is also highlighted how high bit-depth, increased contrast and decreased noise allow for a better measurement, as shown in the far left picture in Figure 3.10.

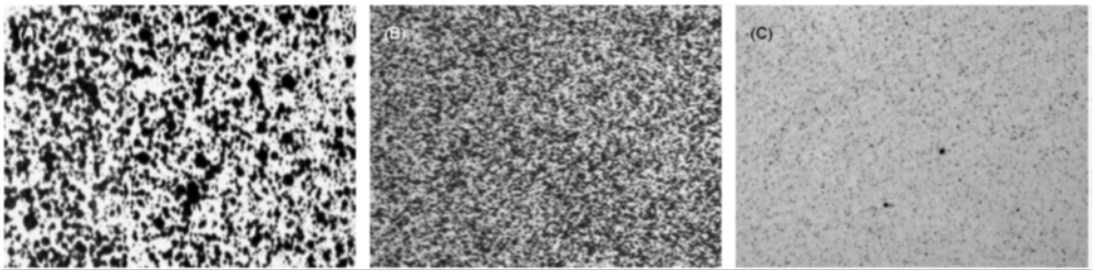

Figure 3.10: Different speckle pattern densities in the undeformed images [52].

During this experimental work, great attention has been given to the determination of the best patterning technique for Ecoflex 00-50, also in terms of adhesion between paint and silicone. Before the application of the pattern, a layer of white metal crack detector ("VMDItalia rilevatore cricche bianco 139") was sprayed onto the specimen, in order to increase adhesion between the non-polar silicone surface and the water based paint used (strongly polar). The pattern characteristics were changed in relation to the type of performed test. The distance between the video camera and the specimen is different in the pure shear and biaxial tensile tests: in biaxial tests (where the camera position is fixed and quite far from the specimen) larger speckles are desired: the airbrush was kept at shorter distance from the specimen and the air flow was kept to a minimum. In pure shear tests, since the camera position can be adjusted accordingly to the maximum strain imposed during the test, smaller speckles were used, obtained adopting spraying conditions opposite to the ones described above.

The software used to perform DIC analysis was **Vic-2D 2009** by Correlated Solutions inc., employing incremental correlation and varying subset size and step accordingly to the testing conditions.

The strain measure output of the program was set to be Green-Lagrange strain (ϵ_L), which can be converted into engineering strain following Eq. 3.4 [53]:

$$\epsilon = \sqrt{2\epsilon_L + 1} - 1 \tag{3.4}$$

3.3.1. DIC Preliminary Study: Optimization of Testing Parameters

In order to better understand the limits of DIC analysis, a series of preliminary tests was conducted to determine the strain measurement resolution, i.e. the minimum deformation which can be detected. The DIC measurement can be affected by many operational

parameters, such as fluctuations of the illumination system, vibrations and other random phenomena which introduce background noise in the measurement. Furthermore, out of plane movements will always be present especially in the case of soft materials (such as Ecoflex 00-50), causing a change of magnification which is interpreted as strain from the DIC software.

In order to determine the strain resolution of the recording system, a series of preliminary tests was performed using PS specimen, subjected to monotonic loading: the specimen was stretched to a strain of 5 through 5 successive deformation ramps (see Figure 3.11). At the end of each deformation ramp, the specimen was held at the applied strain for 5 s. During the holding time, a video of 5 frames was recorded. DIC analysis has been performed on each set of frames, where the first frame was used as reference image. No displacement of the specimen occurs during each 5 s long periods, so any measured strain change should be ascribed to the background noise at each applied strain level. The recording system was not changed during the preliminary tests on PS specimen, since large variations in the distance between video-camera and specimen (fixed at 130 cm) and lens parameters (zoom, focus and aperture) would result in different strain resolution.

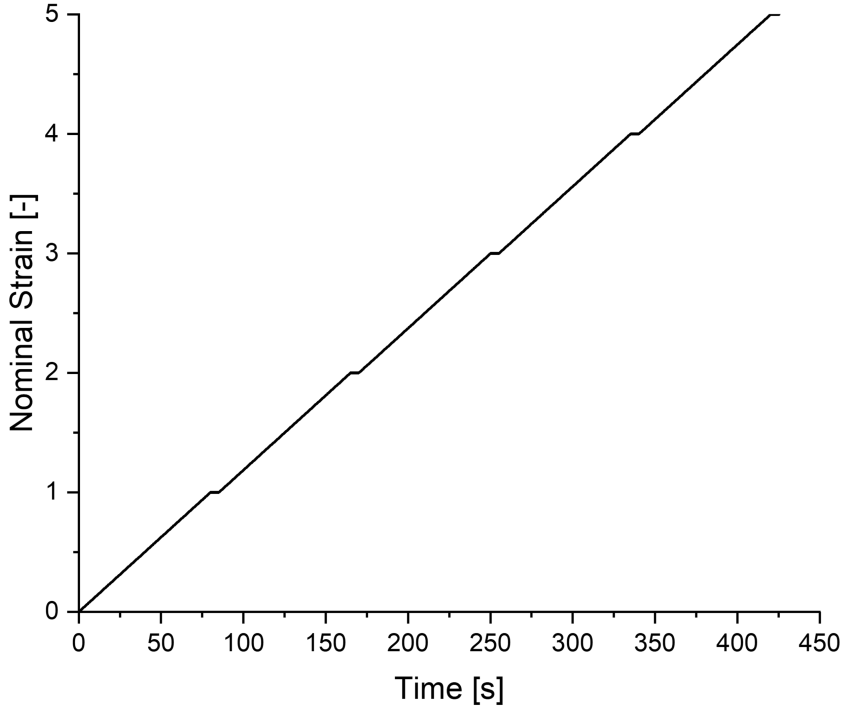

Figure 3.11: Nominal strain vs time plot of the preliminary DIC strain resolution tests.

The results of the analysis, reported for each strain level, are shown in Figure 3.12.

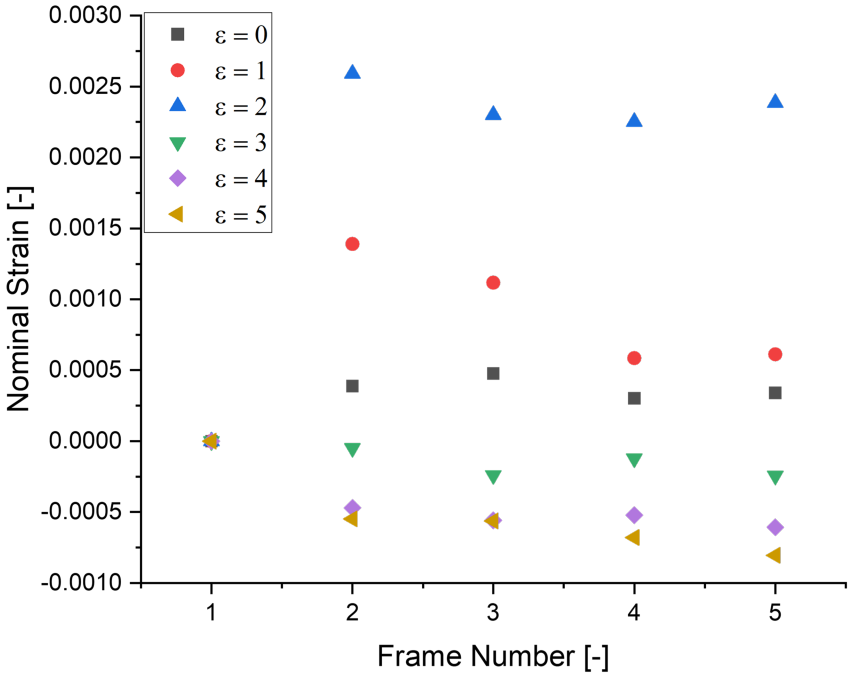

Figure 3.12: Measured parasitic nominal strain for each frame at different imposed nominal strain values.

For each strain level reached at the end of the different loading ramps, parasitic nominal strains were evaluated considering the speckle pattern in the first image acquired during an holding step as undeformed. It can be seen how no defined trend is present with respect to the frame number and to the imposed strain level, highlighting the random nature of the measured noise. The measured nominal strain, associated with background noise, ranges between values from 0.001 to 0.003 (in absolute value), which identify the strain resolution of the system. It should be noted that the this strain resolution stands for the specific testing and recording setup used in this thesis. A different strain resolution is expected if a different setting of the video-recording is adopted. In the future further work should be performed to evaluate this dependence.

Biaxiality maps were plotted according to Eq. (2.21), to identify the region of PS specimens where a good approximation of a pure shear state was present. The results for the uniaxial tensile loading of a PS specimen, for different strain levels, are reported in Figure 3.13.

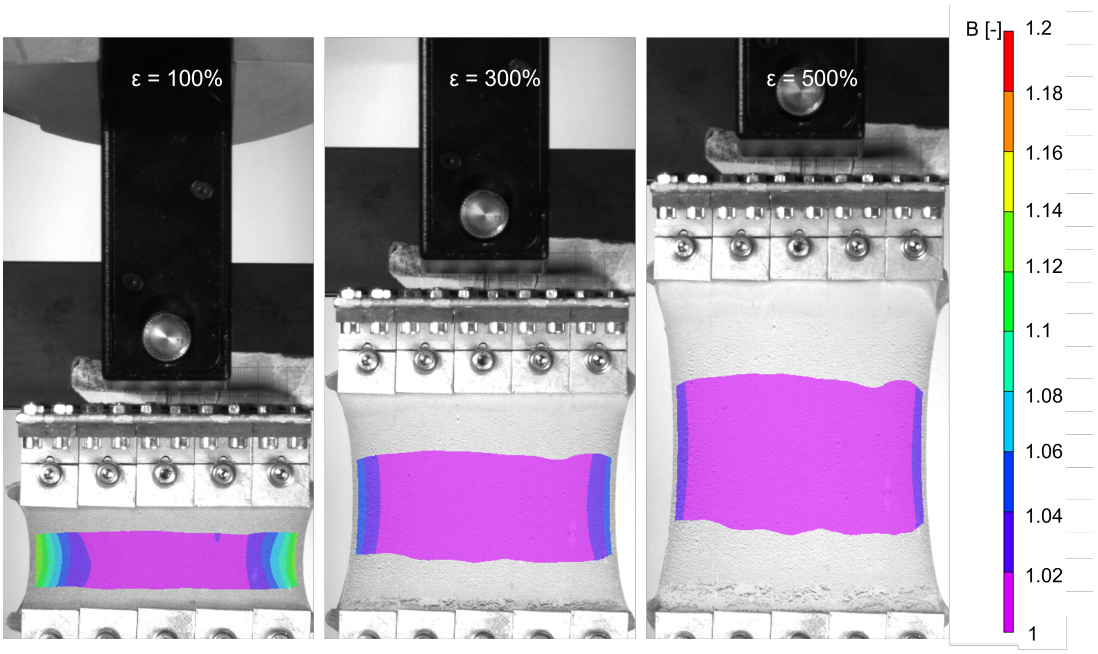

Figure 3.13: Biaxiality maps of a PS specimen subjected to monotonic loading at different strain levels: $\epsilon = 100\%$ (left), $\epsilon = 300\%$ (middle), $\epsilon = 500\%$ (right). Common scale for all three images.

It can be seen how, for the PS specimen, the width of the zone which is in a PS deformation state, indicated by a unit value of the biaxiality, increases as the overall strain increases. This is in accordance with what is reported in [54], where it is highlighted how the free edges of the specimen are able to contract during deformation (similarly to the UT deformation state). In order to accelerate analyses, it was decided to perform DIC analyses only on the central region of the PS specimen. The comparison between the strain obtained from the crosshead displacement and the one obtained from DIC analysis performed on the central region of a PS specimen, during a cyclic loading-unloading test, is reported in Figure 3.14. The strain obtained from the crosshead displacement was calculated as:

$$\epsilon = \frac{\Delta L}{h_0} \tag{3.5}$$

where ΔL is the crosshead displacement and h_0 is the undeformed height of the specimen, corresponding to 20 mm.

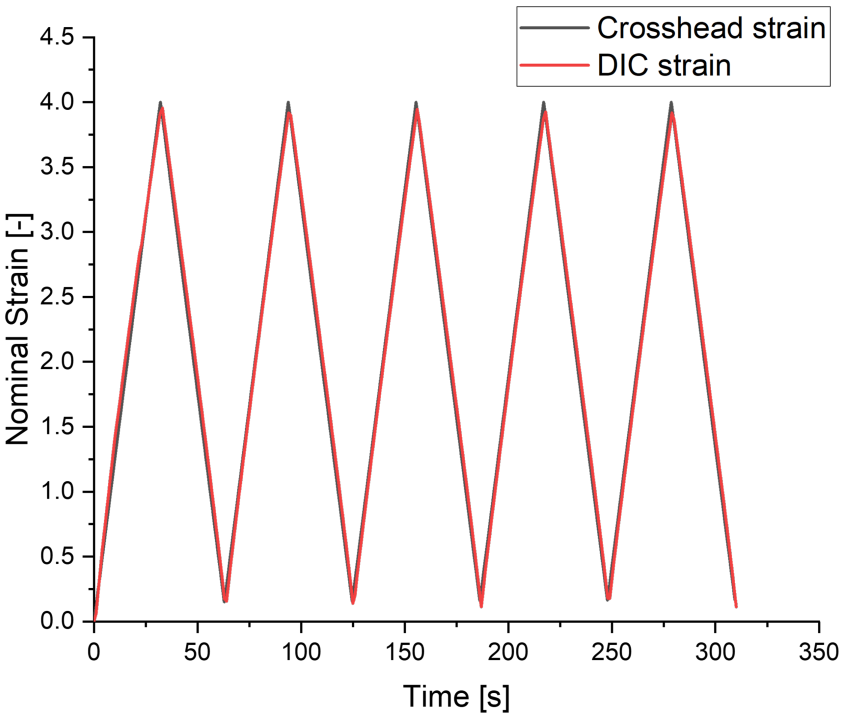

Figure 3.14: Comparison between nominal strain obtained from crosshead displacement (from Eq. (3.5)) and from DIC analysis, performed on the central region of a PS specimen, during a cyclic loading test.

The comparison is performed up to $\epsilon = 4$ since at larger strain levels failure would often occur, most likely due to stress intensification nearby the thick clamped edges. It can be seen how the two strain measurements almost overlap over the whole strain range explored, therefore it was decided to evaluate the applied strain directly from the crosshead displacement for PS tests.

Also for the biaxial tension tests, biaxiality maps were plotted according to Eq. (2.21), to identify the region of the square shaped specimens where a good approximation of an equibiaxial tension state was present. The results for the equibiaxial tensile test (ET) on a squared shaped specimen, at different strain levels, are reported in Figure 3.15, where the whole recording area is reported, which corresponds to approximately 13x10 cm. Due to the close distance of the recording setup to the specimen surface, the outer edges moved out of the frame as the specimen was stretched and therefore are not visible in Figure 3.15.

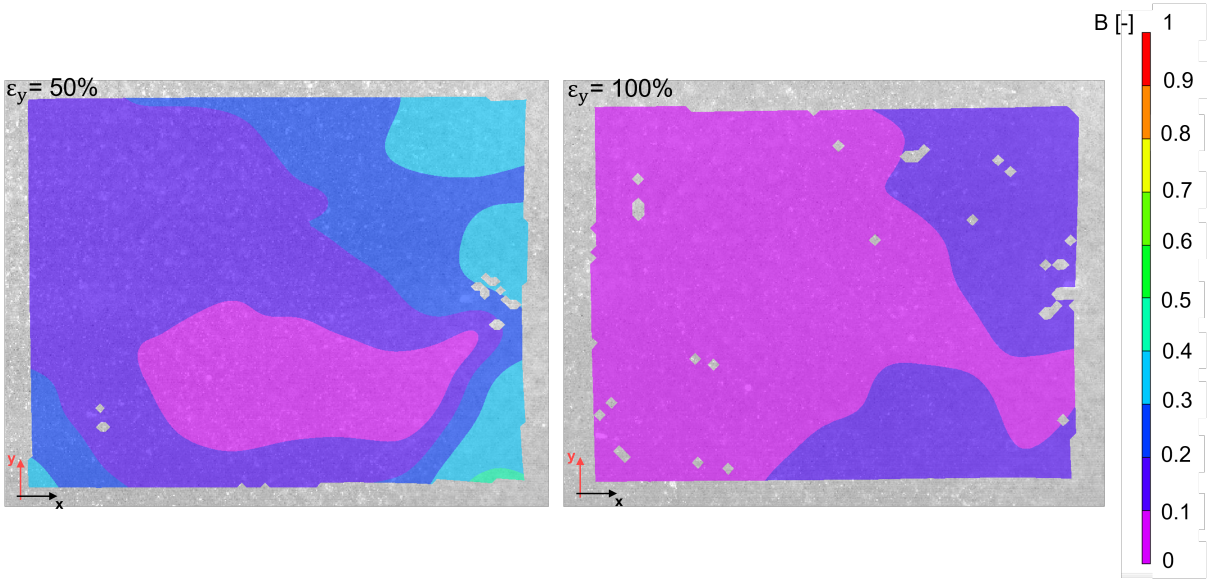

Figure 3.15: Biaxiality maps of a square shaped specimen subjected to monotonic loading at different strain levels: $\epsilon_y = 50\%$ (left), $\epsilon_y = 100\%$ (right). Common scale for both images.

It can be seen how the biaxiality coefficient strongly varies on the analyzed specimen surface. Therefore it was decided to perform DIC analyses on the central region of the specimen (approximately 5x5 cm) where $0 < B < 0.1$, i.e. where the best approximation of the equibiaxial tension deformation state was present. The dimensions of this region are limited because some variations of biaxiality were observed outside of it, which were considered non-negligible. These variations are attributed to experimental conditions: a delay is present in the movement of the axial motors along the x-direction, although the crosshead movement speed is set to be equal in the two directions; furthermore, the sliding of the clamping system (described in Section 3.2.3) is limited at the beginning of the test, because adhesion is observed between surfaces created from the cuts introduced at the edges of the square shaped specimen. Some possible solutions to these experimental problem could be the adjustment of the crosshead moving speed in the two directions, in order to remove delay, and the use of a release agent (e.g. PTFE or talc) to prevent adhesion between the surfaces created by the cuts performed on the specimen.

The comparison between the strains obtained from the crosshead displacement and the ones obtained from DIC analysis performed on the ET region of the specimen is reported in Figure 3.17.

Strains from crosshead displacement were calculated as:

$$\epsilon_x = \frac{\Delta L_B + \Delta L_D}{L_0} \tag{3.6}$$

$$\epsilon_y = \frac{\Delta L_A + \Delta L_C}{L_0} \tag{3.7}$$

where ΔL_B and ΔL_D are the displacements recorded by the crossheads moving in the x-direction (corresponding to principal axis 1), ΔL_A and ΔL_C are the displacements recorded by the crossheads moving in the y-direction (corresponding to principal axis 2) and $L_0 = 131\ mm$ is the undefromed edge length of the specimen. The corresponding stresses are calculated as:

$$\sigma_x = \frac{f_B + f_D}{2L_0H_0} \tag{3.8}$$

$$\sigma_y = \frac{f_A + f_C}{2L_0H_0} \tag{3.9}$$

where f_B and f_D are the forces recorded in the x-direction, f_A and f_C are the forces recorded the y-direction, and $L_0 = 131\ mm$ and $H_0 = 3\ mm$ are the undefromed edge length and thickness of specimen. A representation of the reference system for the square shaped specimen used in biaxial tension tests is provided in Figure 3.16.

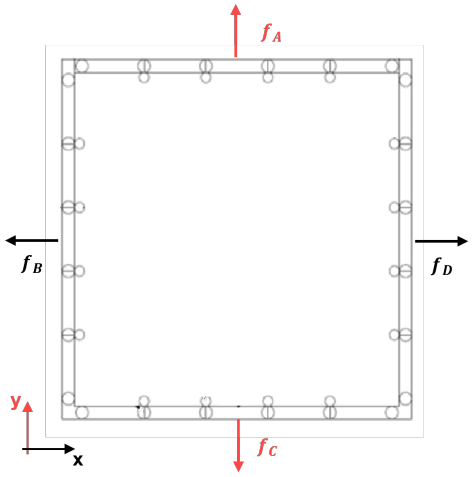

Figure 3.16: Representation of the reference system for the square shaped specimen used in biaxial tension tests.

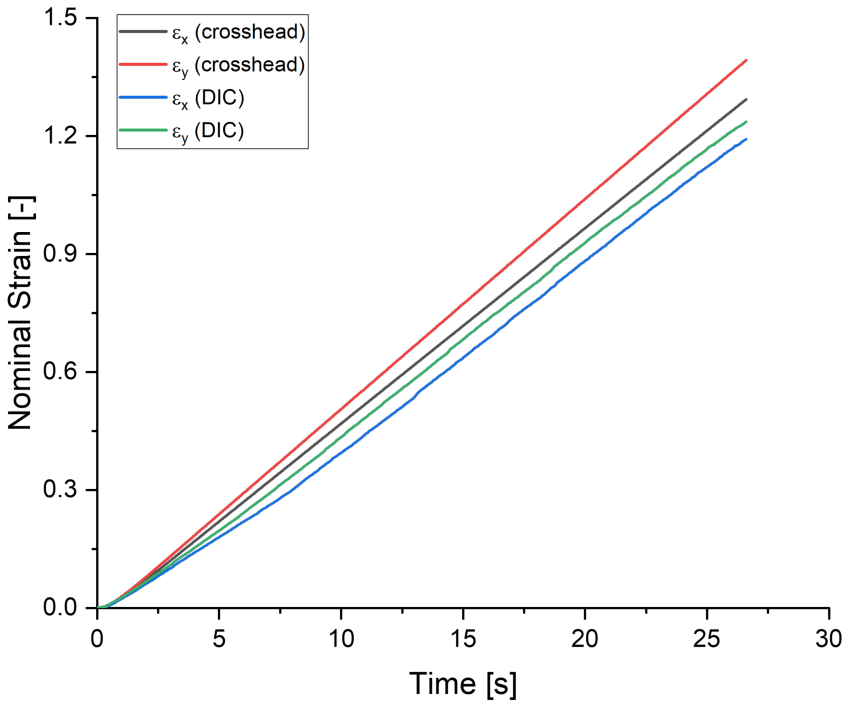

Figure 3.17: Comparison between nominal strain obtained from crosshead displacement and from DIC analysis, performed on the ET region of a square specimen, during a monotonic loading test.

It can be seen how the two strain measurements show lower agreement compared to the PS test, therefore it was decided to determine strains with DIC analysis for every biaxial test performed. It should be noted that in all tests performed, failure would start from the holes at the edges of the specimen and therefore ultimate properties will not be considered reliable.

4 | Experimental Results and Discussion

4.1. Monotonic Tensile Tests

4.1.1. Uniaxial Tension Tests

Preliminary Tests

The nominal and true stress-strain curves for four different UT specimens, die cut from a single square sheet, cured at 23°C for 3 hours (see Section 3.1.1) and tested at a nominal strain rate of $\dot{\epsilon} = 0.01\ s^{-1}$, are reported in Figure 4.1 and Figure 4.2, respectively.

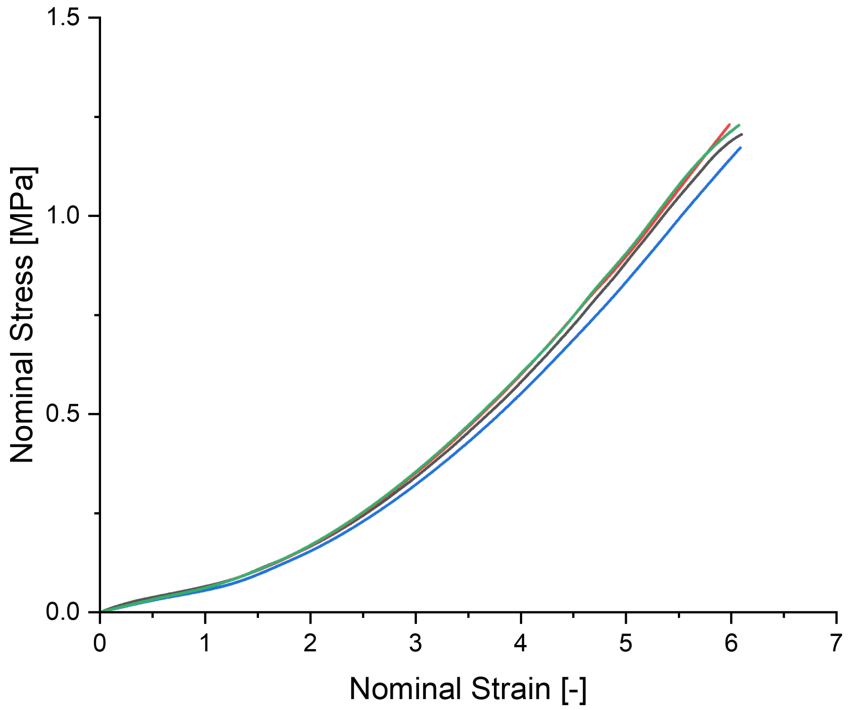

Figure 4.1: Ecoflex 00-50 nominal stress-strain curves for UT tests. The tested specimens were obtained from one square sheet and tested at $\dot{\epsilon} = 0.01\ s^{-1}$.

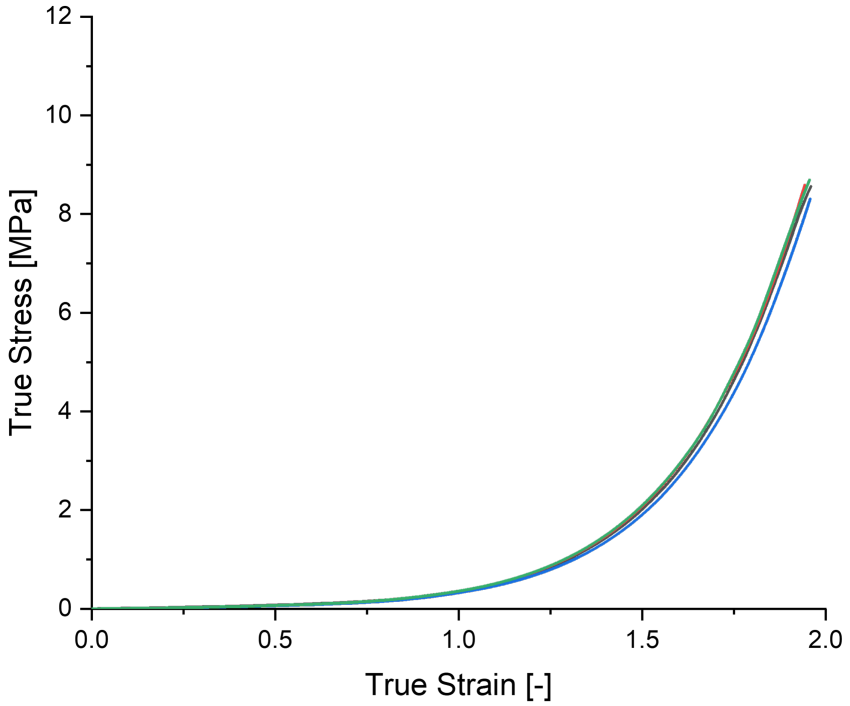

Figure 4.2: Ecoflex 00-50 true stress-strain curves for UT tests. The specimens were die cut from one square sheet and tested at $\dot{\epsilon} = 0.01\ s^{-1}$.

The results show good repeatability and are in accordance with those reported in [42]: failure occurs within the specimen gauge length at a strain of $\epsilon_U \approx 6$ and ultimate stresses of $\sigma_U \approx 1.2$ MPa which are significantly lower than those reported in the material data sheet and summarized in Table 3.1 ($\epsilon_U = 9.8$ and $\sigma_U = 2.15\ MPa$), although no specific information about the specimen used and the testing conditions are provided.

In Figure 4.3, the nominal stress-strain curves of UT tests performed on specimens die cut from three different sheets, all cured at 23°C for 3 hours, and tested at a strain rate of $\dot{\epsilon} = 0.01\ s^{-1}$, are reported. It can be seen how similar repeatability is observed for specimens die-cut from the same sheet, , whereas some variability is present if specimen die-cut from different sheets are compared, mainly for what concerns the ultimate stress which varies between $\sigma_U = 1.3$ MPa and $\sigma_U = 1.1$ MPa, whereas the ultimate strain shows a very limited variation. The differences observed have been attributed to experimental errors in the preparation process (e.g. micro-bubbles formed during casting, defects at the specimen edge from die-cutting etc.)

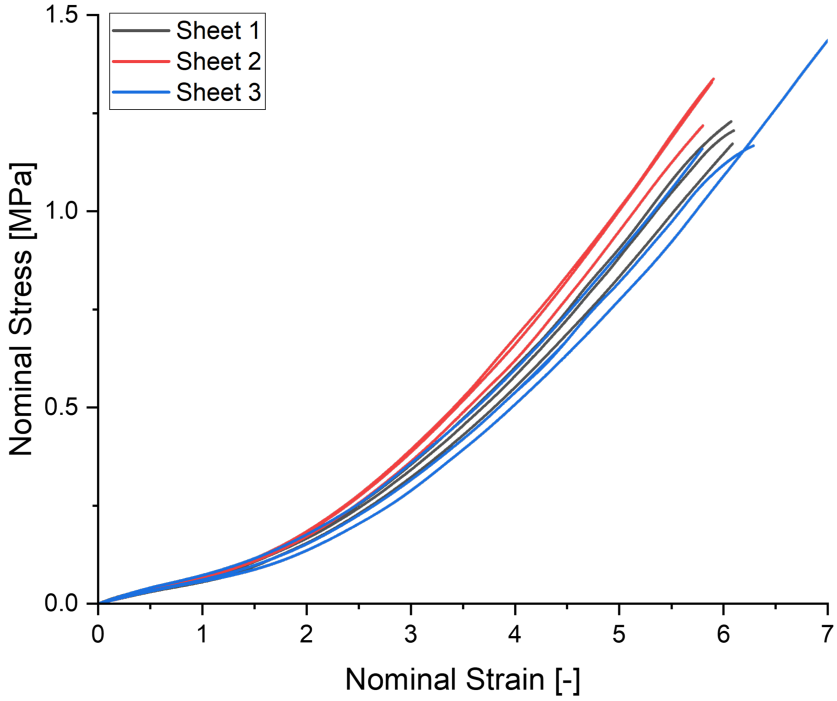

Figure 4.3: Ecoflex 00-50 nominal stress-strain curves for UT tests. The specimens were die cut from three different square sheets and tested at $\dot{\epsilon} = 0.01\ s^{-1}$.

As suggested in the material data sheet [44], a thermal treatment at 80°C for 2 h or at 100°C for 1 h was performed on other specimens die cut from two of the three sheets of Figure 4.3 to evaluate if the data dispersion is reduced after a post curing. Specimens were tested a few minutes after the treatment, at $\dot{\epsilon} = 0.01\ s^{-1}$. The nominal stress-strain curves obtained are reported in Figure 4.4. It can be seen how both thermal treatments don't influence the curves trend and their dispersion, although some specimens fail at a lower ultimate strain than that of the untreated ones, similarly to what is observed in [5]. Since no significant difference was observed, it was decided not to perform any post curing on specimen.

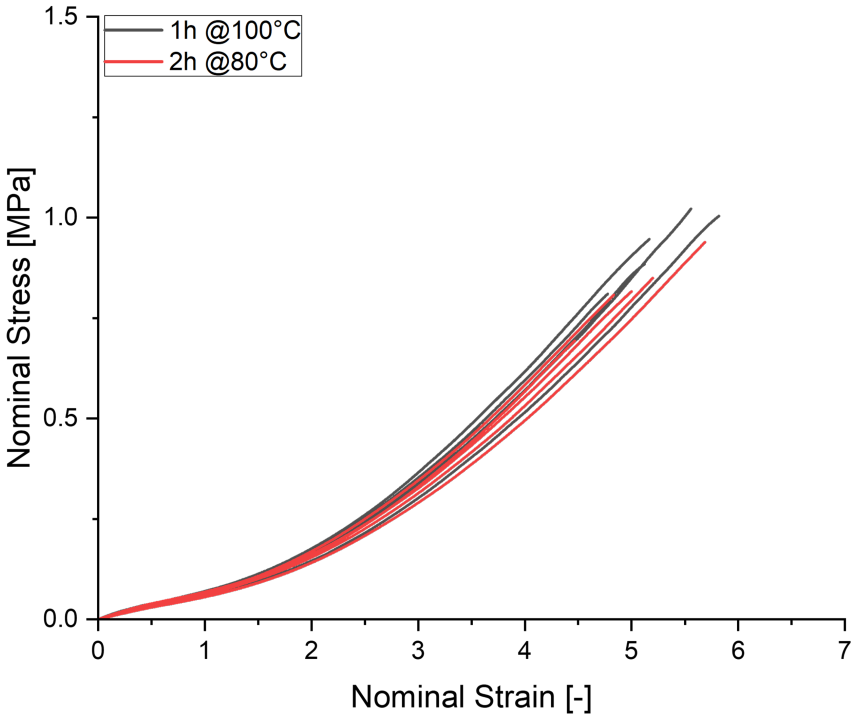

Figure 4.4: Ecoflex 00-50 nominal stress-strain curves for UT tests. The specimens were differently post-treated and tested at $\dot{\epsilon} = 0.01\ s^{-1}$.

Strain Rate Effect

The time-dependency of the mechanical behaviour of Ecoflex 00-50 was investigated performing uniaxial tensile tests at different nominal strain rates, namely $\dot{\epsilon} = 0.005\ s^{-1}$, $\dot{\epsilon} = 0.01\ s^{-1}$ and $\dot{\epsilon} = 0.1\ s^{-1}$. The nominal stress-strain curves for uniaxial tensile tests performed at three different strain rates are reported in Figure 4.5, Figure 4.6 and Figure 4.7. The specimens tested were die cut from three different sheets, to take into account the material preparation variability.

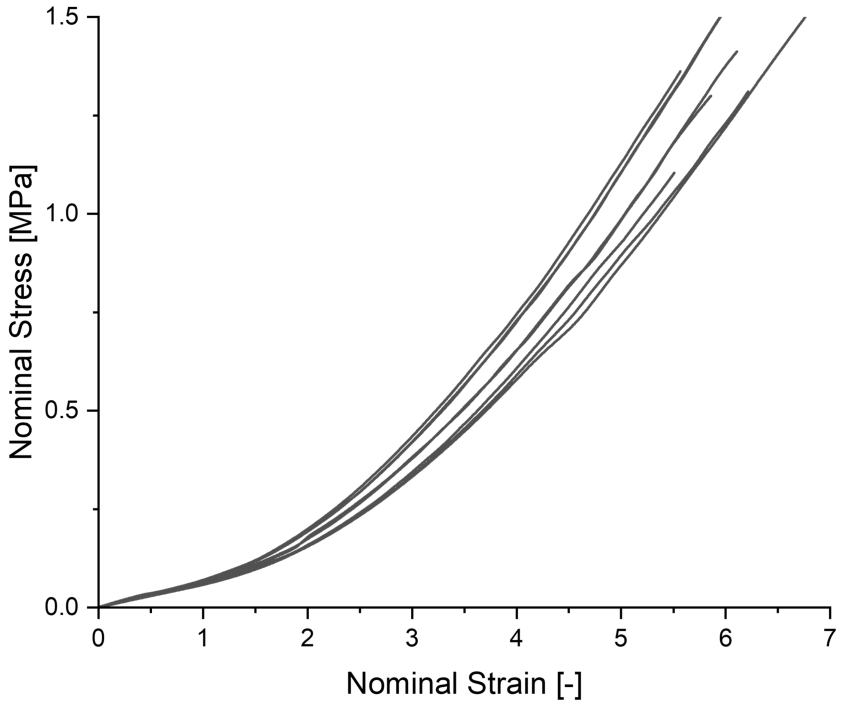

Figure 4.5: Ecoflex 00-50 nominal-stress strain curves for UT tests, performed at $\dot{\epsilon} = 0.1\ s^{-1}$ (specimens were die cut from three different sheets, three for each one).

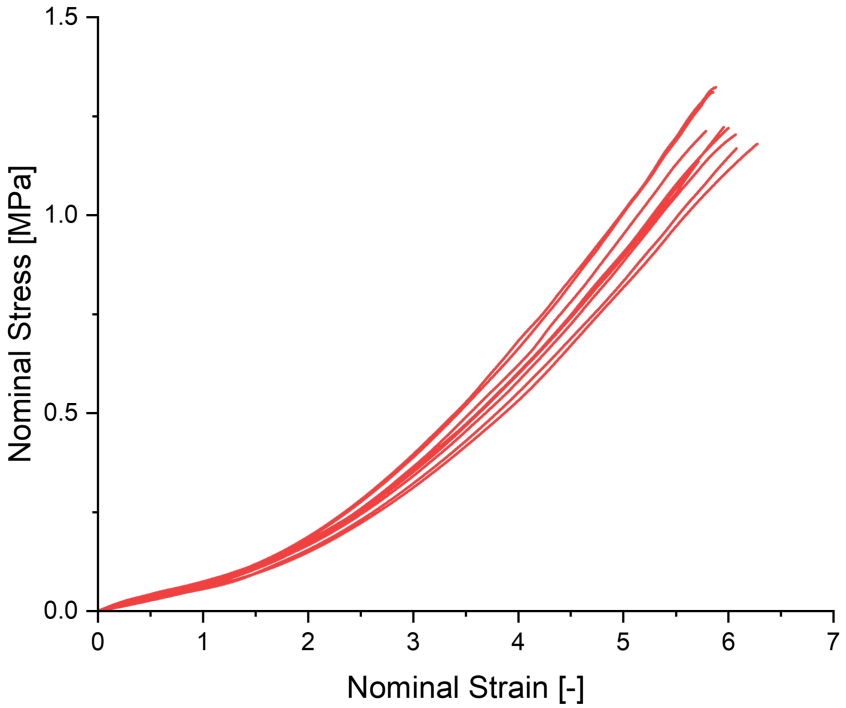

Figure 4.6: Ecoflex 00-50 nominal-stress strain curves for UT tests, performed at $\dot{\epsilon} = 0.01\ s^{-1}$ (specimens were die cut from three different sheets, three for each one)..

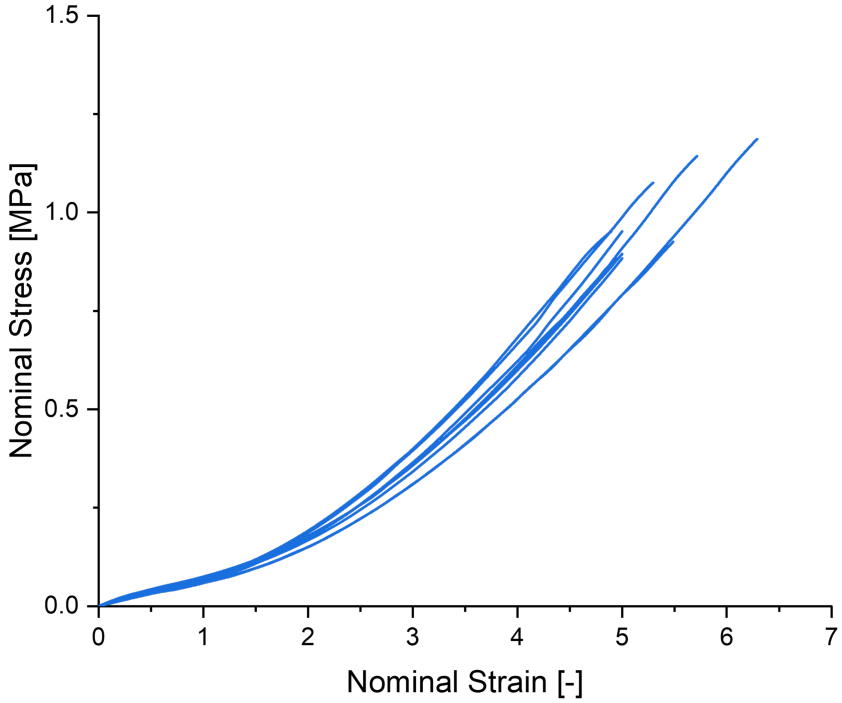

Figure 4.7: Ecoflex 00-50 nominal-stress strain curves for UT tests, performed at $\dot{\epsilon} = 0.005\ s^{-1}$ (specimens were die cut from three different sheets, three for each one).

The curves show similar variability and an increase of both ultimate strain and ultimate stress is observed with increasing strain rate. The averaged values of ultimate strain and stress for each strain rate are reported in Table 4.1.

Table 4.1: Averaged ultimate strain and stress for the different strain rates considered.

Strain Rate, $[s^{-1}]$	**Ultimate Strain, [-]**	**Ultimate Stress, [MPa]**
0.1	5.87 ± 0.49	1.34 ± 0.16
0.01	5.94 ± 0.18	1.22 ± 0.06
0.005	5.29 ± 0.45	0.99 ± 0.12

In particular, the stress and strain at failure obtained for $\dot{\epsilon} = 0.1\ s^{-1}$ are comparable with those reported in [42] of $\epsilon_U = 6.5$ and $\sigma_U = 1.6\ MPa$, although being slightly lower. The curves at $\dot{\epsilon} = 0.01\ s^{-1}$ and $\dot{\epsilon} = 0.005\ s^{-1}$ show a very similar trend. It is possible to notice that the response at low strains (up to $\epsilon = 1$) is strain rate independent, since all curves superimpose in this strain region, whereas for larger strain levels the strain rate dependence is observed, especially for the curves at $\dot{\epsilon} = 0.1\ s^{-1}$. In order to better compare the material behaviour at different strain rates, the highest and lowest experimental stress-strain curves with variability intervals (the area between the two curves) for each test are

reported in Figure 4.8. This representation of data is used to highlight the differences in the material response caused by different strain rates and ultimate stress and strain are not considered meaningful in this representation.

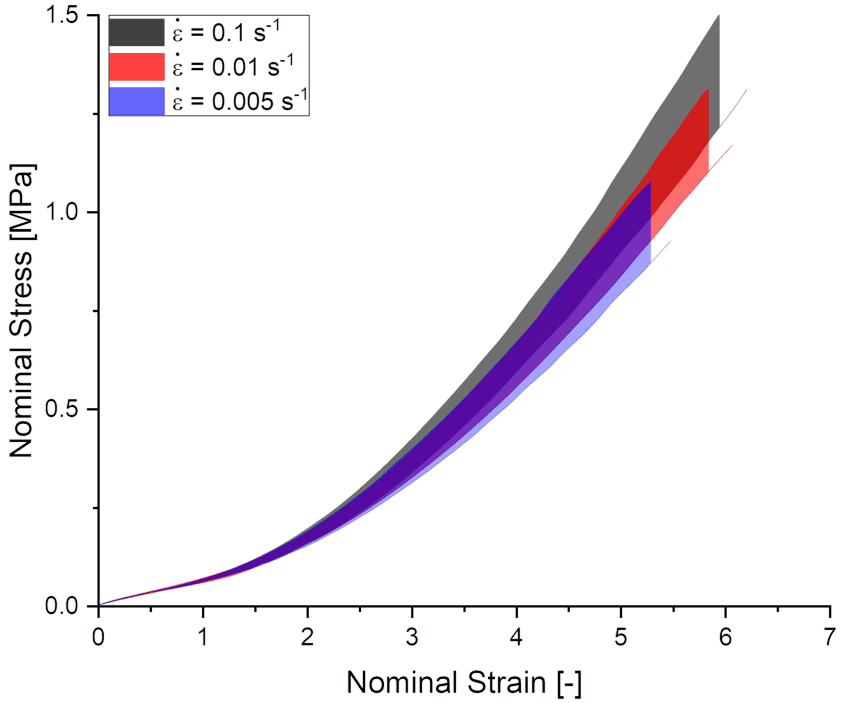

Figure 4.8: Ecoflex 00-50 nominal-stress strain curves for UT tests, performed at three different strain rates (specimens were die cut from three different sheets, three for each one and nine specimen for each strain rate).

In [42], it is suggested to model the material behaviour in the low strain region with a Neo-Hookean model, which is described in Section 2.3.1, since the response shows an overall decreasing slope. Recalling Eq. (2.35), in the Neo-Hookean model the stress is related to $\left(\lambda - \frac{1}{\lambda^2}\right)$ through a proportionality constant G, which is the shear modulus of the material. In order to determine the constant, simultaneous fitting of the stress-stretch curves at each strain rate was performed, in the range $1 < \lambda < 2$. The obtained shear modulus is $G = (0.033 \pm 0.002)$ MPa and no variation is observed with increasing strain rate. No data is available in literature regarding measured values of shear modulus for Ecoflex 00-50, but the value closely resemble that obtained in [42] of $G = 0.039$ MPa, obtained by employing a Shore hardness amplification factor multiplied by the estimated value for Ecoflex 00-10. The comparison between an experimental stress-stretch curve and the Neo-Hookean model is reported in Figure 4.9.

The Young, or tensile, modulus was also determined, as the slope of the linear region of

the stress-strain curves, by a linear fit in the range $0 < \epsilon < 0.5$ and fixing the intercept at the axes origin. The obtained value of tensile modulus is $E = (0.090 \pm 0.005)$ MPa, which also doesn't show strain rate dependence and is in agreement with the value provided in Table 3.1. It is known that the Poisson ratio, Young modulus and shear modulus are related through the following equation, valid in the linear elastic region of the material response [11]:

$$\nu = \frac{E}{2G} - 1 \tag{4.1}$$

while its standard deviation can be obtained through error propagation as:

$$\delta_\nu = \nu \times \sqrt{\left(\frac{\delta_E}{E}\right)^2 + \left(\frac{\delta_G}{2G}\right)^2} \tag{4.2}$$

where δ_E and δ_G are the standard deviations corresponding to the tensile and shear moduli, respectively.

The Poisson ratio obtained is $\nu = 0.36 \pm 0.02$. No data is available in literature regarding the Ecoflex materials Poisson ratio values and, in most cases, incompressible behaviour is assumed; furthermore, ν values reported in literature for unfilled PDMS vary between 0.4 and 0.5, depending on the specific product investigated [55]. The lower value obtained for Ecoflex 00-50 seems to suggest the presence of filler in the material, most likely silica as it is often the case with silicone elastomers, and as TGA data reported in Section 3.1.3 confirm.

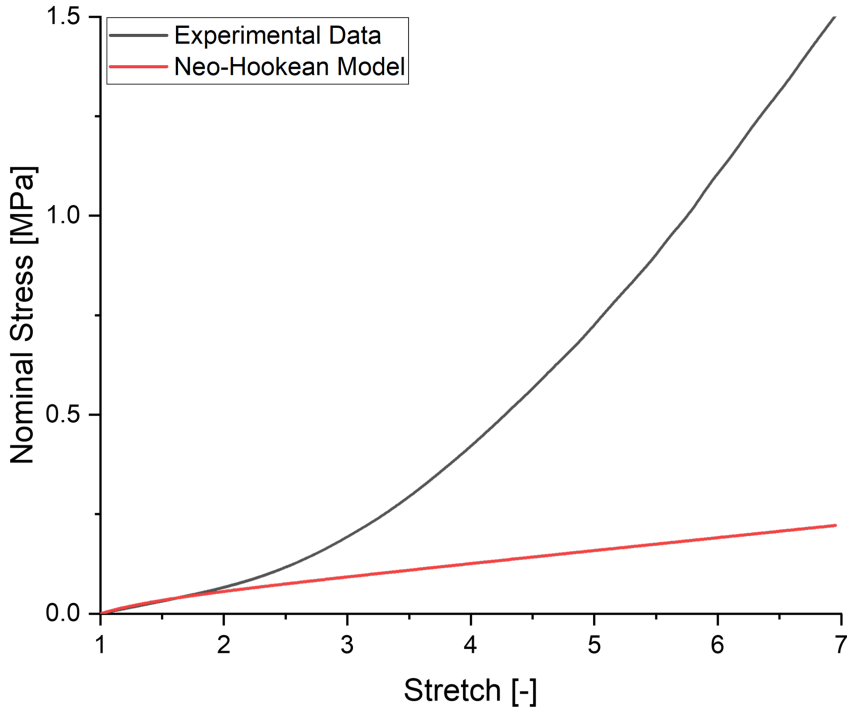

Figure 4.9: Ecoflex 00-50 nominal stress-stretch curves of UT experimental data (from a test performed at $\dot{\epsilon} = 0.1\ s^{-1}$) and the Neo-Hookean model (with $G = 0.032$ MPa).

The strain stiffening observed at large strains in Figure 4.9, may be related to the limited chains extensibility or, being Ecoflex 00-50 a rubber that can crystallize, to its strain induced crystallization. Although DSC tests confirmed the cold crystallization of the material, no test was performed to determine the onset of its strain induced crystallization. In order to evaluate the strain level at which the upturn occurs, it was decided to use the deviation of the material behaviour from the Mooney-Rivlin model (as shown in Figure 2.10), recalling that the reduced stress σ^* is expressed as:

$$\sigma^* = \frac{\sigma}{2\left(\lambda - \frac{1}{\lambda^2}\right)} = C_{10} + \frac{C_{01}}{\lambda} \tag{4.3}$$

The Mooney-Rivlin (MR) plot for the different strain rates studied is reported in Figure 4.10, where a mean curve is reported for each strain rate.

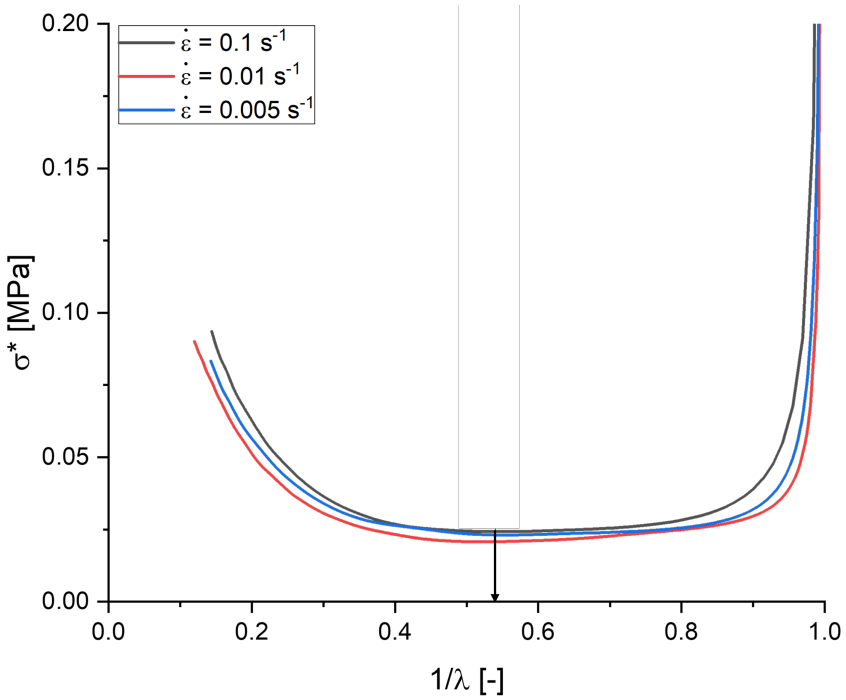

Figure 4.10: Reduced stress (obtained from Eq. (4.3)) vs $1/\lambda$ plot for three different specimen, tested at three different strain rates.

The large increase in reduced stress seen at $\frac{1}{\lambda} \approx 1$ is not reliable, due to too high experimental error in strain and stress measurements. It can be seen that a linear region of the curve exists up to a specific $1/\lambda$ value, which identifies the upturn point ($1/\lambda_{UP}$) of the stress-stretch curve reported in Figure 4.9. Furthermore, the two Mooney-Rivlin constants, C_{10} and C_{01}, can be determined as intercept and slope of the linear region of the plot, respectively (for more details see Section 2.3.1). The values of upturn point and MR constants obtained for each strain rate are reported in Table 4.2.

Table 4.2: Averaged upturn point and MR constants values for the different strain rates considered.

Strain Rate, [s^{-1}]	**Upturn Point, [-]**	**C_{10}, [MPa]**	**C_{01}, [MPa]**
0.1	0.54 ± 0.01	0.016 ± 0.003	0.015 ± 0.002
0.01	0.52 ± 0.02	0.014 ± 0.003	0.014 ± 0.003
0.005	0.53 ± 0.02	0.017 ± 0.003	0.011 ± 0.002

It can be noticed that the upturn point and the Moonery-Rivlin constants are not dependent on the strain rate of the test, showing comparable results for all strain rates considered. Therefore, the values averaged over data obtained at different strain rates

were calculated: the upturn point was identified to be $\frac{1}{\lambda_{UP}} = 0.54 \pm 0.01$ which corresponds to $\lambda_{UP} = 1.85 \pm 0.01$. The two averaged Mooney-Rivlin constants values obtained are $C_{10} = (0.016 \pm 0.003)$ MPa and $C_{01} = (0.013 \pm 0.003)$ MPa. These results further highlight how the low strain region of the material response (up to $\lambda = 2$, corresponding to $\epsilon = 1$) is strain rate independent.

Poisson Ratio Evaluation

DIC analyses were performed on the video recording of UT monotonic loading at $\dot{\epsilon} = 0.01\ s^{-1}$, performed on dumbell specimens. The ratio between the transverse and longitudinal strains was determined from the analysis. In Figure 4.11 this ratio is plotted as a function of the longitudinal strain. The applied strain dependence of this ratio, reported in Eq. (4.4), for incompressible materials is reported too, where the incompressible theoretical strain ratio is expressed as:

$$-\frac{\epsilon_2}{\epsilon_1} = \frac{1}{\epsilon_1}\left(1 - \frac{1}{\sqrt{\epsilon_1 + 1}}\right) \tag{4.4}$$

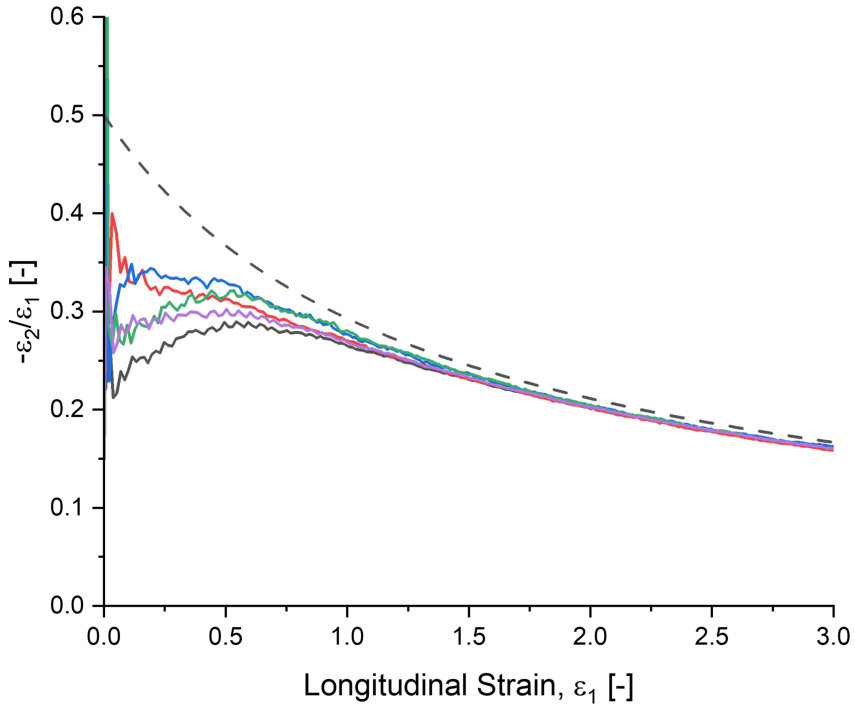

Figure 4.11: Ratio between the transverse and longitudinal nominal strain vs nominal longitudinal strain plot. The measurement was performed on five specimens (coloured continuous lines). The theoretical trend for an incompressible material is reported too (dashed black line).

It can be seen that for $\epsilon_1 < 0.5$ the experimental data do not show a clear trend, which can be attributed to the fact that the transverse contraction of the specimen is too small and it is probable that in this deformation range the resolution is larger than the measurement itself, although no DIC analysis resolution studies were performed in this case, whereas for $\epsilon_1 > 1$ the experimental curves trends are in agreement with the theoretical trend, while the value is lower. Therefore, interpolation (from $\epsilon_1 > 0.5$) with different polynomial functions was performed to extrapolate the zero-strain value of the transverse-longitudinal strain ratio, which is the Poisson ratio of the material. The results are reported in Table 4.3.

Table 4.3: Poisson ratio obtained for with different polynomial function interpolation of experimental data.

Polynomial Order	**Poisson Ratio**
First	0.33 ± 0.01
Second	0.36 ± 0.02
Third	0.36 ± 0.03
Fourth	0.34 ± 0.04

It can be seen how, for all polynomial orders except the linear fitting, the value obtained is very close to the one estimated from the tensile and shear moduli, in the previous section; such ν value suggests that Ecoflex 00-50 is a filled elastomer, as already suggested by TGA analyses (see Section 3.1.3).

4.1.2. Pure Shear Tests

The nominal stress-strain curves of Ecoflex 00-50 in PS loading conditions, tested at a strain rate of $\dot{\epsilon} = 0.01\ s^{-}1$, are reported in Figure 4.12.

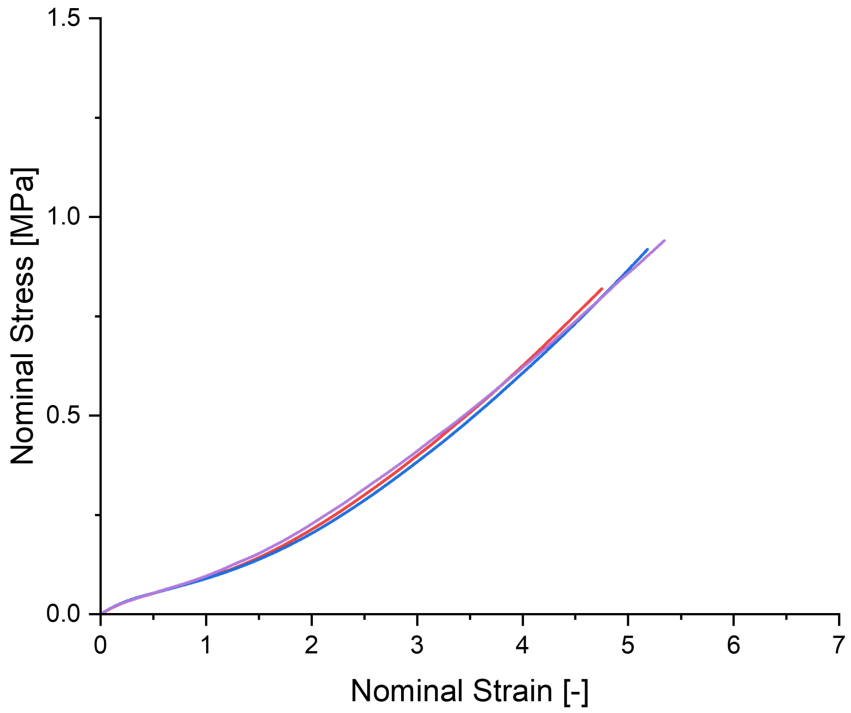

Figure 4.12: Ecoflex 00-50 nominal stress-strain curves for PS tests. Five specimens tested at $\dot{\epsilon} = 0.01\ s^{-1}$.

The results show higher repeatability compared to UT stress-strain curves. It should be noted that, for all specimens, failure occurs nearby the thick clamped edges, most likely due to stress intensification. Due to this effect and to errors during specimen clamping, a larger dispersion of ultimate strain is observed, ranging from $\epsilon_U = 4$ to $\epsilon_U = 5.35$.

For PS tests, three different strain rates were chosen for testing, namely $\dot{\epsilon} = 0.01\ s^{-1}$, $\dot{\epsilon} = 0.05\ s^{-1}$ and $\dot{\epsilon} = 0.1\ s^{-1}$, in order to understand if the material strain rate dependence was affected by the deformation state of the test. The nominal and true stress-strain curves for 15 different specimen tested at three different strain rates (five specimen for each strain rate), are reported in Figure 4.13.

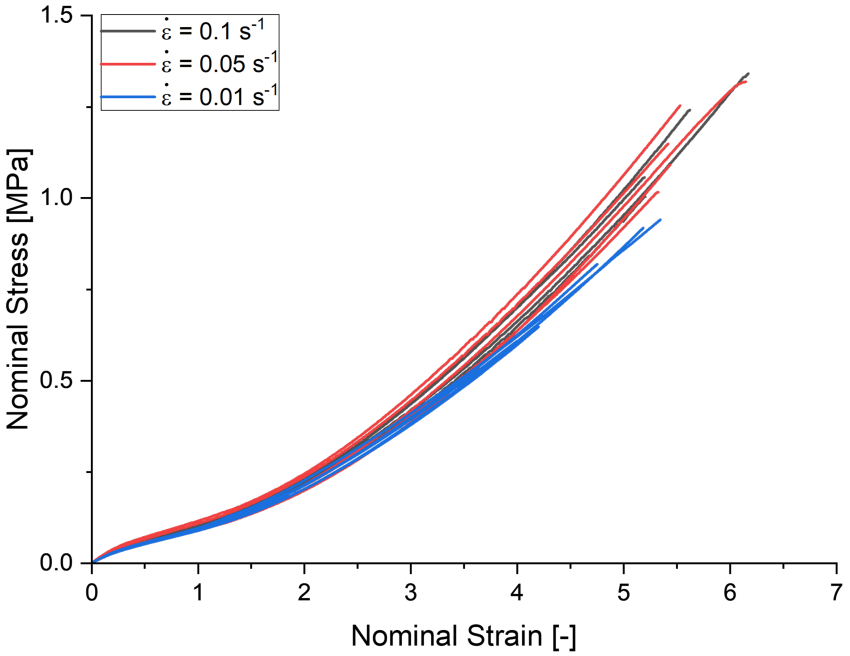

Figure 4.13: Ecoflex 00-50 nominal stress-strain curves for PS tests. 15 specimens tested at different strain rates (five specimens for each strain rate).

The curves corresponding to the PS specimen tested at $\dot{\epsilon} = 0.01\ s^{-1}$ show the most limited variability, whereas the curves for the other two strain rates show comparable repeatability and lower dispersion for what concerns ultimate strains. The effect of strain rate is very limited, and in fact specimen tested at $\dot{\epsilon} = 0.1\ s^{-1}$ and $\dot{\epsilon} = 0.05\ s^{-1}$ show comparable response, whereas an increase in stress is noticeable for $\epsilon > 2.5$, compared to the specimen tested at $\dot{\epsilon} = 0.01\ s^{-1}$. Also in pure shear deformation state the portion of the curve up to $\epsilon \approx 1$ is unaffected by strain rate variations.

Equivalent Simple Shear

Recalling the observations reported in Section 2.2.2, from the stress and the draw ratio applied in the first principal direction in PS state, it is possible to determine the shear stress in the equivalent Simple Shear (SS) state. The equivalent shear stress τ can be obtained from Eq. (2.19), whereas the equivalent shear deformation γ can be determined from λ_1 according to Eq. (2.15). The equivalent shear stress vs shear strain plot, obtained from the data of a PS specimen tested at $\dot{\epsilon} = 0.01\ s^{-1}$, is reported in Figure 4.14, alongside the theoretical linear trend obtained from a linear fit of the data for $\gamma < 1$.

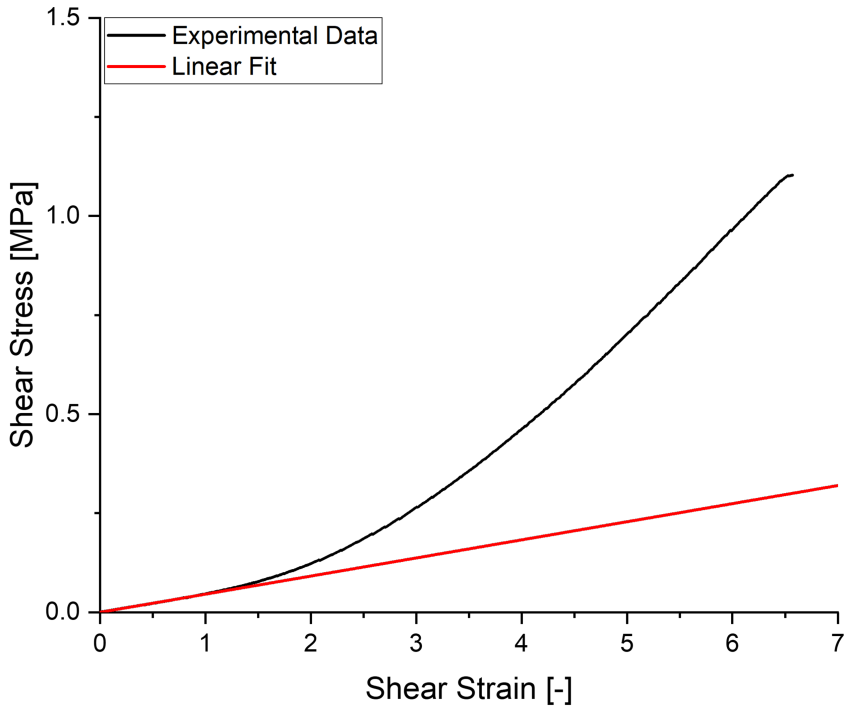

Figure 4.14: Shear stress-strain plot (black line) obtained from PS data of a specimen tested at $\dot{\epsilon} = 0.01\ s^{-1}$, and theoretical linear trend obtained from linear fit (red line).

The equivalent SS data and the theoretical linear trend show agreement up to $\gamma = 1$ (as already noted in Figure 2.4), corresponding to $\lambda \approx 1.6$ where no strain rate dependence is observed. The trend is different from the one reported in [1]where, after the linear region, the equivalent SS trend lies below the theoretical linear trend: in the case of Ecoflex 00-50 the equivalent shear stress is higher than the theoretical one for $\gamma > 1$, which was attributed to the fact that the upturn point (indicating strain stiffening) is observed in the low strain region, and therefore the real response is always above the theoretical linear trend. From the slope of the linear region, it is possible to determine the shear modulus of the material: the result obtained by simultaneously fitting 15 equivalent shear stress-strain curves is $G = (0.048 \pm 0.002)$ MPa, which is higher than the value obtained by fitting UT data with the Neo-Hookean model, and also of the value obtained in [42] from UT data. Also in this case, the value does not show a strain rate dependence. The discrepancy in the value of shear modulus obtained from the Neo-Hookean fitting of UT data and the one obtained from the equivalent SS state, suggests how simultaneous fitting of experimental data in different deformation states could provide a better approximation of the real value of G and other material constants.

4.1.3. Biaxial Tension Tests

The nominal stress-strain curves from load and displacement measurements performed in the two deformation directions (called x and y) of a square shaped specimen, tested at a strain rate of $\dot{\epsilon} = 0.05\ s^{-1}$ (which corresponds to the maximum rate achievable by the dynamometer), are reported in Figure 4.15.

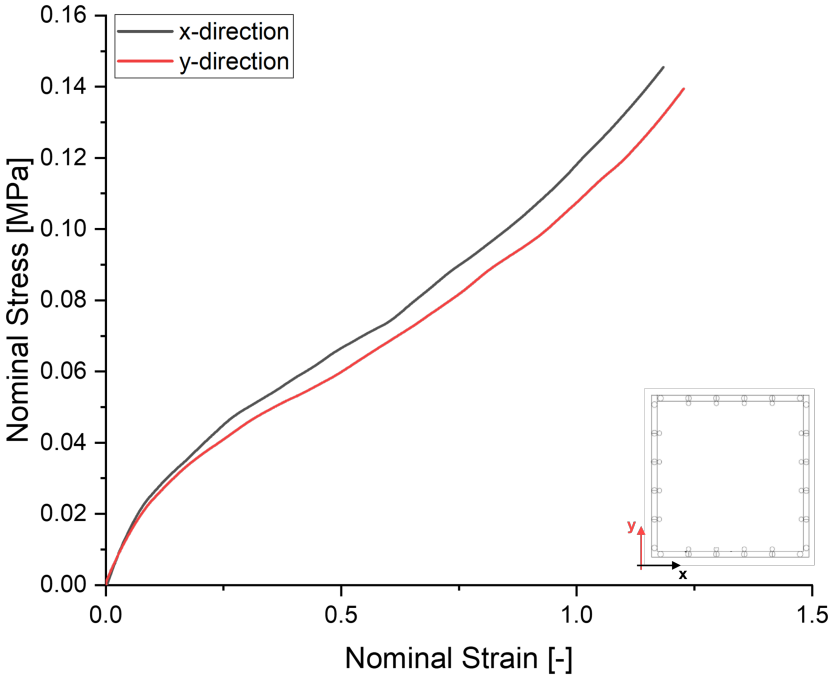

Figure 4.15: Nominal stress-strain curves in the x and y directions of a square shaped specimen tested at $\dot{\epsilon} = 0.05\ s^{-1}$.

As previously observed, due to a difference between the crosshead displacement rate in the two directions, the test is not an equibiaxial tension test. The stress-strain curves in the two direction are not superimposed suggesting that, as expected, the material response to the stretching in one direction depends ond the stress/strain applied in the perpendicular one. The difference in the two curves can be attributed to the dynamometer used during testing, in which the movement in the x-direction was delayed compared to that in y-direction and, as a result, the x-direction stress-strain curve is always above the one in the other direction. Furthermore, the ultimate values obtained during biaxial tensile tests are not reliable, since failure always starts from the holes at the border of the specimen, due to stress intensification. However, it is noticeable how failure occurs at ultimate strain values of $\epsilon_U \approx 1.2$, much lower than those observed for UT and PS tests.

The nominal stress-strain curves of three different square shaped specimen, tested at

$\dot{\epsilon} = 0.05\ s^{-1}$, are reported in Figure 4.16. It can be seen that some degree of variability exists among the different stress-strain curves, most likely because of the problems related to the testing setup, which often would lead to inhomogenous deformation of the specimen and resulting in different stress-strain trends. Due to the limited extensibility of the material in this deformation state, the dispersion of the curves is more limited compared to that obtained in UT and PS states.

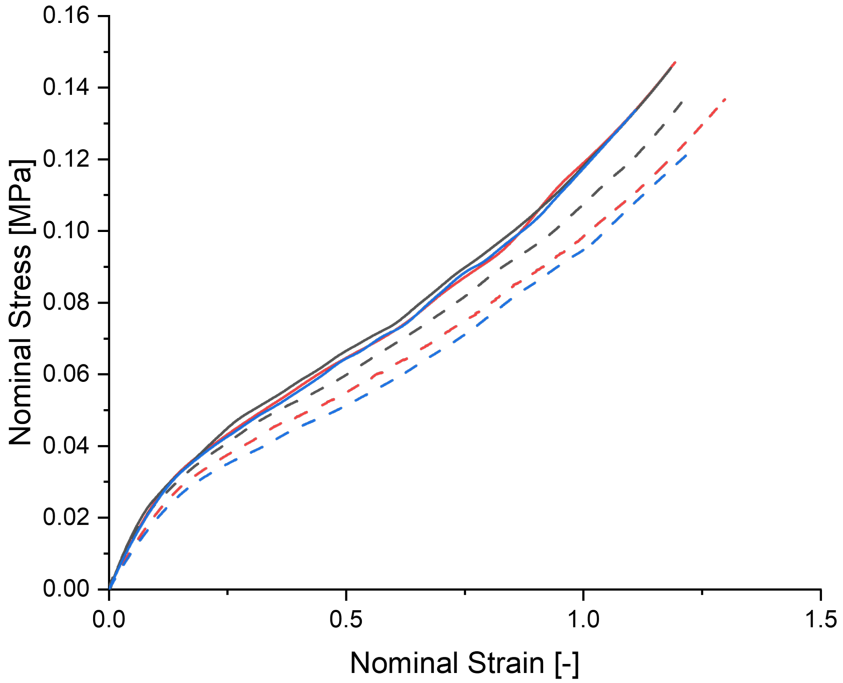

Figure 4.16: Nominal stress-strain of three different square shaped specimen tested at $\dot{\epsilon} = 0.05\ s^{-1}$, for x-direction (continuous lines) and y-direction (dashed lines).

Since the variability is present only in the y-direction response, it was decided, in order to have a clearer representation of experimental data and to allow easier modelling of the material behaviour (see Section 4.1.5), to associate a single stress-strain curve to each specimen tested, obtained by averaging the results in the two directions as follows:

$$\sigma = \frac{\sigma_x + \sigma_y}{2} \tag{4.5}$$

$$\epsilon = \frac{\epsilon_x + \epsilon_y}{2} \tag{4.6}$$

The comparison between the averaged data for three different specimen tested at $\dot{\epsilon} = 0.05\ s^{-1}$ is reported in Figure 4.17.

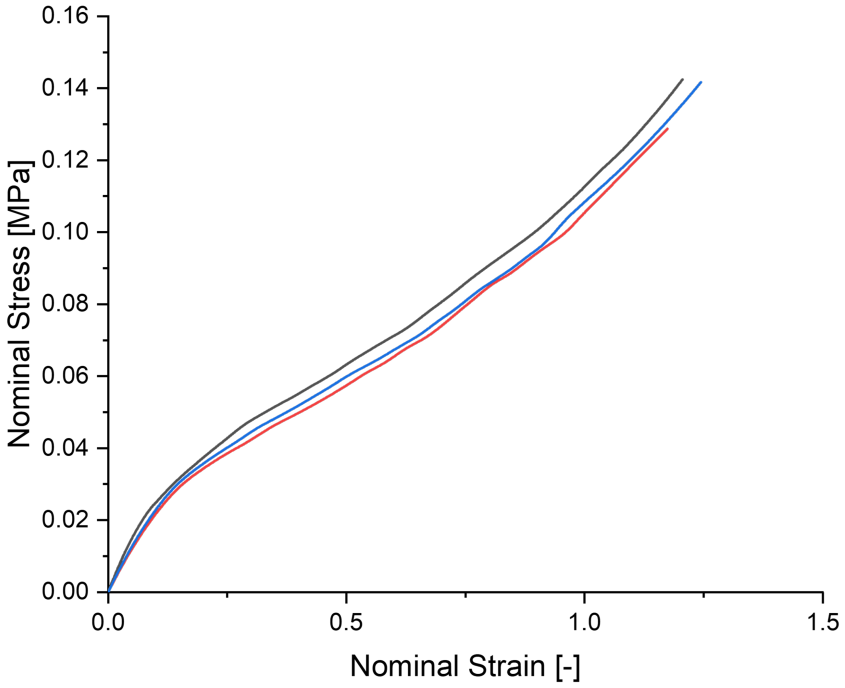

Figure 4.17: Nominal stress-strain of three different square shaped specimen tested at $\dot{\epsilon} = 0.05\ s^{-1}$.

The effect of strain rate on the material behaviour in BT deformation state was evaluated performing tests at two different strain rates, namely $\dot{\epsilon} = 0.05\ s^{-1}$ and $\dot{\epsilon} = 0.001\ s^{-1}$. The nominal stress-strain curves for two different specimen, tested at two different strain rates, are reported in Figure 4.18.

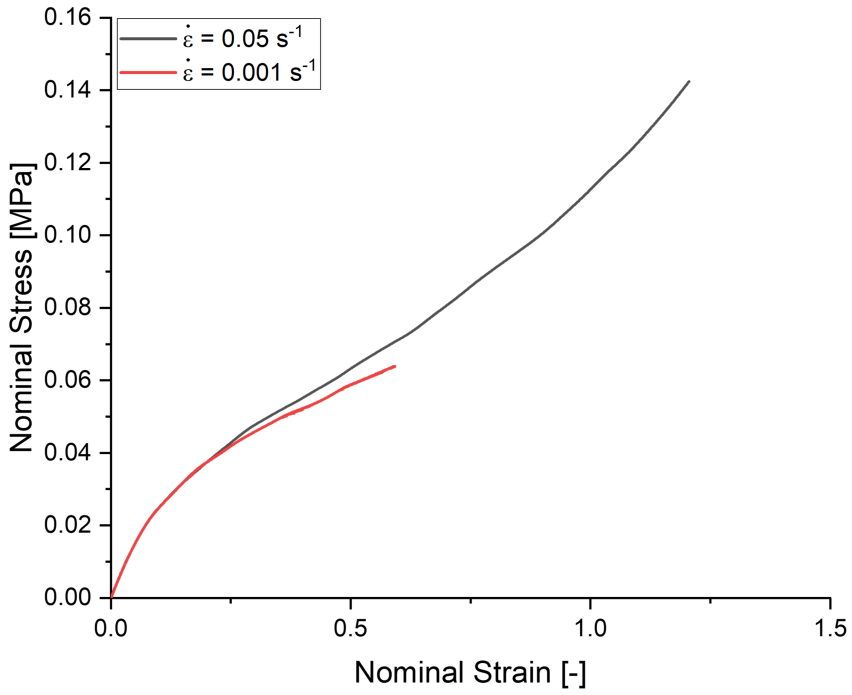

Figure 4.18: Nominal stress-strain curves of two different square shaped specimen tested at $\dot{\epsilon} = 0.05\ s^{-1}$ and $\dot{\epsilon} = 0.001\ s^{-1}$.

It is clear from the plot, that a negligible effect of strain rate is observed for $\epsilon < 0.3$, highlighting how the deformation state may play a role in the material response, whereas the curve for the specimen tested at $\dot{\epsilon} = 0.001\ s^{-1}$ seems to fall below the other for larger strains. Furthermore, it is evident how failure occurs at lower ultimate strains, which seems to suggest that an effect of strain rate may be present (although failure always starts from the holes, also in this case).

4.1.4. Comparison Between Deformation States

To summarize the results obtained during the study of the monotonic loading behaviour of Ecoflex 00-50 in different deformation states, an alternative way of representing stress-strain curves is presented in order to provide a clear comparison between experimental data, following the derivation shown in [1].

Recalling the derivation reported in Section 2.3.1, it can be proven that the total work of deformation for an ideal incompressible elastomer can be expressed as:

$$W = \frac{G}{2}\left(\lambda_1^2 + \lambda_2^2 + \frac{1}{\lambda_1^2\lambda_2^2} - 3\right) \tag{4.7}$$

And that the nominal stress-stretch relationship can be obtained by derivation of Eq. (4.7), as:

$$\sigma_1 = \left(\frac{\partial W}{\partial \lambda_1}\right) = G\left(\lambda_1 - \frac{1}{\lambda_1^3 \lambda_2^2}\right) \tag{4.8}$$

Recalling the relation between principal stretches for incompressible materials:

$$\lambda_1 \lambda_2 \lambda_3 = 1 \tag{4.9}$$

$$\lambda_3 = \frac{1}{\lambda_1 \lambda_2} \tag{4.10}$$

the first true principal stress can be expressed by combining Eq. (2.8) and (4.10), as:

$$\sigma_{t,1} = \lambda_1 \sigma_1 = G(\lambda_1^2 - \lambda_3^2) \tag{4.11}$$

A similar expression is obtained for $\sigma_{t,2}$ and, in the case of plane stress ($\sigma_{t,3} = 0$), the general true stress state is defined as:

$$\begin{cases} \sigma_{t,1} = G(\lambda_1^2 - \lambda_3^2) \\ \sigma_{t,2} = G(\lambda_2^2 - \lambda_3^2) \\ \sigma_{t,3} = 0 \end{cases} \tag{4.12}$$

The difference between the first and second true principal stresses will always be proportional to the difference between the first and second principal stretches squared:

$$\sigma_{t,1} - \sigma_{t,2} = G(\lambda_1^2 - \lambda_2^2) \tag{4.13}$$

In particular, for UT, PS and ET deformation states the expression is simplified to:

$$\begin{cases} \sigma_{t,1} - \sigma_{t,2} = G\left(\lambda_1^2 - \dfrac{1}{\lambda_1}\right) & for\ \boldsymbol{UT} \\ \sigma_{t,1} - \sigma_{t,2} = G\left(\lambda_1^2 - 1\right) & for\ \boldsymbol{PS} \\ \sigma_{t,1} - \sigma_{t,2} = G\left(\lambda_1^2 - \dfrac{1}{\lambda_1^4}\right) & for\ \boldsymbol{ET} \end{cases} \tag{4.14}$$

which can be expressed in terms of nominal stress and stretch as [1]:

$$\begin{cases} \sigma\lambda = G\left(\lambda^2 - \dfrac{1}{\lambda}\right) & for\ \boldsymbol{UT} \\ \sigma\lambda\left(1 - \dfrac{1}{\lambda^2+1}\right) = G\left(\lambda^2 - 1\right) & for\ \boldsymbol{PS} \\ \sigma\lambda = G\left(\lambda^2 - \dfrac{1}{\lambda^4}\right) & for\ \boldsymbol{ET} \end{cases} \tag{4.15}$$

As a first approximation, the available experimental averaged BT data (defined in Section 4.1.3) is treated according to the equibiaxial tension expression given in Eq. (4.15). Therefore, it is possible to represent experimental data obtained in the different deformation states on a common $(\sigma_{t,1} - \sigma_{t,2})$ vs $(\lambda_1^2 - \lambda_2^2)$ plot, as shown in Figure 4.19. The curves for PS and BT states correspond to specimen tested at $\dot{\epsilon} = 0.05\ s^{-1}$, whereas the curve for UT state corresponds to a specimen tested at $\dot{\epsilon} = 0.01\ s^{-1}$, since no strain rate influence is observed in this range (see Section 4.1.1).

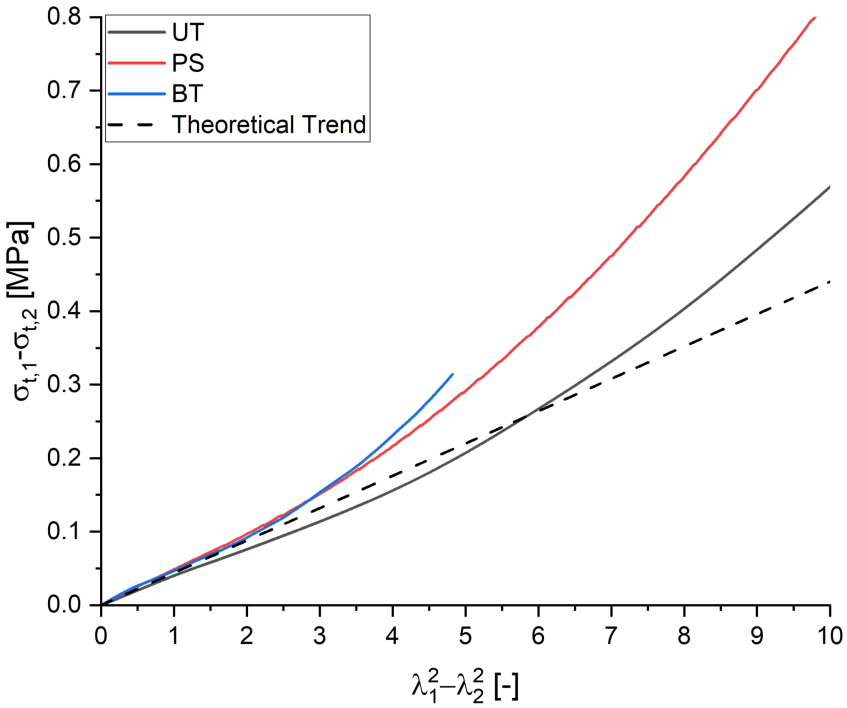

Figure 4.19: Comparison between different deformation states (Eq. (4.14)) and the theoretical trend (Eq. (4.13)).

It can be seen how all curves corresponding to the different deformation states converge to the theoretical linear trend (Eq. (4.13)) for $\lambda_1^2 - \lambda_2^2$ tending to zero. For the theoretical

trend the value of $G = 0.044$ MPa was used; the value was obtained from the Neo-Hookean fitting of experimental data, as illustrated in the following section.

4.1.5. Constitutive Modelling

In the previous sections, the experimental results obtained in uniaxial tension, pure shear and biaxial tension have been presented and discussed, highlighting how the material response can be divided into a strain rate independent portion (for low strains) and strain dependent region (for intermediate and high strains). Furthermore, depending on the deformation state, the value of shear modulus of the material presents discrepancies: this is indicative of how simultaneous fitting of the material response in different states could provide a better approximation of the real material behaviour.

As already introduced in Section 2.4, the total strain energy can be expressed as the sum of an elastic and viscous contributions; in [5, 42] the response of the material is described as the combination of an equilibrium (which identifies the strain rate independent region of the response) and an overstress (associated with the strain rate dependent region) portions. For modelling purposes, a stress contribution is associated to each region of the response: the equilibrium stress, σ_{EQ}, which is related to the elastic contribution of the strain energy, and the overstress, σ_{OV}, related to the viscous contribution; the complete material response is therefore described in terms of the sum of these two stress contributions.

Following the constitutive modelling approach reported in [42], the Neo-Hookean model for the equilibrium portion of the monotonic loading response of Ecoflex 00-50. The details on the derivation of the Neo-Hookean model have already been reported in Section 2.3.1, and therefore only the corresponding strain energy function (W_{NH}) is reported here:

$$W_{NH} = \frac{G}{2}(I_1 - 3) \tag{4.16}$$

where I_1 is the first stretch invariant which is equal to $\lambda_1^2 + \lambda_2^2 + \lambda_3^2$, being λ_i the principal stretches. It can be shown that the stress, as a function of the stretch, can be obtained from derivation of the strain energy function with respect to the applied stretch:

$$\sigma_{NH} = \left(\frac{\partial W_{NH}}{\partial \lambda}\right) = \frac{G}{2}\left(\frac{\partial I_1}{\partial \lambda}\right) \tag{4.17}$$

The expression of I_1 as a function of the applied λ depends on the specific deformation state under analysis. In Table 4.4 the constitutive relations, according to the Neo-Hookean

model, are reported for UT, PS and ET states. The details of the different deformations states can be found in Section 2.2.2 and Eqs. (2.13), (2.14) and (2.20). This model, being of the first order with respect to $(I_1 - 3)$, is very a basic and crude description of the material response and is able to approximate the material behaviour up to very limited strains (as shown in previous sections).

Table 4.4: First stretch invariant and stress expressions for uniaixal tension, pure shear and equibiaxial tension deformation states.

Deformation State	**First Stretch Invariant,** I_1	**Stress,** σ_{NH}
Uniaxial Tension	$\lambda^2 + \frac{2}{\lambda}$	$G\left(\lambda - \frac{1}{\lambda^2}\right)$
Pure Shear	$\lambda^2 + 1 + \frac{1}{\lambda^2}$	$G\left(\lambda - \frac{1}{\lambda^3}\right)$
Equibiaxial Tension	$2\lambda^2 + \frac{1}{\lambda^4}$	$G\left(\lambda - \frac{1}{\lambda^5}\right)$

In [42], the overstress contribution is modelled according to the Yeoh model, which is a third order hyperelastic phenomenological model, proposed originally in [56], in which the strain energy function takes the form:

$$W_Y = c_1(I_1 - 3) + c_2(I_1 - 3)^2 + c_3(I_1 - 3)^3 \tag{4.18}$$

where c_1, c_2 and c_3 are the material constants of the model which must be all positive.

Analogously to the Neo-Hookean model, the stress can be obtained from derivation of the strain energy function with respect to the applied stretch (as in Eq. (4.17)). Therefore, the stress expression for UT, PS and ET are respectively:

$$\sigma_{Y,UT} = 2\left(\lambda - \frac{1}{\lambda^2}\right)\left[c_1 + 2c_2(I_1 - 3) + 3c_3(I_1 - 3)^2\right] \tag{4.19}$$

$$\sigma_{Y,PS} = 2\left(\lambda - \frac{1}{\lambda^3}\right)\left[c_1 + 2c_2(I_1 - 3) + 3c_3(I_1 - 3)^2\right] \tag{4.20}$$

$$\sigma_{Y,ET} = 2\left(\lambda - \frac{1}{\lambda^5}\right)\left[c_1 + 2c_2(I_1 - 3) + 3c_3(I_1 - 3)^2\right] \tag{4.21}$$

where I_1 takes the expressions reported in Table 4.4 according to the different deformation states.

Since both models have been defined for the three deformation states examined during this thesis work, they can be combined in order to described the complete material response, as already proposed in [42]. The constitutive equation of the material, describing both the equilibrium and the overstress contributions of the material response, thus becomes:

$$\sigma = \sigma_{EQ} + \sigma_{OV} = \sigma_{NH} + \sigma_Y \tag{4.22}$$

$$\sigma = \left(\frac{\partial I_1}{\partial \lambda}\right)\left[G + 2c_1 + 4c_2(I_1 - 3) + 6c_3(I_1 - 3)^2\right] \tag{4.23}$$

As a first approximation, the available experimental averaged BT data (defined in Section 4.1.3) is fitted using the expression for equibiaxial tension reported in Table 4.4 for the Neo-Hookean model, and in Eq. (4.21) for the Yeoh model.

First of all, the equilibrium constant G was determined from experimental data through the use of least square curve-fitting approach (*lsqcurvefit*) built-in the commercially available software MATLAB. The accuracy of the method was verified by comparing the values obtained by fitting of UT, PS and BT data separately in MATLAB and OriginLab, by defining custom fitting functions. Since the results showed great agreement, it was decided to perform the simultaneous fitting of the data in the different deformation states in MATLAB.

The obtained value of shear modulus is $G = 0.044$ MPa, which is comparable to that reported in [42] of $G = 0.039$ MPa, obtained through the use of a Shore hardness amplification factor for only UT data. As expected, the obtained value is higher than $G_{UT} = 0.033$ MPa, obtained from the Neo-Hookean fitting of uniaxial tensile data in 4.1.1, and is lower than $G_{PS} = 0.049$ MPa, obtained from the equivalent simple shear state in Section 4.1.2. The comparison between experimental data and the Neo-Hookean model is reported in Figure 4.20.

It can be seen how, given the dispersion of experimental data, the model is able to correctly predict the equilibrium response in all three deformation states.

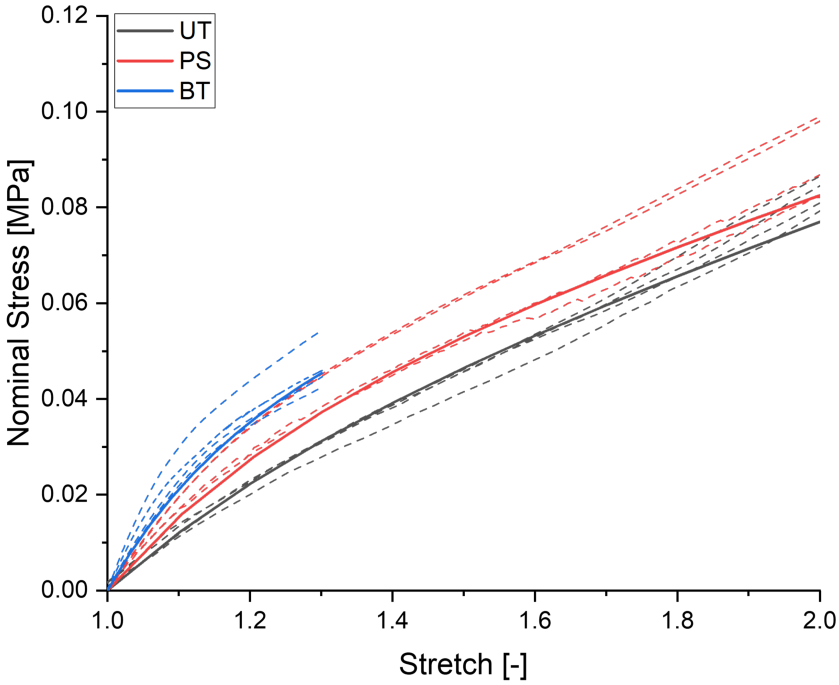

Figure 4.20: Experimental data (dashed lines) and Neo-Hookean fit with $G = 0.044$ MPa (continuous lines) comparison for UT, PS and BT deformation states.

Since the equilibrium parameter has been identified, it is now possible to determine the constants of the Yeoh model by simultaneous fitting of experimental data in different deformation states by means of Eq. (4.23). Also in this case fitting is performed through the use of least square curve-fitting approach (*lsqcurvefit*) built-in the commercially available software MATLAB. The fitting is performed up to $\lambda = 5$, as shown in [42] and the identified material parameters are reported in Table 4.5. A comparison between experimental data and the fitting model is reported in Figure 4.21.

Table 4.5: Identified material parameters from simultaneous fitting of UT, PS and BT data up to $\lambda = 5$.

Parameter	**Value**
c_1	2.22×10^{-14} MPa
c_2	8.02×10^{-4} MPa
c_3	0 MPa

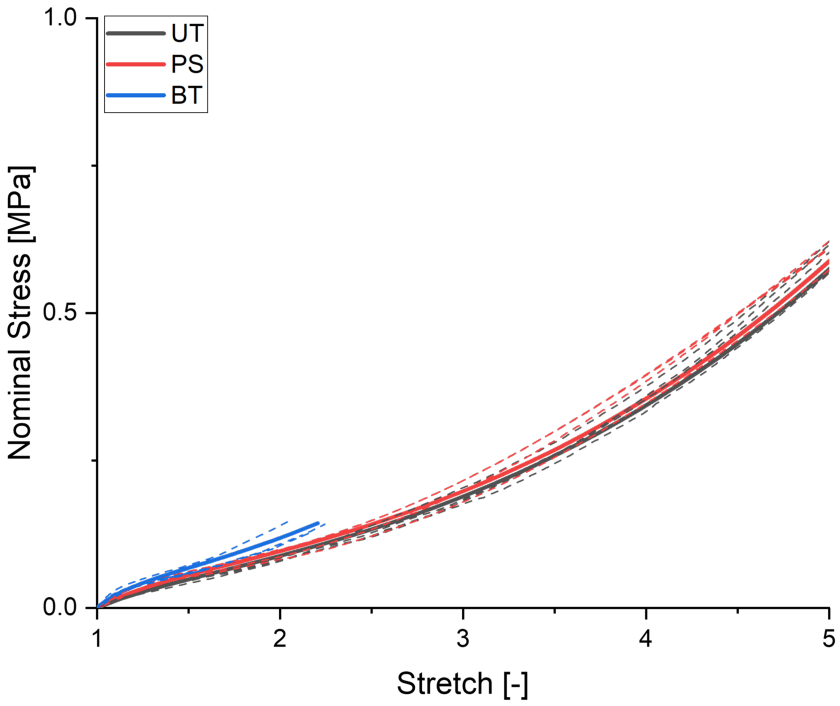

Figure 4.21: Experimental data (dashed lines) and Eq. (4.23) fit (continuous lines) comparison for UT, PS and BT deformation states up to $\lambda = 5$.

It can be seen how the proposed model is able to correctly predict the response in all three deformation states. It was decided to try performing the fitting up to $\lambda = 6$, in order to understand if it was possible to extend the applicability of the model up to failure. The newly identified material parameters are reported in Table 4.6 and a comparison between experimental data and the fitting model is reported in Figure 4.22.

Table 4.6: Identified material parameters from simultaneous fitting of UT, PS and BT data.

Parameter	**Value**
c_1	0.0121 MPa
c_2	0.0005 MPa
c_3	0 MPa

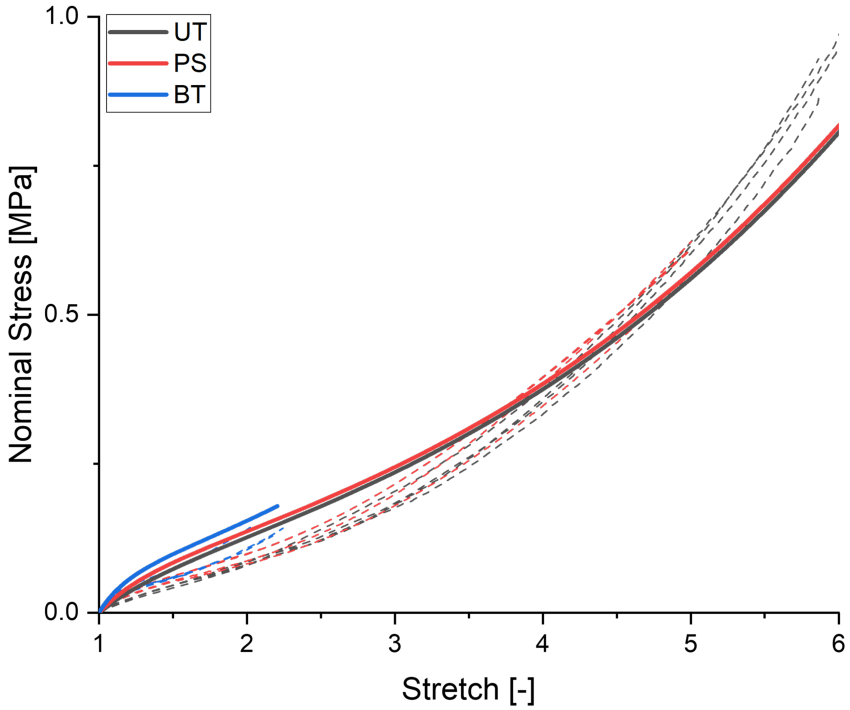

Figure 4.22: Experimental data (dashed lines) and Eq. (4.23) fit (continuous lines) comparison for UT, PS and BT deformation states.

It can be seen how, by extending the fitting range up to $\lambda = 6$, the model overestimates the real material response in both UT and PS states, especially at low stretch. On the other hand, the model is still able to predict the response in BT state with good accuracy. It was therefore concluded that the combined Neo-Hookean and Yeoh model proposed is able to correctly predict the material behaviour up to moderate strain levels, whereas it fails to predict the total material response. Finally, it should be remarked how the model does not include a prediction of the strain rate effect on the overstress response, since both constitutive models adopted are hyperelastic and therefore the viscous contribution to the material response is not considered. Furthermore, both models assume incompressibility of the material, which may not be the case of Ecoflex 00-50, as proven by Poisson ratio estimation. Therefore, in the future, a more suitable constitutive model should be developed to encompass the viscoelastic nature and compressibility of Ecoflex 00-50.

4.2. Cyclic Tensile Tests

4.2.1. Uniaxial Tension Cyclic Tests

The cyclic loading behaviour of Ecoflex 00-50 was investigated by performing multiple loading-unloading uniaxial tensile tests for different values of the applied strain. For each strain, ten loading-unloading cycles were performed. Figure 4.23 reports a few of the loading-unloading curves for a 10 cycles cyclic loading test performed up to $\epsilon = 5$ at $\dot{\epsilon} = 0.01\ s^{-1}$.

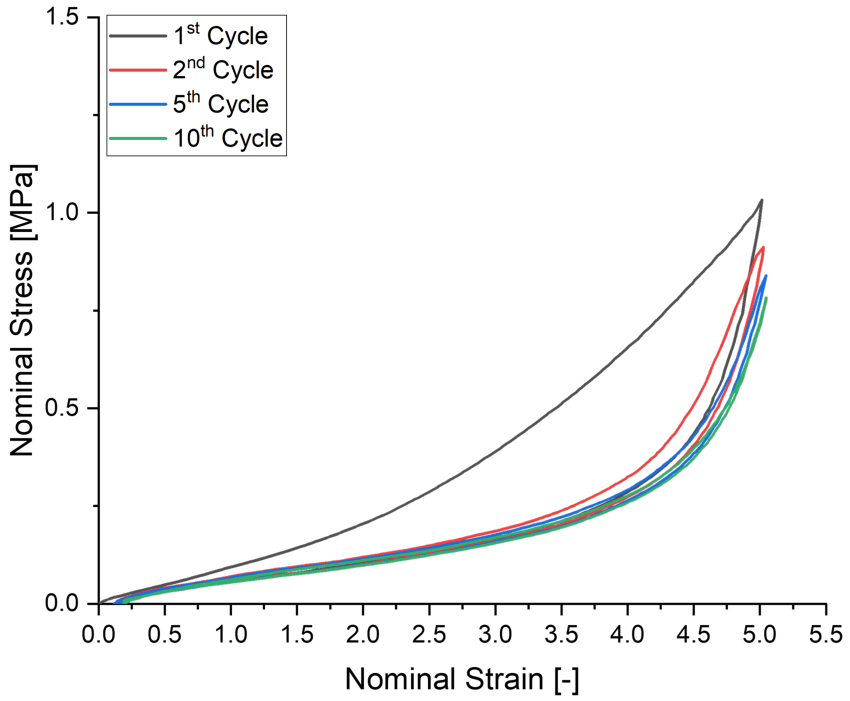

Figure 4.23: Nominal stress-strain plot of a 10 cycles cycle loading test at $\dot{\epsilon} = 0.01\ s^{-1}$. The curves are relevant to the first, second, fifth and tenth loading-unloading cycles

It can be seen how the loading and unloading paths of a cycle do not coincide, suggesting an hysteretical (that is dissipative) behavior of the material. The hysteresis decreases moving from the first to the tenth cycle. In order to quantify the dissipation magnitude, the dissipated energy density (w_d) is calculated by integration of the area between the loading and unloading paths, whereas the elastically stored energy density (w_e) is calculated by integration of the area beneath the unloading path (as shown in Figure 4.24). The sum of the two contributions is the total energy density (w_{tot}) associated with the loading-unloading cycle:

$$w_{tot} = w_d + w_e = \left(\int_l \sigma d\epsilon - \int_{ul} \sigma d\epsilon \right) + \int_{ul} \sigma d\epsilon = \int_l \sigma d\epsilon \tag{4.24}$$

where the subscripts l and ul identify the loading and unloading paths, respectively. The trends of the total, elastically stored and dissipated energy densities as a function of the cycle number are shown in Figure 4.25. Furthermore, residual deformation can be observed upon unloading the specimen, whose value slightly fluctuates with the cycle number. The value of residual strain observed in this case is $\epsilon_{res} = 0.15 \pm 0.02$.

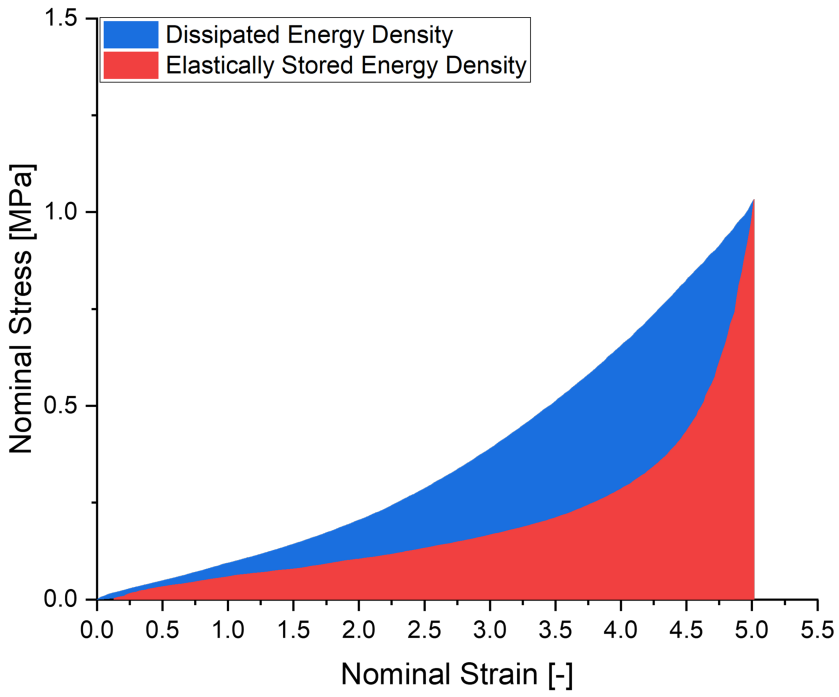

Figure 4.24: Identification of dissipated and elastically stored energy densities from nominal stress-strain curve.

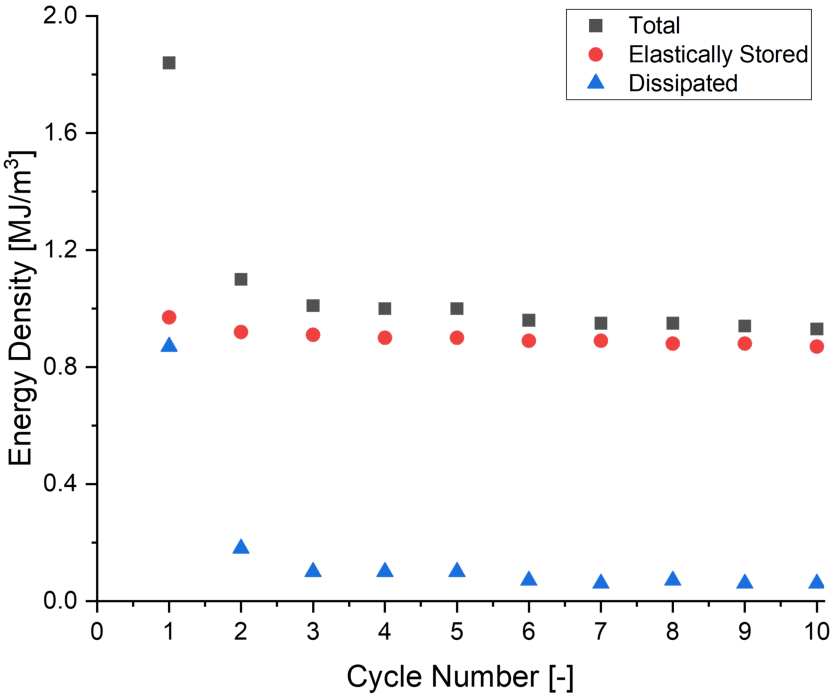

Figure 4.25: Total, dissipated and elastically stored energy densities vs cycle number plot for a UT specimen subjected to cyclic loading up to $\epsilon = 5$ at $\dot{\epsilon} = 0.01\ s^{-1}$.

Strain-induced stress softening (or Mullins effect) is present and it is evident how it mainly occurs during the first loading cycle. The trend of the maximum stress (at $\epsilon = 5$) as a function of the cycle number is shown in Figure 4.26.

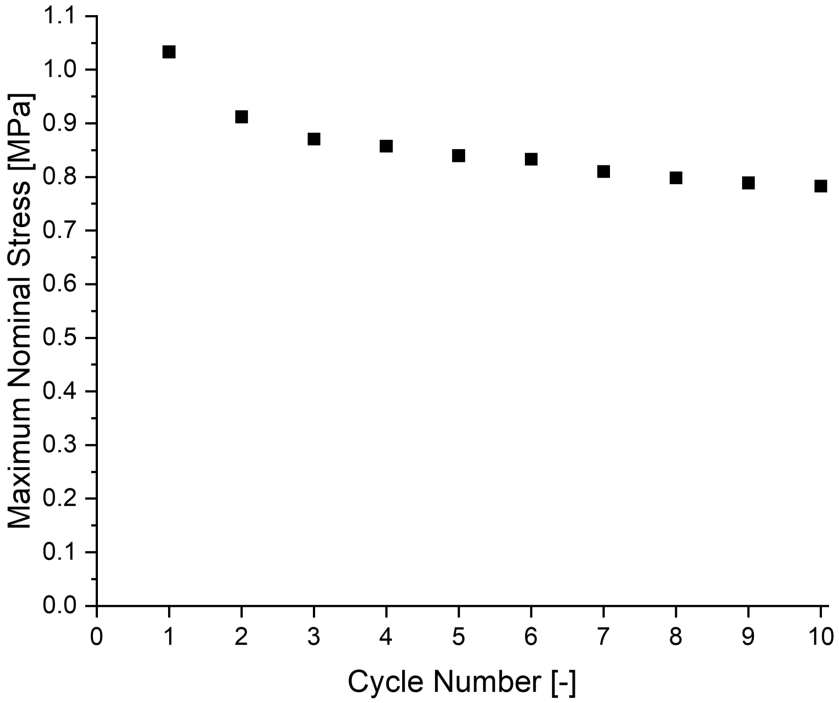

Figure 4.26: Maximum stress vs cycle number plot for a UT specimen subjected to cyclic loading up to $\epsilon = 5$ at $\dot{\epsilon} = 0.01\ s^{-1}$.

After the fifth cycle, the dissipated energy density becomes constant and the maximum stress is reduced by less than 5% between two subsequent cycles (which is considered a negligible reduction), identifying the stabilized cyclic response of the material. For this reason, it was decided to perform only 5 cycles in subsequent tests.

To further investigate cyclic response of the material and to allow modelling of the stress softening phenomenon (see Section 4.2.3), cyclic loading-unloading tests were performed at different imposed maximum crosshead displacements, corresponding to $\epsilon \approx 1$, $\epsilon \approx 2$, $\epsilon \approx 3$ and $\epsilon \approx 4$. Some degree of variability exists between maximum strains reached during testing, although the corresponding crosshead maximum displacement is fixed: this is because the material, being very soft, would squeeze out of the clamping system in an inhomogeneous way, resulting in a slightly different gauge length for each test. The first cycle nominal stress-strain curve for several UT specimens subjected to cyclic loading up to different nominal strain are reported in Figure 4.27.

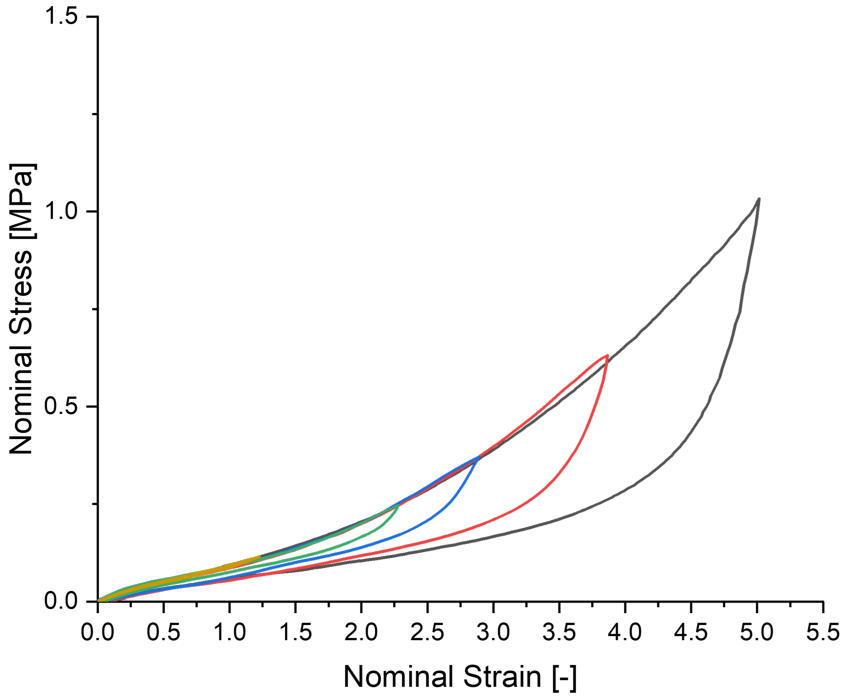

Figure 4.27: Nominal stress-strain plot of first loading-unloading cycle performed on UT specimens up to different strains at $\dot{\epsilon} = 0.01\ s^{-1}$.

As expected, hysteresis area, maximum stress and residual deformation increase with increasing imposed strain level. In particular, for $\epsilon \approx 1$, the loading and unloading path are nearly superimposed and the resulting hysteresis area is nearly zero. The values of residual strain after the first cycle follow a quasi-linear trend with respect to the imposed maximum strain, as shown in Figure 4.28.

The maximum stress and dissipated energy fraction (obtained as w_d/w_{tot}) as a function of the cycle number, for applied strains, are reported in Figure 4.29 and Figure 4.30, respectively.

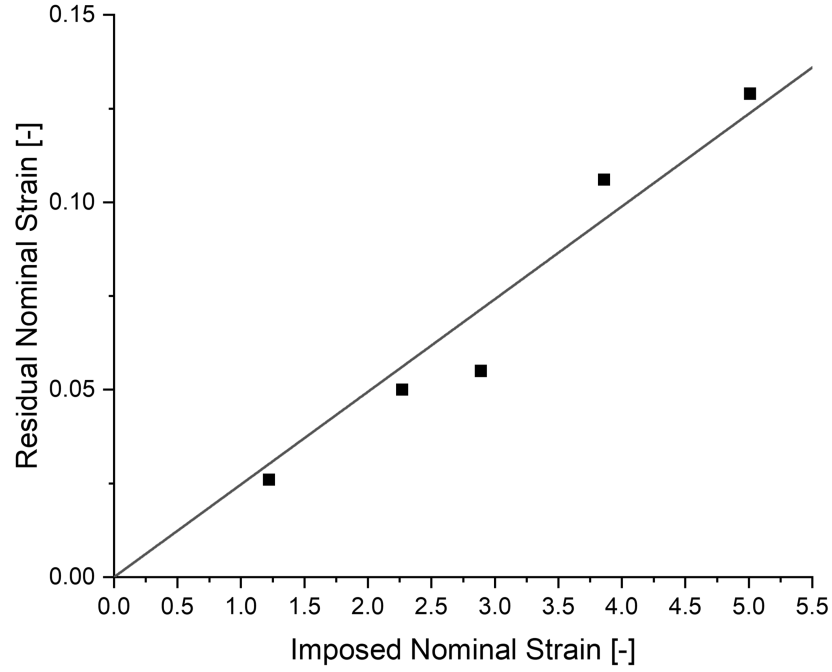

Figure 4.28: Residual strain at the end of the first loading-unloading cycle for specimens tested up to different strains, at $\dot{\epsilon} = 0.01\ s^{-1}$.

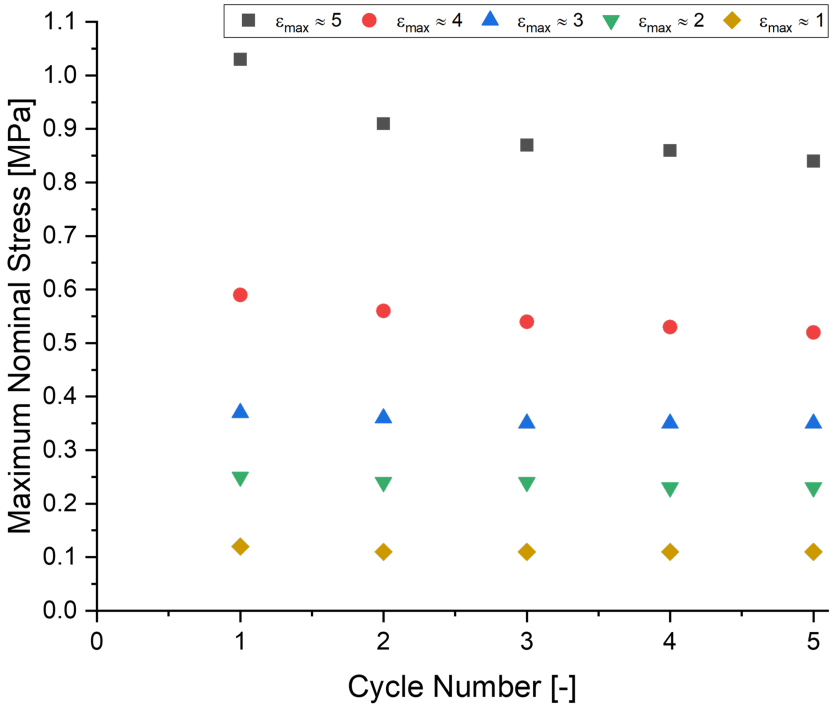

Figure 4.29: Maximum stress vs cycle number plot for specimens subjected to cyclic loading up to different strains, tested at $\dot{\epsilon} = 0.01\ s^{-1}$.

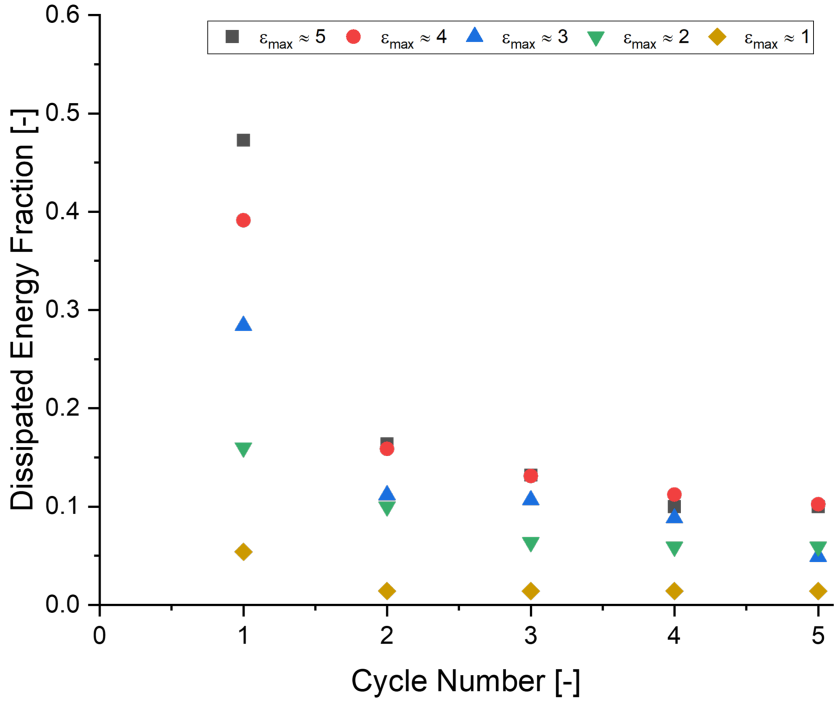

Figure 4.30: Dissipated energy fraction vs cycle number plot for specimens subjected to cyclic loading up to different strains, tested at $\dot{\epsilon} = 0.01\ s^{-1}$.

As already mentioned, up to $\epsilon \approx 1$ energy dissipation phenomena are very limited, and no changes are observed in dissipated energy density and maximum stress after the first cycle. Therefore, in the low-strain region of the material response (up to $\epsilon \approx 1$ for UT tests) negligible softening is observed upon reloading. On the contrary, for larger strains, an increase in both stress softening and dissipation are observed with increasing strain. These last observations are in agreement with the results reported in [5, 42], although no residual deformation was reported.

In order to model the cyclic loading-unloading response of the material (as will be shown in Section 4.2.3), the total and elastically stored energy density components need to be determined from the first loading-unloading cycle. The trends of the total, dissipated and elastically stored energy densities for the first cycle, as a function of the nominal strain, obtained from cyclic tests performed at $\dot{\epsilon} = 0.1\ s^{-1}$ and $\dot{\epsilon} = 0.01\ s^{-1}$, are reported in Figure 4.31. Since no data are available in literature regarding the energy density trends for Ecoflex 00-50, experimental data were fitted using a power-law equation, determined by comparing different functions, which is in the form:

$$w = a\epsilon^b \tag{4.25}$$

where a and b are the two power-law coefficients. The coefficients for each energy density curve are reported in Table 4.7.

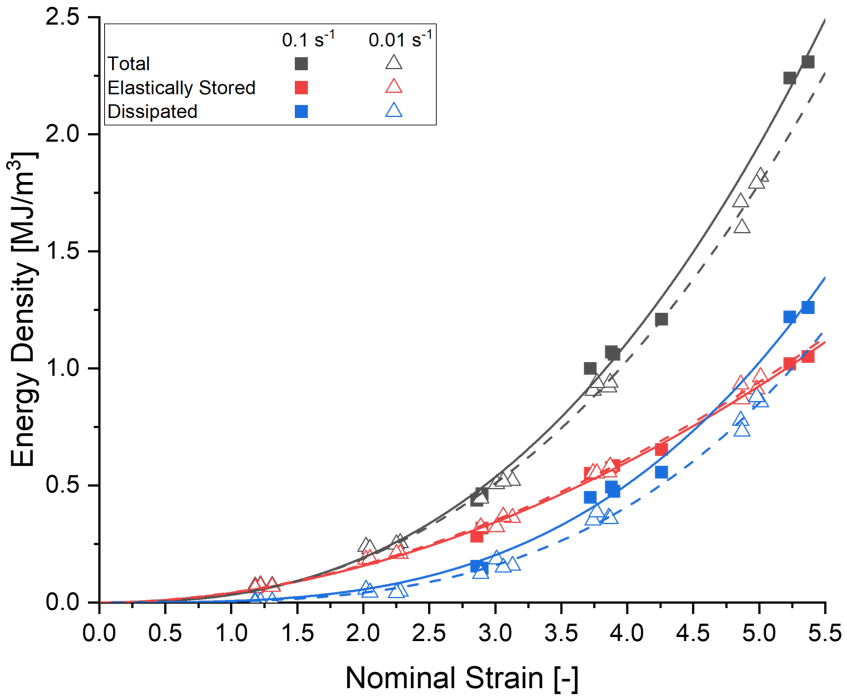

Figure 4.31: Total, dissipated and elastically stored energy densities relevant to the first cycle and power-law fitting (continuous and dashed lines) vs nominal strain plot for several UT specimens subjected to cyclic tests at $\dot{\epsilon} = 0.1\ s^{-1}$ and $\dot{\epsilon} = 0.01\ s^{-1}$.

Table 4.7: Power-law coefficients determined by fitting of energy densities experimental data, obtained from UT specimen tested at $\dot{\epsilon} = 0.01\ s^{-1}$ and $\dot{\epsilon} = 0.1\ s^{-1}$.

$\dot{\epsilon}\ [s^{-1}]$		w_{tot}	w_s	w_d
0.01	a $[MJ/m^3]$	0.0342 ± 0.0023	0.0423 ± 0.0024	0.0043 ± 0.0006
	b [-]	2.46 ± 0.05	1.93 ± 0.04	3.29 ± 0.09
0.1	a $[MJ/m^3]$	0.033 ± 0.005	0.041 ± 0.004	0.006 ± 0.001
	b [-]	2.53 ± 0.09	1.93 ± 0.06	3.18 ± 0.15

Considering the experimental data obtained at $\dot{\epsilon} = 0.01\ s^{-1}$, it is evident how both energy density components increase with increasing the applied strain. In particular, the dissipated energy density reaches zero at $\epsilon \approx 1.2$, suggesting that for lower strains no energy dissipation occurs. Furthermore, it can be seen how w_d remains almost half of w_s between $\epsilon = 2$ and $\epsilon = 4$, but for larger strain levels the dissipated component becomes almost equal to the elastically stored one.

As reported in Section 4.1.1, an increase of strain rate leads to an increase of stress in the time-dependent region of the material response, and this effect is valid also during cyclic loading, which is the same behaviour observed during monotonic loading. Tests at 0.1 s^{-1} were performed only at strains larger than $\epsilon = 3$, in order to investigate the strain rate dependent region of the material response. No net increase of energy is associated with an increase of strain rate. Furthermore, it can be seen that the dissipated energy trend is different with respect to that obtained from tests at $\dot{\epsilon} = 0.01\ s^{-1}$, as w_d and w_s become comparable at $\epsilon \approx 4$, whereas for larger strain levels the dissipated component becomes larger than the elastically stored one. The physical reason behind this phenomenon needs further investigation.

Stress Recovery

The so called recovery test was performed on UT specimens that were stretched up to $\epsilon \approx 4$ and after the unloading to zero stress, they were removed from the testing machine. The material was let recover for a certain amount of time (recovery time) and loaded-unloaded to and from the same strain. Different recovery times were investigated, namely **1 day**, **1 week** and **1 month**. The nominal stress-strain curves, relevant to the first cycle (on the pristine material) and relevant to second cycle, performed after each recovery time, are reported in Figure 4.32.

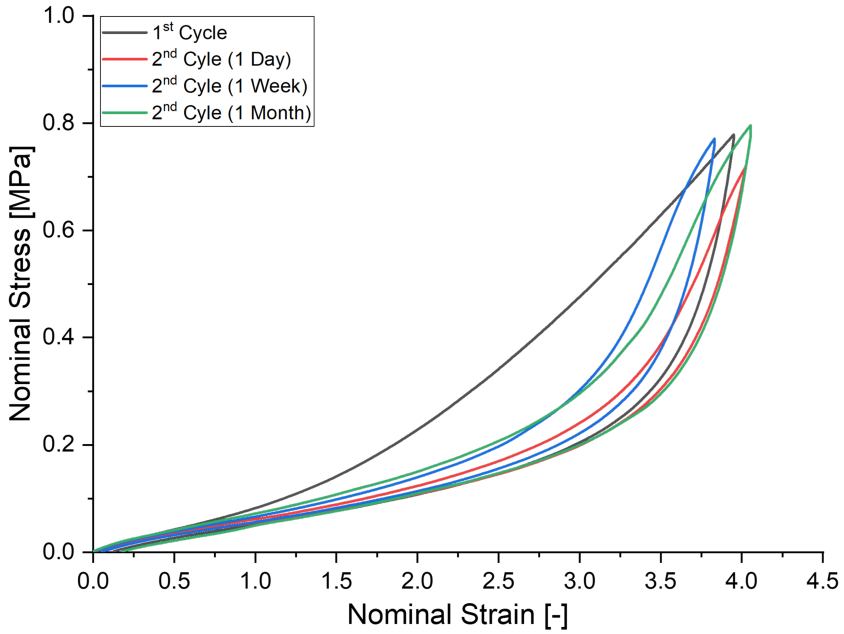

Figure 4.32: Nominal stress-strain curves relevant to the first and second cycle, obtained from cyclic tensile tests performed on different UT specimens, tested after different recovery times at $\dot{\epsilon} = 0.01\ s^{-1}$.

For each recovery time, four different specimen were tested. Before performing the second loading-unloading cycle, the residual strain was monitored by measuring the specimen length at fixed time intervals: an almost complete recovery was observed two weeks after the first cyclic loading-unloading test. The dissipated energy density was determined for both the first ($w_{d,0}$) and second ($w_{d,r}$) cycle as the area between the loading and unloading paths. The dissipated energy ratio, obtained as $w_{d,r}/w_{d,0}$, is reported as a function of the recovery time in Figure 4.33.

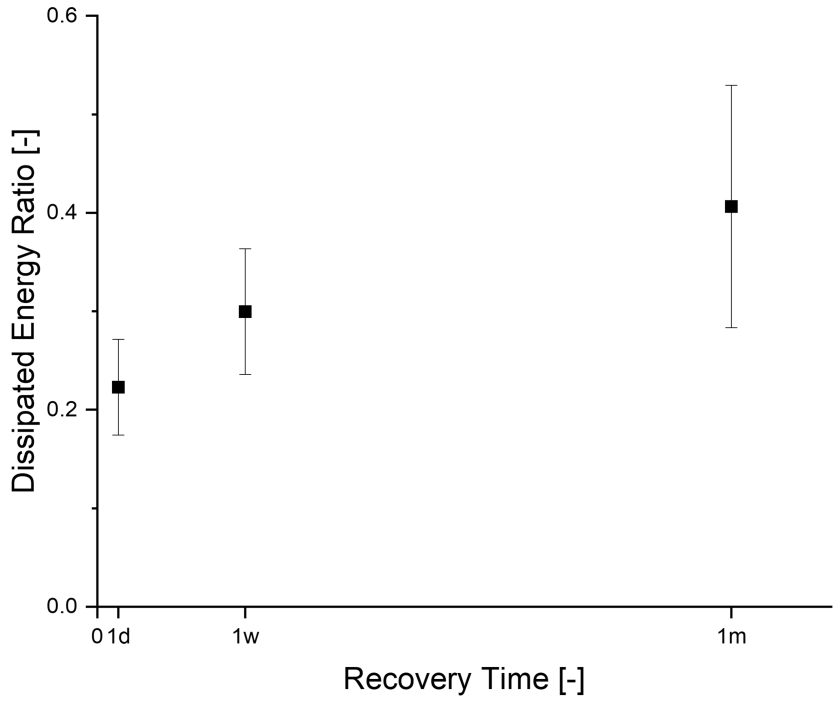

Figure 4.33: Dissipated energy ratio ($w_{d,r}/w_{d,0}$) vs recovery time plot. Data obtained 1 day ($1d$), 1 week ($1w$), and 1 month ($1m$) after the first cyclic test.

Despite the data scattering, an increasing trend of dissipated energy ratio is observed with the increase of the recovery time, as already noticed in [43] for Ecoflex 00-30, suggesting how the material is able to recover the strain induced structural changes.

The observed data scattering is mainly related to the fact that tests were performed controlling the maximum crosshead displacement, which is fixed for the first and second cyclic tests, but the effective gauge length can be different, since strains are determined from video recordings (see Section 3.2.2), and therefore some differences are noticed in the maximum strain level reached during the primary and the secondary cycles, as shown in Figure 4.32.

4.2.2. Pure Shear and Biaxial Tension Cyclic Tests

Pure Shear Cyclic Tests

Results similar to those obtained from uniaxial tensile cyclic tests were obtained also from the pure shear cyclic tests. Since reporting an in-depth study also for this deformation state would be repetitive, only the main results, which are of interest for modelling the material cyclic response, are reported and commented in the following.

The first cycle nominal stress-strain curve for several PS specimens subjected to cyclic loading at different strains are reported in Figure 4.34. Also in this case, hysteresis area, maximum stress and residual deformation increase, increasing the applied strain.

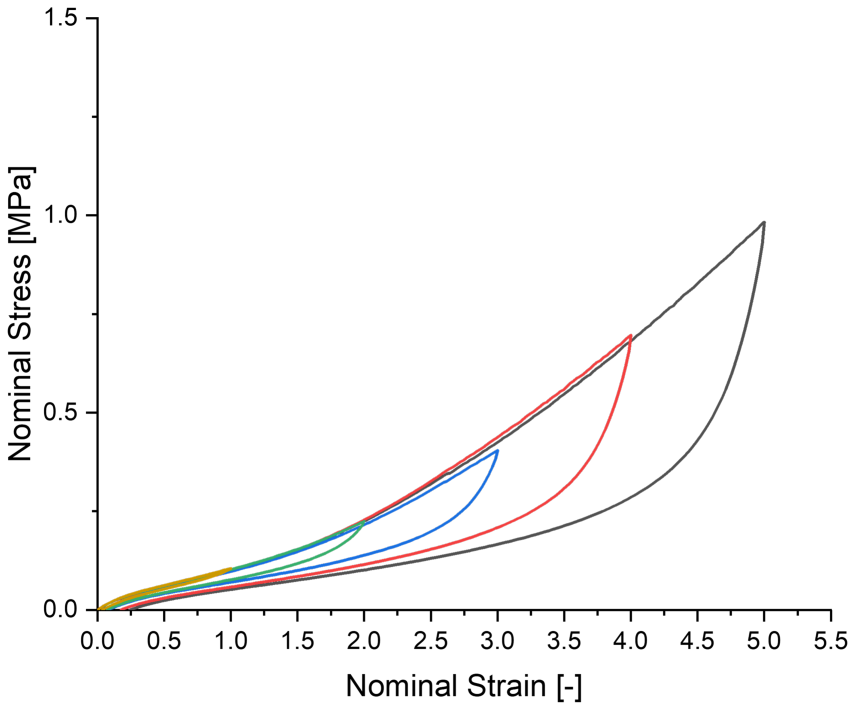

Figure 4.34: Nominal stress-strain plot of first loading-unloading cycle performed on several PS specimen up to different strains, tested at $\dot{\epsilon} = 0.1\ s^{-1}$.

All the specimens tested at $\epsilon = 5$ failed after the second loading-unloading cycle. For the cyclic tensile test in PS state too, for strains up to $\epsilon = 1$, the hysteresis area is almost negligible.

The total, elastically stored and dissipated energy densities relevant to the first cycle are reported in Figure 4.35 as a function of the nominal strain, obtained from cyclic tests performed at $\dot{\epsilon} = 0.1\ s^{-1}$ and at $\dot{\epsilon} = 0.01\ s^{-1}$. Analogously to what has been reported in Section 4.2.1 for UT cyclic tests, experimental data were fitted using a power-law equation

and the obtained coefficients are reported in Table 4.8. It should be noted that no data for $\epsilon = 5$ at $\dot{\epsilon} = 0.01\ s^{-1}$ are reported because of premature failure of the specimen tested, during the unloading of the first cycle.

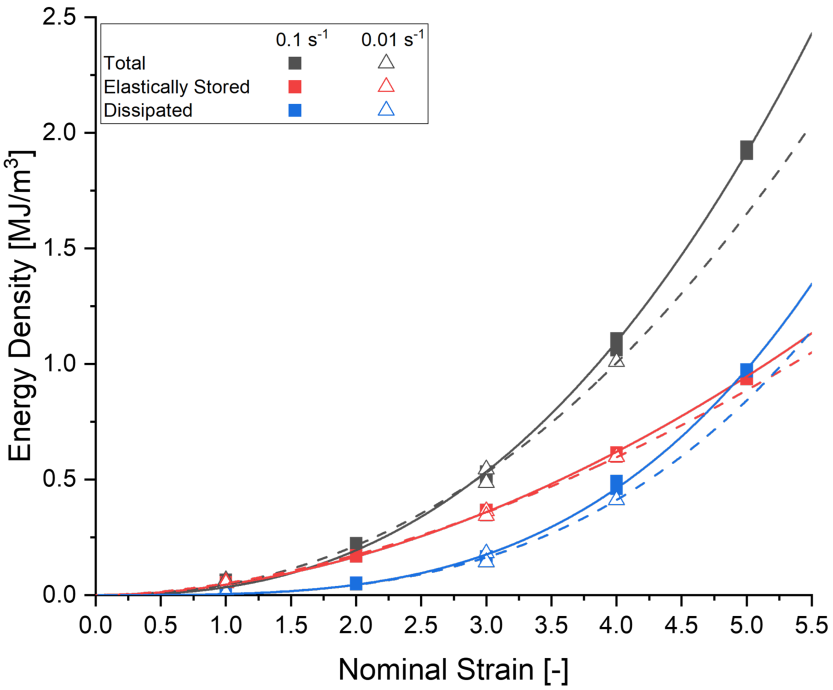

Figure 4.35: Total, dissipated and elastically stored energy densities relevant to the first cycle and power-law fitting (continuous and dashed lines) vs nominal strain plot for several PS specimens subjected to cyclic tests at $\dot{\epsilon} = 0.1\ s^{-1}$ and $\dot{\epsilon} = 0.01\ s^{-1}$.

Table 4.8: Power-law coefficients determined by fitting of energy densities experimental data, obtained from PS specimen tested at $\dot{\epsilon} = 0.01\ s^{-1}$ and $\dot{\epsilon} = 0.1\ s^{-1}$.

$\dot{\epsilon}\ [s^{-1}]$		w_{tot}	w_s	w_d
0.01	a $[MJ/m^3]$	0.046 ± 0.006	0.051 ± 0.003	0.005 ± 0.001
	b [-]	2.23 ± 0.10	1.78 ± 0.04	3.21 ± 0.18
0.1	a $[MJ/m^3]$	0.0343 ± 0.0020	0.0448 ± 0.0016	0.0044 ± 0.0004
	b [-]	2.49 ± 0.04	1.89 ± 0.02	3.36 ± 0.06

The trends of both energy density components are very similar to those observed for UT cyclic tests in Section 4.2.1, where the dissipated component reaches zero value at $\epsilon = 1$ and is approximately half the elastically stored energy density for strains between $\epsilon = 2$ and $\epsilon = 4$. Furthermore, the strain rate has a very limited effect on the energy density

components, since a very slight variation is observed only at $\epsilon = 4$, whereas for lower strain the two components values are almost identical for the two strain rates considered.

Finally, the elastically stored (w_s/w_{tot}) and dissipated energy fractions (w_d/w_{tot}) are used to compare UT and PS energy density trends, since a direct comparison between the energy density components is unfeasible because of the different state of deformation. The results, obtained from tests performed at $\dot{\epsilon} = 0.01\ s^{-1}$, are reported in Figure 4.36.

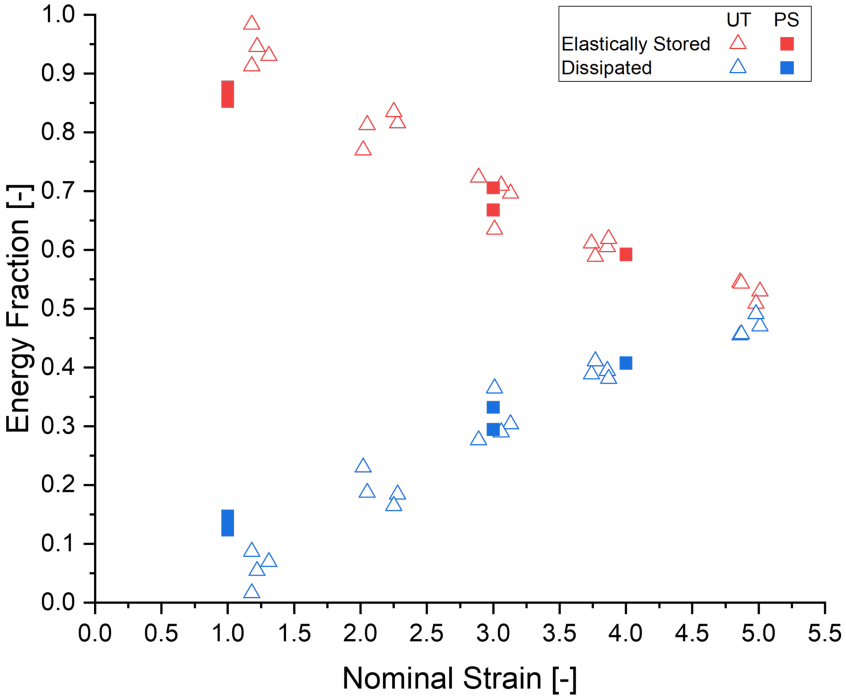

Figure 4.36: Elastically stored (red) and dissipated (blue) energy fractions relevant to the first cycle for UT (triangles) and PS (squares) specimens subjected to cyclic tests at $\dot{\epsilon} = 0.01\ s^{-1}$.

It can be seen that, for both deformation states, the two energy fractions follow a linear trend, which is decreasing for the elastically stored energy fraction and decreasing for the dissipated one. In particular, it can be seen that for both states w_s/w_{tot} is close to 1 for $\epsilon \approx 1$, highlighting how negligible dissipation occurs below this strain. The values of the energy fractions become comparable for the two deformation states for $3 \leq \epsilon \leq 4$. Overall the greatest difference between the two deformation states is present for $\epsilon \approx 1$, where a slightly larger dissipated fraction is observed for the PS specimens, compared to the UT ones.

Biaxial Tension Cyclic Tests

Because of the limited extensibility of Ecoflex 00-50 in biaxial tension deformation state (see Section 4.1.3), cyclic tests were performed only up to $\epsilon \approx 1$ imposed maximum strain, in both stretching directions. Only five cycles were performed during testing.

Only the first cycle nominal stress-strain curves obtained from the stress and strain measured the x and y directions, for a BT specimen subjected to cyclic loading at $\dot{\epsilon} = 0.05\ s^{-1}$, are reported in Figure 4.37.

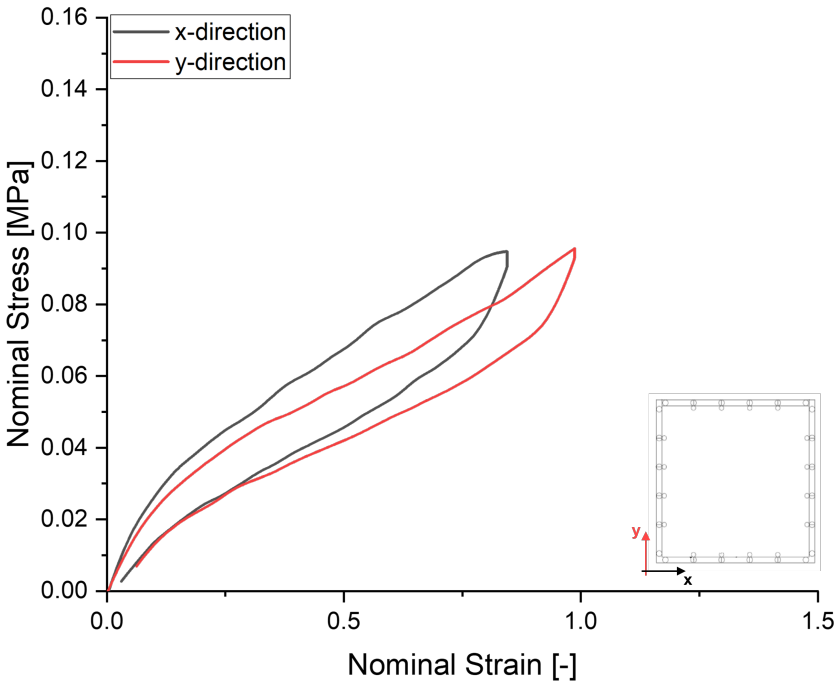

Figure 4.37: Nominal stress-strain curves in the x and y directions of the first cycle performed on a BT specimen tested at $\dot{\epsilon} = 0.05\ s^{-1}$.

Because of the testing setup sensitivity, the stress never reaches zero upon unloading, therefore a strain is observed after unloading which is not indicative of the real residual strain. Differently to what observed for the to UT and PS cyclic tests, energy dissipation is not negligible in the cyclic BT test, not even for the small values of the applied strain; this is in agreement with the observations reported in Section 4.1.3, where the strain rate-independent region of the material response in BT states is limited to $\epsilon = 0.3$, highlighting how the deformation state plays a role in the material response. The values of total, elastically stored and dissipated energy densities evaluated from the stress-strain data in the x or in the y directions are reported in Table 4.9.

As previously said, the test is not an actual equibiaxial tensile test. Therefore the hys-

teresis areas in the two direction are different, as the overall strain and thus the total strain energy. Because of the lower maximum strain level reached, the dissipated energy fraction resulted to be higher in the x direction.

Table 4.9: Total, elastically stored and dissipated energy densities in the x and y directions, obtained from the first cycle of a BT specimen tested at $\dot{\epsilon} = 0.05\ s^{-1}$.

	x-direction	**y-direction**
ϵ_{max} [-]	0.84	0.98
w_{tot} $[MJ/m^3]$	0.049	0.054
w_s $[MJ/m^3]$	0.034	0.041
w_d $[MJ/m^3]$	0.015	0.013
w_d/w_{tot} [%]	31	24

4.2.3. Loading-Unloading Modelling

In Section 4.1.5, a constitutive model for Ecoflex 00-50 has been proposed, based on the experimental results obtained during this thesis work and the observations reported in [42]. The model is able to predict the material monotonic response up to moderate strain levels ($\lambda \approx 5$ corresponding to $\epsilon \approx 4$) and is based on a combination of the Neo-Hookean and Yeoh models. In order to model the loading-unloading response of the material, an approach based on the Ogden-Roxburgh [57] pseudo-elastic phenomenological model is proposed in [42] for other Ecoflex materials, and its applicability is discussed in this section. The model was originally proposed to extend the concept, and therefore the description, of hyperelasticity to stress softening phenomena and to describe the unloading and reloading paths of cyclic tests, which are equivalent for an ideal softening [14]. The model can be extended to describe the cyclic behaviour of real elastomers, where unloading and reloading paths are not equivalent, as shown in [58].

From a modelling point of view, it is important to notice that stress softening and dissipation phenomena affect only the overstress portion of the material response (at high strains), whereas the equilibrium portion (at low strains) remains unaltered during cyclic loading, as observed in Section 4.1.5 (the two portions of the response have been defined in 4.1.5).

An additional parameter is added to the already existing model, η, which is the ratio between the energy density of the primary loading path (w_0, corresponding to the total energy density obtained from cyclic tests) and of the primary unloading path (w, corresponding to the elastically stored energy density obtained from cyclic tests). Therefore,

the energy density of the unloading path can be expressed as:

$$w\left(I_1,\eta\right)=\eta w_0\left(I_1\right)+\phi(\eta) \tag{4.26}$$

where $\phi(\eta)$ is a dissipation function which denotes the energy dissipation responsible of the softening. In particular $\eta=1$ denotes the primary loading path, which implies that $\phi(1)=0$. Furthermore, it can be proven that:

$$\sigma=\eta\sigma_0 \tag{4.27}$$

where σ_0 denotes the nominal stress in the primary loading path, which is obtained form the proposed Neo-Hookean and Yeoh model, and σ is the stress in the unloading path. Combining Eq. (4.27) with the constitutive model presented previously, the following relationship is obtained:

$$\sigma=\left\{G+\eta\left[2c_1+4c_2\left(I_1-3\right)\right]\right\}\left(\frac{\partial I_1}{\partial\lambda}\right) \tag{4.28}$$

where G, c_1 and c_2 are the material parameters of the Neo-Hookean and Yeoh models, reproducing the primary loading response. Following [42, 58], the explicit expression for the η parameter is chosen to be:

$$\eta=1-\frac{1}{r}\tanh\left(\frac{w_{max}-w_0(\lambda)}{m}\right) \tag{4.29}$$

where r and m are two parameters which must have positive values (and in particular $r\geq 1$), w_{max} denotes the total energy density in the primary loading at the instant when an unloading initiates (i.e. $w_{max}=max\{w_0(\lambda)\}$ on the primary loading path) and $w_0(\lambda)$ denotes the energy density in the unloading, which is a function of λ.

Fitting was performed on the data from the primary unloading path of cyclic UT tests up to $\lambda\approx 5$, through the use of least square curve-fitting approach (*lsqcurvefit*) built-in the commercially available software MATLAB, in order to verify reliability of the model. The two identified parameters are reported in Table 4.10 and the comparison between experimental data and the model is reported in Figure 4.38.

Table 4.10: Identified Ogden-Roxburgh parameters from fitting of UT unloading data.

Parameter	Value
r [-]	1.00
m [-]	1.72

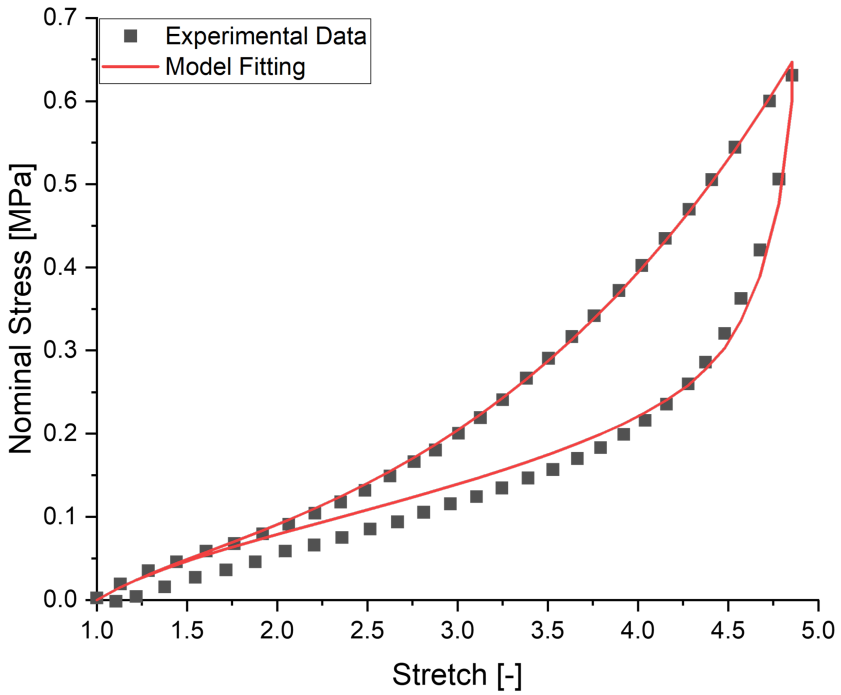

Figure 4.38: Comparison between UT cyclic experimental data (black dots) and model fitting from Eq. (4.28) (red line).

It can be seen how the model is able to correctly describe the response of Ecoflex 00-50 during loading, as already observed in Section 4.1.5, but overestimates the material response during unloading for $\lambda < 3.5$. The overestimation was expected, because the model does not take into account the presence of residual deformation at the end of unloading and, as a matter of fact, the model predicts a null stress for $\lambda = 1$ which is not the case, as observed in previous sections (in this particular case the stress is null at $\lambda = 1.11$). A modified version of the Ogden-Roxburgh model, which effectively takes into account the presence of residual strain is reported in [32], but no explicit expression for the additional parameters introduced is present in literature.

Therefore, it was concluded that the model proposed in [42] is not a suitable prediction of the cyclic response of Ecoflex 00-50 and, in the future, a more complete description of the stress softening behaviour of the material needs to be developed.

4.3. Temperature Effects

4.3.1. Tensile Behaviour Dependence on Test Temperature

In this last chapter, the testing temperature effect on the material response is investigated. Different temperatures were considered, namely -40°C, -20°C, 0°C, 23°C, 60°C, 80°C, 100°C and 140°C. This temperature range was chosen in order to have a direct comparison with already available data, present in [5, 42] for Ecoflex 00-30. The upper limit was fixed to avoid the material degradation during testing, from the results reported in Section 3.1.3. For each temperature, four strip specimen (described in Section 3.2.4) were tested at $\dot{\epsilon} = 0.1\ s^{-1}$ after conditioning for 15 minutes.

The nominal stress-strain curves obtained for each testing temperature are reported in Figure 4.39. In order to compare the material behaviour at different temperatures, the highest and lowest experimental nominal stress-strain curves with variability intervals (the area between the two curves) for each test are reported in Figure 4.40. This representation of data is used to highlight the differences in the material response caused by different testing temperatures and ultimate stress and strain, which will be analyzed in detail in the following sections, are not considered meaningful in this representation.

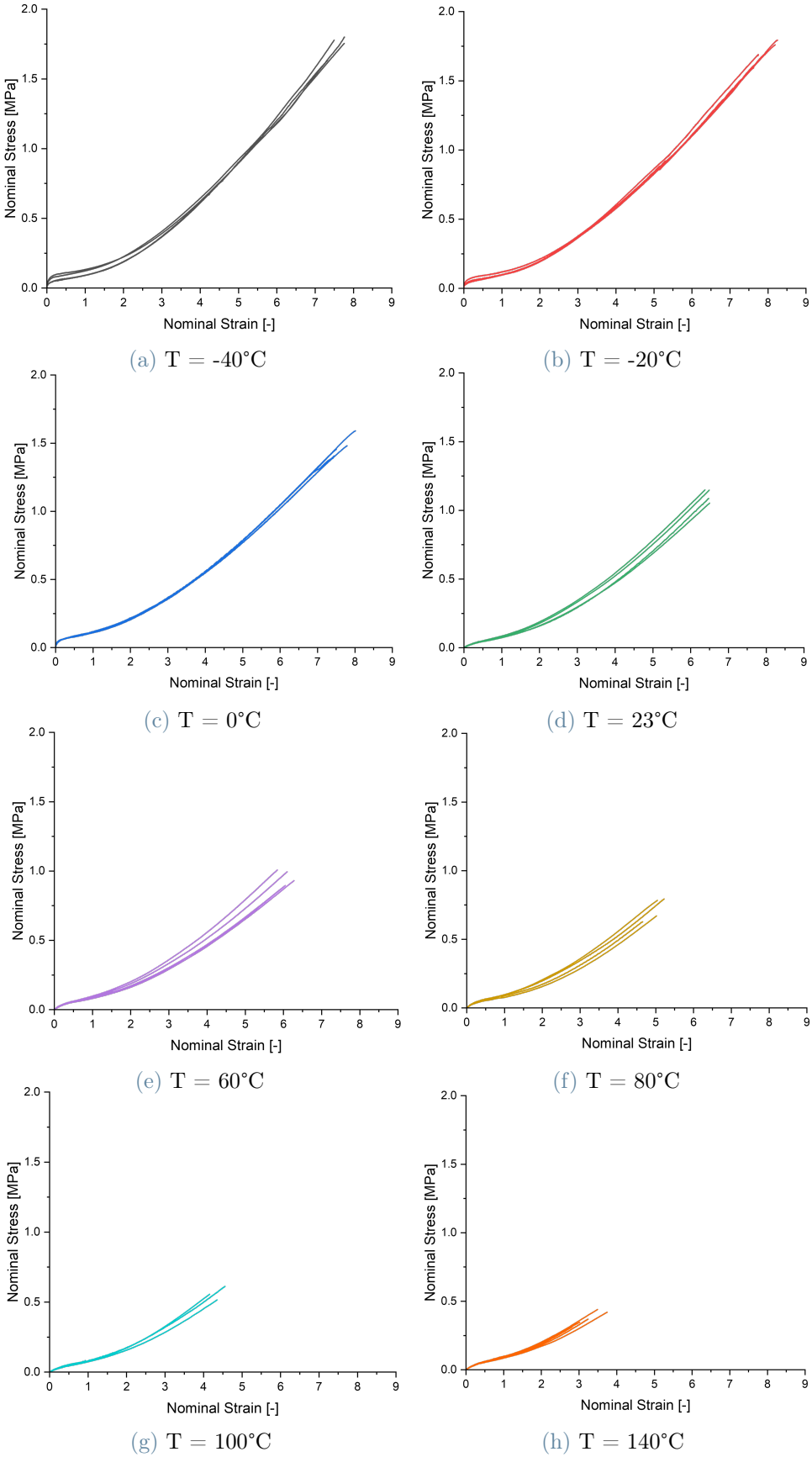

(a) T = -40°C (b) T = -20°C

(c) T = 0°C (d) T = 23°C

(e) T = 60°C (f) T = 80°C

(g) T = 100°C (h) T = 140°C

Figure 4.39: Nominal stress-strain curves obtained from tests performed at $\dot{\epsilon} = 0.1\ s^{-1}$ and different temperatures.

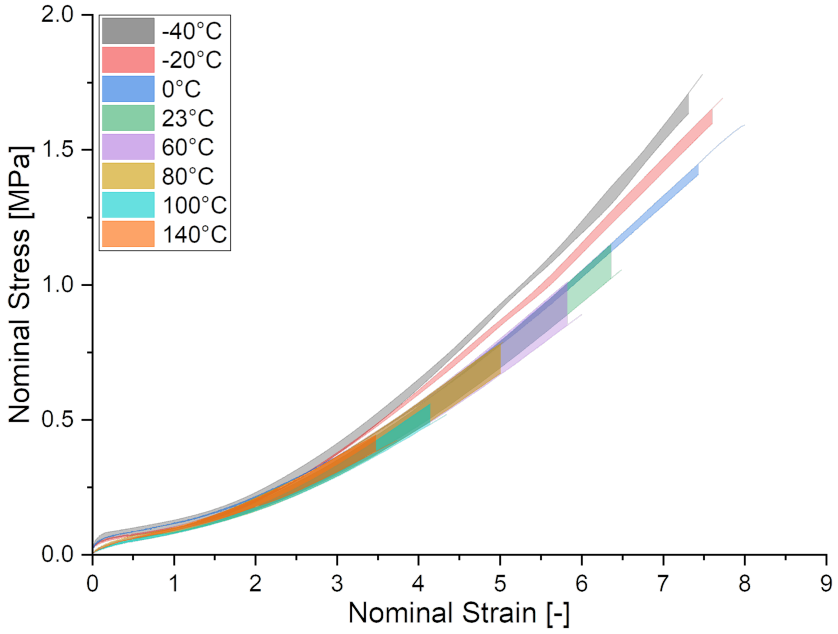

Figure 4.40: Nominal stress-strain curves for different testing temperatures. All tests performed at $\dot{\epsilon} = 0.1\ s^{-1}$.

The first thing that should be noted, is that the material response variability for temperature higher than or equal to 23°C (which will be referred to as "high temperature range") is larger that its variability at temperatures lower than 23°C (which will be referred to as "low temperature range").

In general, given the curves dispersion, no visible variation in the material response in the strain range explored is observed for test performed in the high temperature range. The main effect of increasing temperature, is a decrease in the material stress and strain at failure, which will be discussed in the following sections. On the contrary, at low temperatures the material shows a higher stiffness at low strains and higher stress at high strains.

In [59], it is highlighted how, for unfilled silicone elastomers, the stiffness in the low-strain region, as expected, increase as the temperature increases: this trend was not observed for Ecoflex 00-50, supporting the idea that the material contains a reinforcing filler. In fact, the filler precence related contribution to the material stiffness, associated with an enthalpy-related response, becomes more significant at low temperatures where the elastomer contribution, associated with an entropy-related response, decreases; the overall filler-elastomer system mobility is therefore reduced in the low temperature range, resulting in a stiffer response upon stretching the material [40].

Overall, the effect of temperature on the material response is complex and an accurate

description through a model is outside the objectives of this thesis work. On the other hand, the ultimate properties show a clear dependence on temperature, which is presented and discussed in detail in the following section.

4.3.2. Ultimate Stress and Strain

In order to analyse Ecoflex 00-50 ultimate tensile properties data dependence on temperature, the concept of **failure envelope** is introduced, originally proposed in [60, 61] for unfilled elastomers.

The failure envelope has been introduced in order to determine a functional relation between ultimate stress (σ_U) and strain (ϵ_U), and the failure time (t_U). In particular, it was found that for each σ_U value exists a unique ϵ_U value, independent of testing method and conditions [60].

A description of this approach will be briefly reported here: considering a sample subjected to a constant load test (creep tests), the material will undergo a progressively increasing macroscopic elongation, while, at a microscopic level, small tears will form and start to grow; at the tip of these increasing in size tears, the material behaves like strained elastomer filaments do: at a certain time they break. The time taken for the material at the tear tip to rupture is determined by the rate of retraction of the broken filament and the creep response of the subsequent filament to the load to which it is subjected. Therefore, the tear propagation rate, that controls the time to failure t_U, is determined by the creep response of the elastomer [62]. Assuming that the macroscopic failure occurs after q filaments have ruptured, the time required for each filament to break is t_U/q.

The creep response is quantitatively determined from the creep compliance, which is defined as:

$$\Gamma(t) = \frac{\epsilon(t)}{\sigma_0} \tag{4.30}$$

where σ_0 is the constant load applied during the creep test, which also corresponds to σ_U in this testing condition. At the microscopic level, the ultimate stress of a single filament (σ_B) is:

$$\sigma_B = \frac{\epsilon_B}{\Gamma(t_U/q)} \tag{4.31}$$

where ϵ_B is the ultimate strain of the single filament and $\Gamma(t_U/q)$ is the material creep

compliance evaluated at the time required for a single filament to rupture. It should be noted that $\Gamma(t)$ is the material creep compliance, a macroscopic quantity, which can be used to describe the single filament behaviour by introducing the factor q, substantially reducing the time scale of the response [62]. The material and filament stress at break are related via a stress intensification factor s, which takes into account the critical conditions at the tear tip:

$$\sigma_B = \sigma_U s \tag{4.32}$$

Combining Eq. (4.31) and Eq. (4.32), one obtains:

$$\sigma_U = \frac{\sigma_B}{s} = \frac{\epsilon_B/s}{\Gamma(t_U/q)} = \frac{K}{\Gamma(t_U/q)} \tag{4.33}$$

where K is a constant related to the critical rupture conditions at the tear tip [63]. The ultimate material strain can be obtained by combining Eq. (4.30) and Eq. (4.33), as:

$$\Gamma(t_U) = \frac{\epsilon_U}{\sigma_U} = \frac{\epsilon_U}{K}\Gamma(t_U/q) \tag{4.34}$$

$$\epsilon_U = K\left[\frac{\Gamma(t_U)}{\Gamma(t_U/q)}\right] \tag{4.35}$$

Eqs. (4.33) and (4.35) can be expressed in in logarithmic form as:

$$\begin{cases} log(\sigma_U) = log(K) - log(\Gamma(t_U/q)) \\ log(\epsilon_U) = log(K) + log(\Gamma(t_U)) - log(\Gamma(t_U/q)) \end{cases} \tag{4.36}$$

By representing the ultimate stress and strain on a double logarithmic plot, the curve interpolating the rupture points, obtained in different testing conditions, identifies the failure envelope of the material, as shown in Figure 4.41, for an unfilled SBR rubber [60]. Generally speaking, the failure envelope is unique for any material, and is independent of time and temperature. The ultimate stress values are multiplied by a temperature factor which corresponds to the testing temperature in Kelvin, in order to reduce all values to the arbitrary reference temperature T_0, analogously to the procedure used to perform time-temperature superposition of small-deformation viscoelastic data, where the relaxation and dynamic moduli are usually multiplied by a temperature factor before shifting data along the frequency axis to effect superposition, although no direct experimental evidence

was presented to justify the procedure for ultimate stress superposition [60].

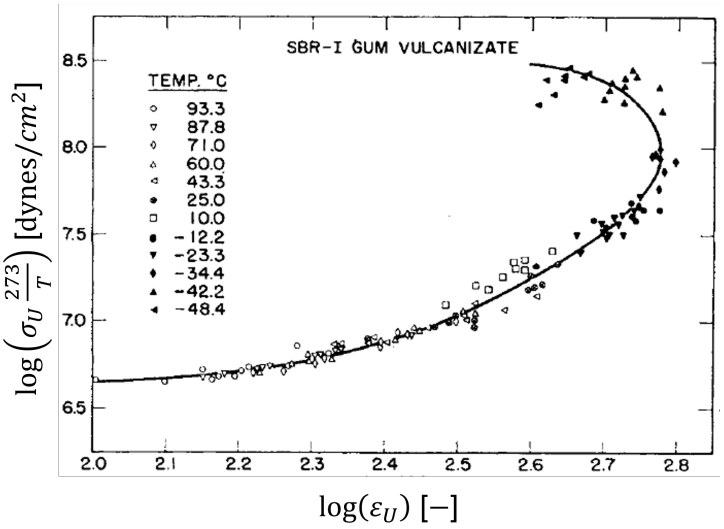

Figure 4.41: $log(\sigma_U T_0/T)$ vs $log(\epsilon_U)$ representation of ultimate tensile data for an unfilled SBR rubber [61].

Therefore, the failure behaviour of an elastomer is determined by its microscopic behaviour, where the tear propagation is governed by the creep compliance of the filament, which is independent of the testing method and conditions [62]: since $\Gamma(t)$ is an increasing function of both time and temperature, it is clear to see that σ_U will decrease with increasing temperature or decreasing strain rate. On the other hand, ϵ_U is determined by the ratio $\Gamma(t_U)/\Gamma(t_U/q)$, resulting in a non-linear trend:

- For very low temperatures (or large strain rates) the ratio is close to unity, since both contributions have values characteristic of the glassy state of the creep compliance;
- For slightly higher temperatures, $\Gamma(t_U)$ is in the rubbery portion of the creep curve, whereas $\Gamma(t_U/q)$ is still in the glassy region of the response, determining large ultimate strains;
- For very high temperatures, both contributions are in the rubbery region of the creep curve, resulting in lower ϵ_U values.

Therefore, to determine the theoretical values of ultimate stress and strains the knowledge of the constants K and q is required.

As already noticed in previous section of this thesis work, an increase of ultimate stress and strain of Ecoflex 00-50 has been observed with increasing strain rate and decreasing

temperature. Focusing on the temperature effect, the rupture points obtained at different temperatures are reported in Figure 4.42 in a log-log scale plot.

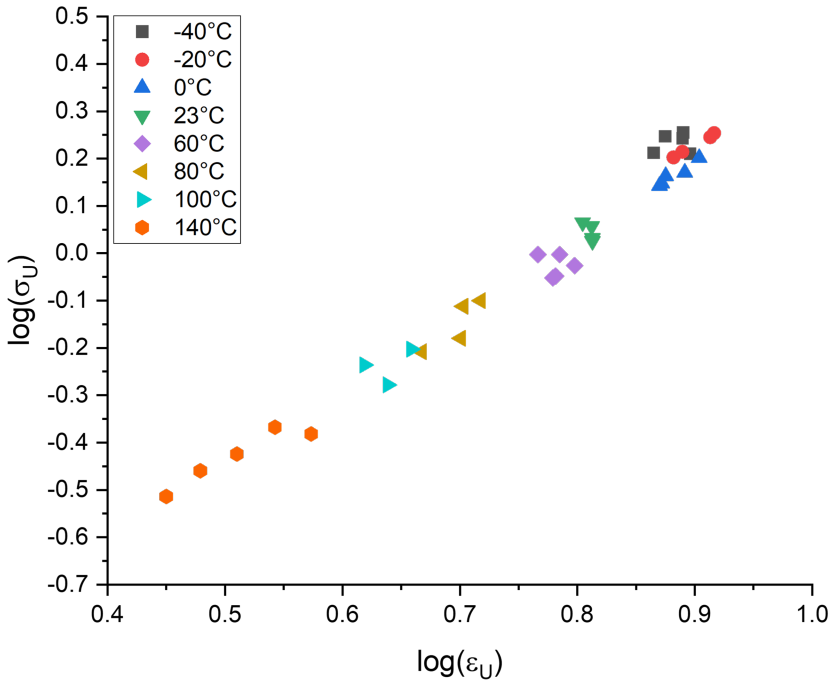

Figure 4.42: $log(\sigma_U)$ vs $log(\epsilon_U)$ representation of ultimate tensile data, obtained for Ecoflex 00-50 at different temperatures and $\dot{\epsilon} = 0.1\ s^{-1}$.

Some scattering of experimental data exists, especially for the values obtained at -140°C, but it is evident how the points define a clear curve, which identifies the failure envelope of Ecoflex 00-50. Two separate regimes can be identified in the curve: the high temperature region (corresponding to $T \geq 23$°C) where a linear trend of the envelope is observed with increasing temperature, and a low temperature regime (corresponding to $T < 23$°C) where a change of trend is observed, since ϵ_U remains almost constant, whereas σ_U slightly increases with decreasing temperature. These last observations are in agreement with those reported in [60, 61] for various unfilled elastomers; the decrease of the strain at failure observed in Figure 4.41 for low temperatures was not observed for Ecoflex 00-50, most likely because no crystallization occurs in the temperature range considered (since T_c = -78.5°C, as already reported in Section 3.1.2).

As already mentioned, in [60] it is proposed to multiply ultimate stress values by a T_0/T factor, in order to reduce all values to the reference temperature, although no direct experimental evidence was presented to justify the procedure. In order to compare the the trends with and without the presence of the reducing factor, in Figure 4.43 the ultimate stress values are multiplied by T_0/T, where T_0 is chosen to be 296 K.

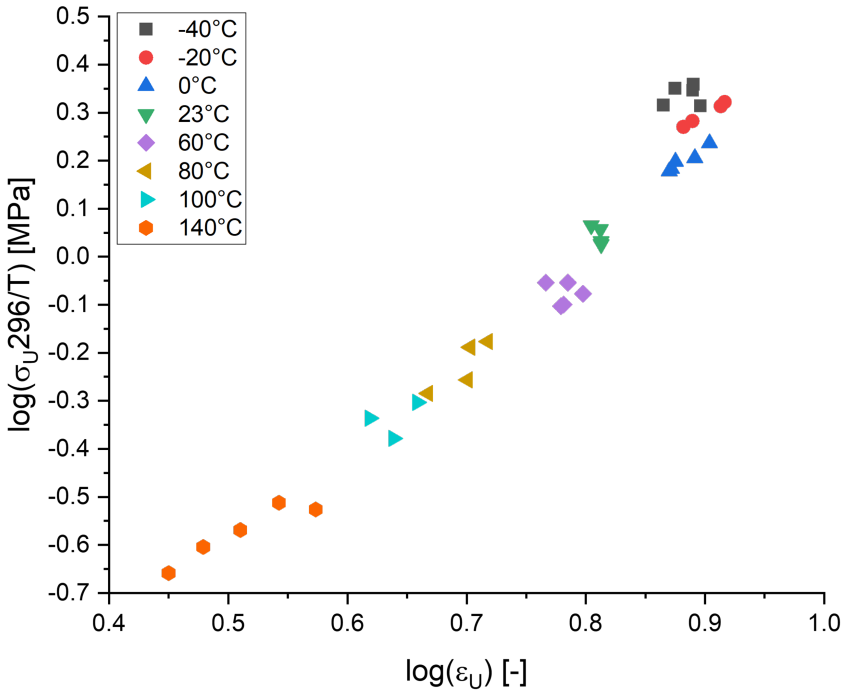

Figure 4.43: $log(\sigma_U T_0/T)$ vs $log(\epsilon_U)$ representation of ultimate tensile data, obtained for Ecoflex 00-50 at different temperatures and $\dot{\epsilon} = 0.1\ s^{-1}$.

No major differences are observed between Figure 4.42 and Figure 4.43 although in the latter, as expected, the slope of the high-temperature linear region is increased, since the factor T_0/T decreases with increasing temperature; for the same reason, the rupture points obtained at temperatures below 23°C are more spaced in Figure 4.43. Therefore, it was decided to adopt the temperature factor T_0/T in the following representations of experimental results, in order to follow the formalism used in [60, 61].

An alternative representation of stress and strain at failure is reported in [60]: from the values of stress and strain, it is possible to define a linear relation between the two, according to Martin, Roth and Stiehler (MRS) equation [64]:

$$\sigma = E_e \left(\frac{\lambda - 1}{\lambda^2} \right) exp \left[A \left(\lambda - \frac{1}{\lambda} \right) \right] \tag{4.37}$$

where E_e is the equilibrium tensile modulus of the material and A is an empirical constant. This relationship can be applied to high temperature ultimate stress and strain, since the stress-strain curves obtained from tests in the high temperature range correspond to the equilibrium response of the material, showing a trend not dependent on testing temperature [61]. To reduce data obtained at different temperatures to a single reference temperature, the same multiplying factor used in the failure envelope representation is

employed. Thus, the logarithmic form for ultimate tensile data of Eq. (4.37) becomes:

$$log\left[\frac{\sigma_U \lambda_U^2}{(\lambda_U - 1)}\frac{296}{T}\right] = log\left(E_e \frac{296}{T}\right) + 2.303A\left(\lambda_U - \frac{1}{\lambda_U}\right) \tag{4.38}$$

which corresponds to a linear relation with slope $2.303A$ and intercept $log\,(E_e 296/T)$, as shown in Figure 4.44.

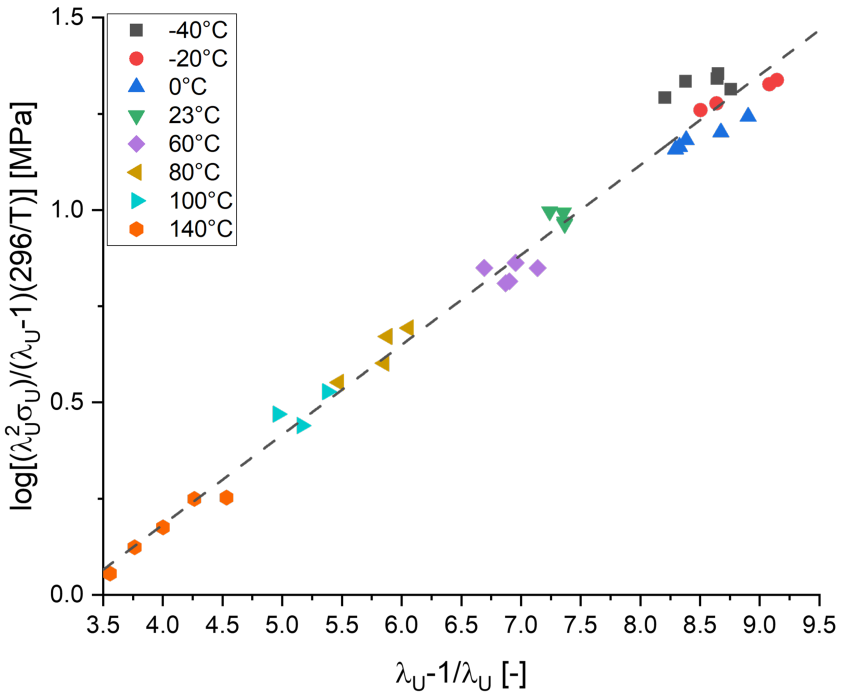

Figure 4.44: MRS representation of ultimate tensile data, obtained at different temperatures and theoretical linear trend (dashed line).

It can be seen how the ultimate data obtained in the temperature range between 23°C and 140°C fall perfectly on the theoretical line, whereas the data measured in the low temperature range (below 23°C) show a very limited degree of deviation from the predicted behaviour. This is in agreement with the results reported in [61] for various unfilled elastomers, where it is observed that only the high temperature ultimate stress and strain identify the equilibrium behaviour of the material and low temperature data do not fall on the linear trend. Furthermore, from the intercept of the linear trend it is found that $E_e = 0.17$ MPa and from the slope $A = 0.1$ MPa; the value of modulus obtained is nearly twice the value obtained in Section 4.1.1, from fitting of the linear elastic region of the material response in UT deformation state (at room temperature), most likely because the different specimen geometry used for temperature testing causes a stiffer response at

small strains (for a comparison, the apparent modulus obtained from linear fitting of PS data up to $\epsilon = 0.1$ is equal to $E_{PS} = 0.2$ MPa).

Further tests were performed at 23°C, 60°C and 100°C at different strain rates, namely 0.1 s^{-1}, 0.01 s^{-1} and 0.001 s^{-1}. The stress at failure (σ_U) and the time to failure (t_U) were measured for each test condition. In Figure 4.45 these data have been reported in a log-log scale, for a reference temperature of 23°C.

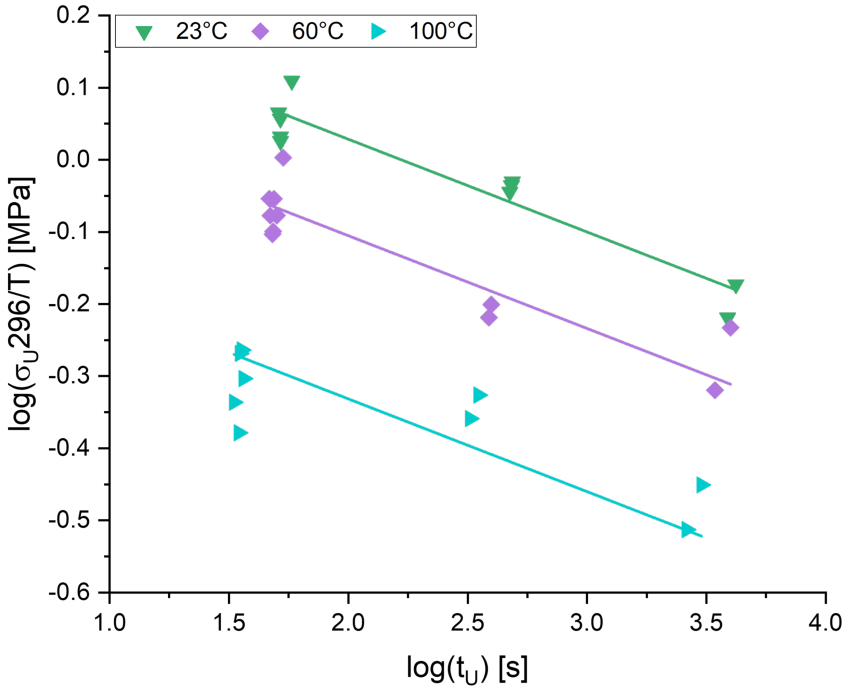

Figure 4.45: $log(\sigma_U T_0/T)$ vs $log(t_U)$ representation of ultimate tensile stress data, obtained at different temperatures and different strain rates, fitted with Eq. (4.39) and $m = -0.129$ MPa/s.

The data obtained varying the strain rate at a fixed temperature, were fitted through a power-law equation [65], in the logarithmic form:

$$log(\sigma_U T_0/T) = m \times log(t_U) + n \tag{4.39}$$

where m and n are the two power-law coefficients. In particular, a constant value of m was used for the different temperatures data fitting. This m value was obtained from the fitting of the ultimate stress data at 23°C and resulted to be equal to -0.129 MPa/s. The shifting required to superpose data at temperature T with those at the reference temperature T_0 = 23°C identifies the logarithm of the shift factor $log(a_T^{T_0})$. Through

horizontal shifting of the different temperatures ultimate stress data, a master curve has been obtained as shown in Figure 4.46; the values of shift factor obtained are reported in Table 4.11 that, referring to Eq. (4.39) is equal to:

$$log(a_T^{T_0}) = \frac{n_T - n_{T_0}}{m} \tag{4.40}$$

Table 4.11: Shift factor values obtained from Eq. (4.40).

Temperature, [°C]	n_T, **[MPa]**	$log(a_T^{T_0})$, **[-]**
23	0.286	0
60	0.152	1.04
100	-0.074	2.80

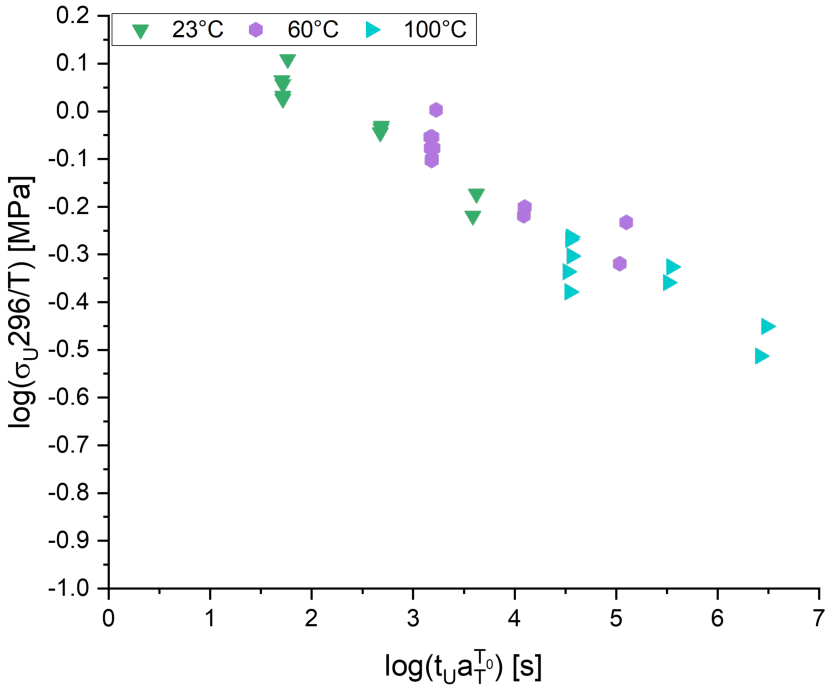

Figure 4.46: $log(\sigma_U T_0/T)$ vs $log(t_U a_T^{T_0})$ master curve representation of ultimate tensile stress data, obtained at different temperatures and different strain rates.

The master curve obtained can be used to compute the theoretical values of ultimate stress and strain, defining the theoretical failure envelope of the material, as originally proposed in [63, 62]. As previously explained, and illustrated in Eq. (4.36), the creep compliance of the material is required to compute the values of stress and strain at failure: experimentally, the creep compliance curve was obtained by performing a creep

test at room temperature, on the same specimen type used for temperature tensile tests (illustrated in Section 3.2.4), with an applied constant load corresponding to $\sigma_0 = \sigma_U = 0.48$ MPa.

As suggested in [63], the experimental values of the two parameters can be obtained by representing $-log(\Gamma(t))$ and the ultimate tensile stress master curve on a common plot, as a function of $log(t)$ as shown in Figure 4.47: the vertical and horizontal shifts, needed to superimpose the two curves, correspond to $log(K)$ and $log(q)$, respectively.

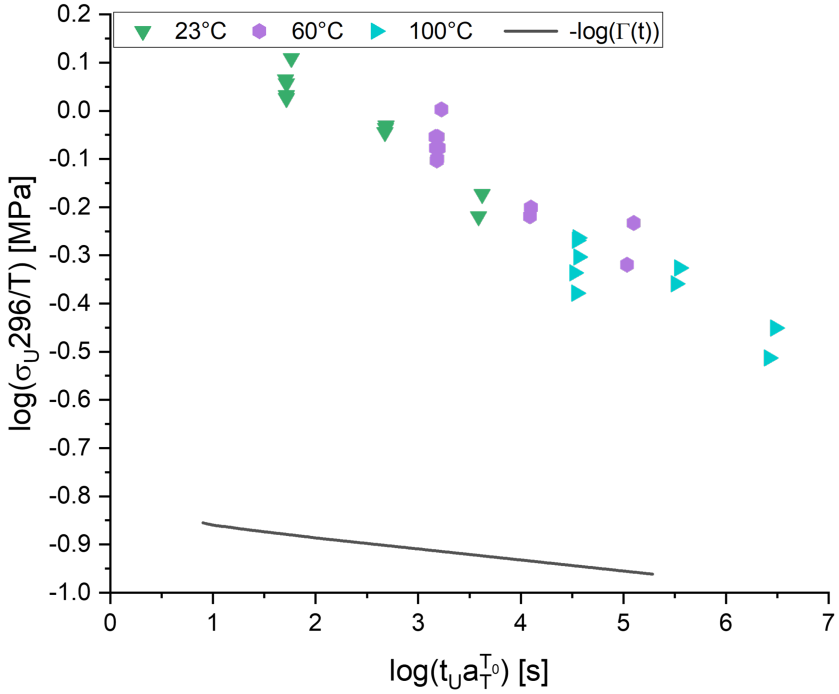

Figure 4.47: $log(\sigma_U T_0/T)$ and $-log(\Gamma(t))$ vs $log(t_U a_T^{T_0})$ representation of ultimate tensile stress data and creep compliance.

It is evident how, with the experimental data obtained, it is impossible to superimpose the creep compliance curve to the ultimate stress master curve, since they are never parallel in the range examined. As a matter of fact, the slope of the master curve is $m_m = -0.129$ MPa/s, whereas the slope of the creep compliance curve is $m_c = -0.023$ MPa/s. Therefore, it was concluded that, given the obtained experimental results, the determination of the theoretical failure envelope was not feasible. In the future, further creep tests at different load levels and different temperatures should be performed in order to obtain a prediction of the failure envelope of the material.

As a conclusion to this section, the ultimate tensile data obtained at different temperatures and strain rates are presented on the same failure envelope plot in Figure 4.48 and MRS

plot in Figure 4.49, in order to show how all data points collapse on a single curve in both cases as already shown in [60, 61], thus confirming the suitability of this two methods to predict the failure of Ecoflex 00-50. The theoretical linear trend of the MRS plot is the same reported in Figure 4.44.

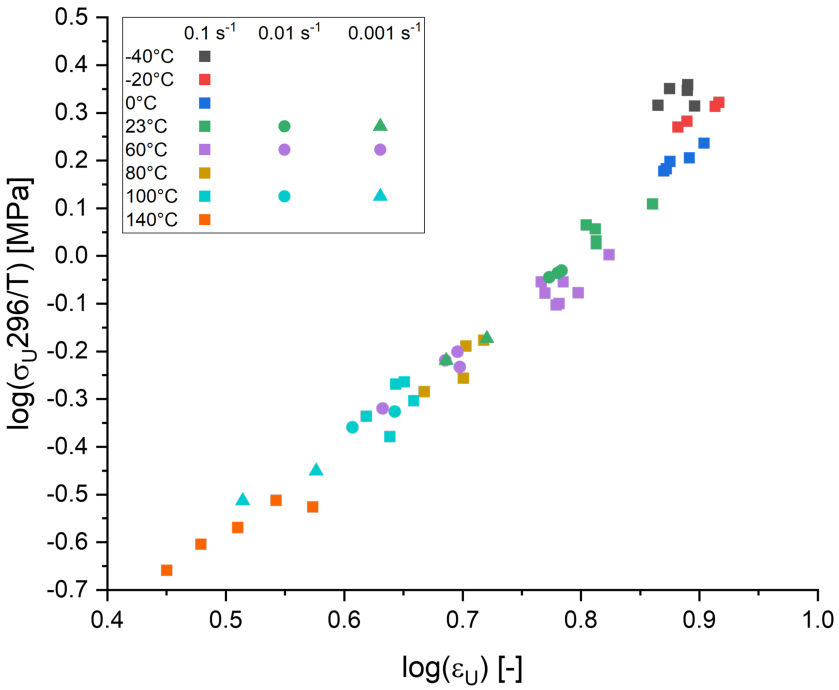

Figure 4.48: Failure envelope representation of ultimate tensile data obtained at different temperatures and strain rates.

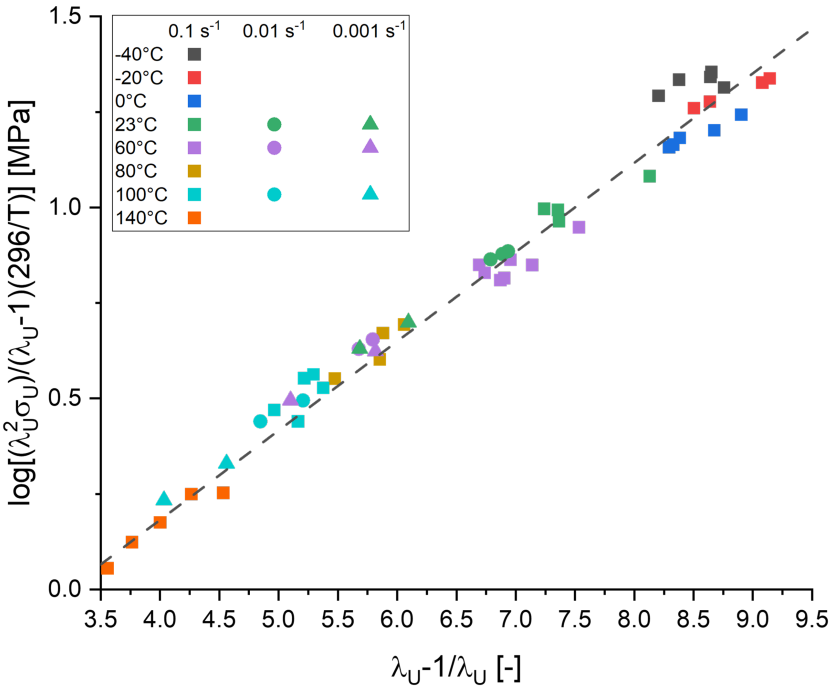

Figure 4.49: MRS representation of ultimate tensile data obtained at different temperatures and strain rates, and theoretical linear trend (dashed line).

5 | Conclusive Remarks and Future Developments

In this work, the mechanical behaviour of Ecoflex 00-50 has been characterized in different deformation states, namely uniaxial tension, pure shear and biaxial tension; furthermore, the effects of strain rate and temperature on the mechanical response were investigated.

The main activities and experimental results of this research can be summarized as follows:

- The material behaviour in monotonic loading conditions has been characterized, highlighting that for strain levels between 0 and 1 in uniaxial tension and pure shear, and between 0 and 0.3 in biaxial tension, the material response is practically unaffected by the strain rate. Outside of these ranges, instead, in all three deformation states for a given strain the stress increases with the increase of the applied strain rate. As a consequence, ultimate stress and strain values increase with the applied strain rate.
- The material behaviour in cyclic loading revealed that the the material has a hysteretical behaviour, the material undergoes strain induced softening (or Mullins effect) and the presence of a residual deformation; the magnitude of these phenomena depends on the applied strain level. Furthermore, the hysteretical dissipation and the magnitutde of the strain induced softening progressively decrease in the loading-unloading cycles following the first one, whereas no significant increase in the residual deformation was observed in the following cycles. In particular, it was found that, for applied strain values up to 1, the material showed negligible energy dissipation when tested under uniaxial tension and in pure shear loading conditions while non-negligible energy dissipation occurred in biaxial tension.
- The experimental data obtained from the monotonic and cyclic tensile tests were used to verify the applicability of a constitutive model proposed in [42] for other Ecoflex Materials, to the grade under study. Thanks to a combination of the Neo-Hookean and Yeoh hyperelastic models, a good agreement was found between the considered constitutive equation and the real response of the material during the

loading phase, up to a strain of 4 in uniaxial tension and pure shear and up to failure in biaxial tension. On the other hand, the considered Ogden-Roxburgh pseudo-elastic model was unable to predict the unloading response of the material, because the residual strain was not accounted for in its formulation.

- The effect of temperature on the material response, and in particular on stress and strain at failure, were considered in the range between -40°C and 140°C. The overall stress-strain trend is not affected by the temperature in the temperature range above 23°C, nevertheless a decrease of ultimate material properties with increasing temperature was observed and for temperatures below room temperature an increase in stiffness in the low strain region was observed, as well as an increase of the stress in the high strain region. A method to predict failure at different temperatures and strain rates, based on the failure envelope concept and on the Martin-Roth-Stiehler (MRS) equation, originally developed in [60], was proposed: the results showed that ultimate stress and strain values would follow a clear trend in both representations. The theoretical failure envelope was not obtained in this work, whereas the MRS linear description constitutes a valuable engineering tool, since it allows an effective description of the combined effects of strain rate and temperature on the stress and strain at failure of Ecoflex 00-50.

In the future, a more complete constitutive model should be developed, since the proposed Neo-Hookean and Yeoh model does not encompass the observed time and temperature dependence of Ecoflex 00-50 mechanical response, thus failing to describe the viscoelastic behaviour of the material, and the Ogden-Roxburgh pseudo-elastic model does not predict any residual strain at the end of the unloading ramp. Furthermore, the model assumes incompressibility of the material, whereas some of the results obtained in this work suggest the presence of filler in the material under study. Therefore, a more complete chemical and physical characterization of the material is required to clarify this point and to be able to correlate the macroscopic response to the microscopic structure, in order to develop a physically-based constitutive model, which is not purely phenomenological as the adopted one.

Finally, considering the data obtained in this work, the ultimate stress and strain of Ecoflex 00-50 can be described with the MRS equation between -40°C and 140°C, although the ultimate properties values obtained at temperatures lower than 23°C showed slight deviations from the linear trend. The validity of the MRS equation should be verified in the future in a broader temperature range, and in particular at temperatures lower than -40°C, at which crystallization phenomena are expected to occur. Furthermore, a in-depth characterization of the creep response of Ecoflex 00-50 should be performed to

find the parameters defining the theoretical failure envelope and to validate it, since it could be a possible approach to predict the material ultimate properties outside of the temperature range investigated in this work.

A | Mould Schematics

The male-female moulds used to cast biaxial and pure shear specimen were designed as part of this thesis work and are presented in this Appendix. All dimensions were obtained from already available moulds used for compression moulding. 3D models were sketched in Solidworks software and the final moulds were realized in aluminium.

The following schematics refer to (in order of appearance):

1. Male Pure Shear Mould.
2. Female Pure Shear Mould.
3. Male Biaxial Mould.
4. Female Biaxial Mould.

All views are in 1:3 scale, except where otherwise indicated. All dimensions are in millimeters.

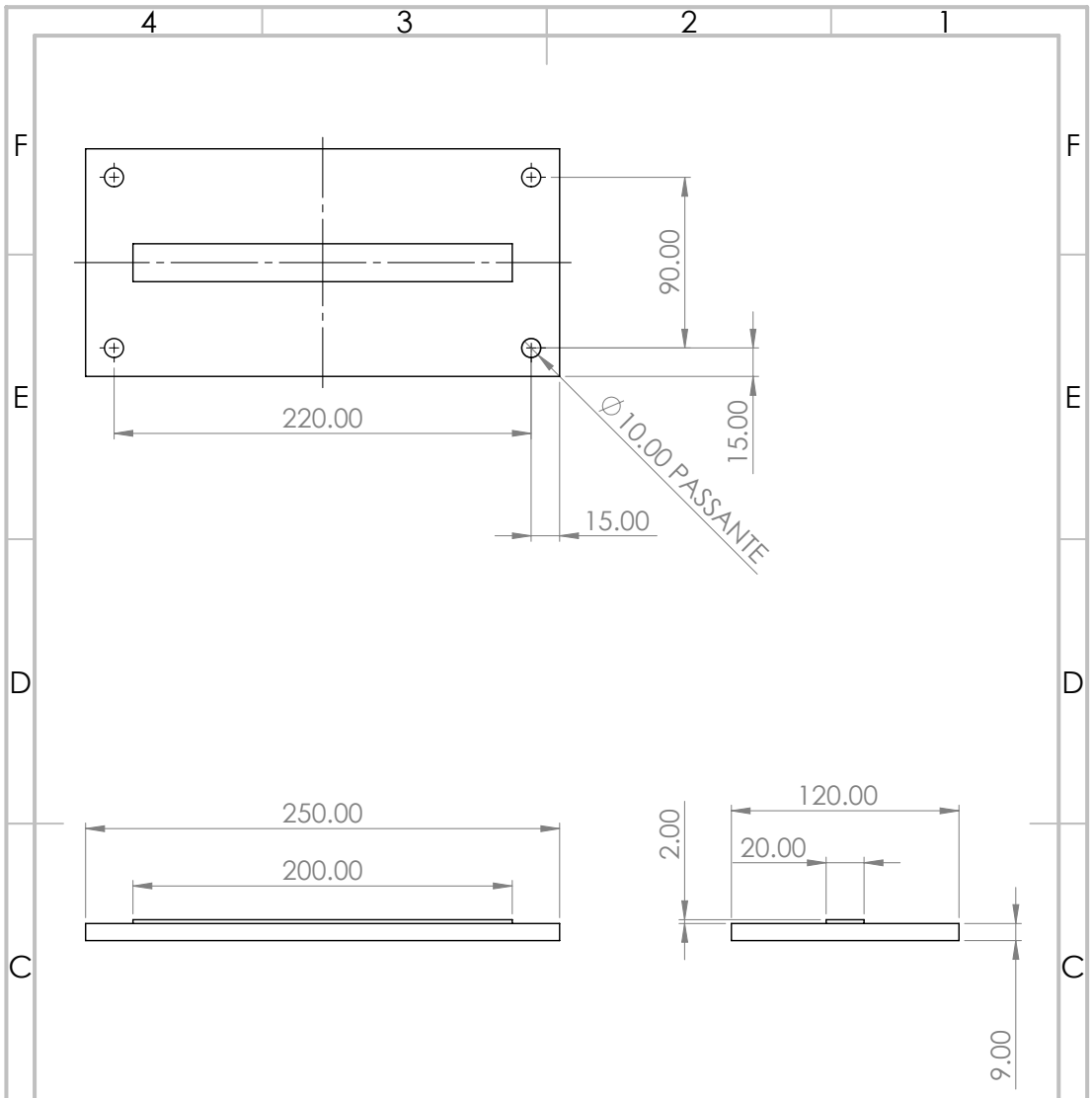

SE NON SPECIFICATO: QUOTE IN MILLIMETRI FINITURA SUPERFICIE: TOLLERANZE: LINEARE: ANGOLARE:		FINITURA:			INTERRUZIONE BORDI NETTI		NON SCALARE DISEGNO	REVISIONE
	NOME	FIRMA	DATA				TITOLO:	
DISEG.	Lavazza						PS Mould - Male	
VERIF.								
APPR.								
FABB.								
Qual.				MATERIALE:			N. DISEGNO	A4
				Al				
				PESO:			SCALA: 1:3	FOGLIO 1 DI 1

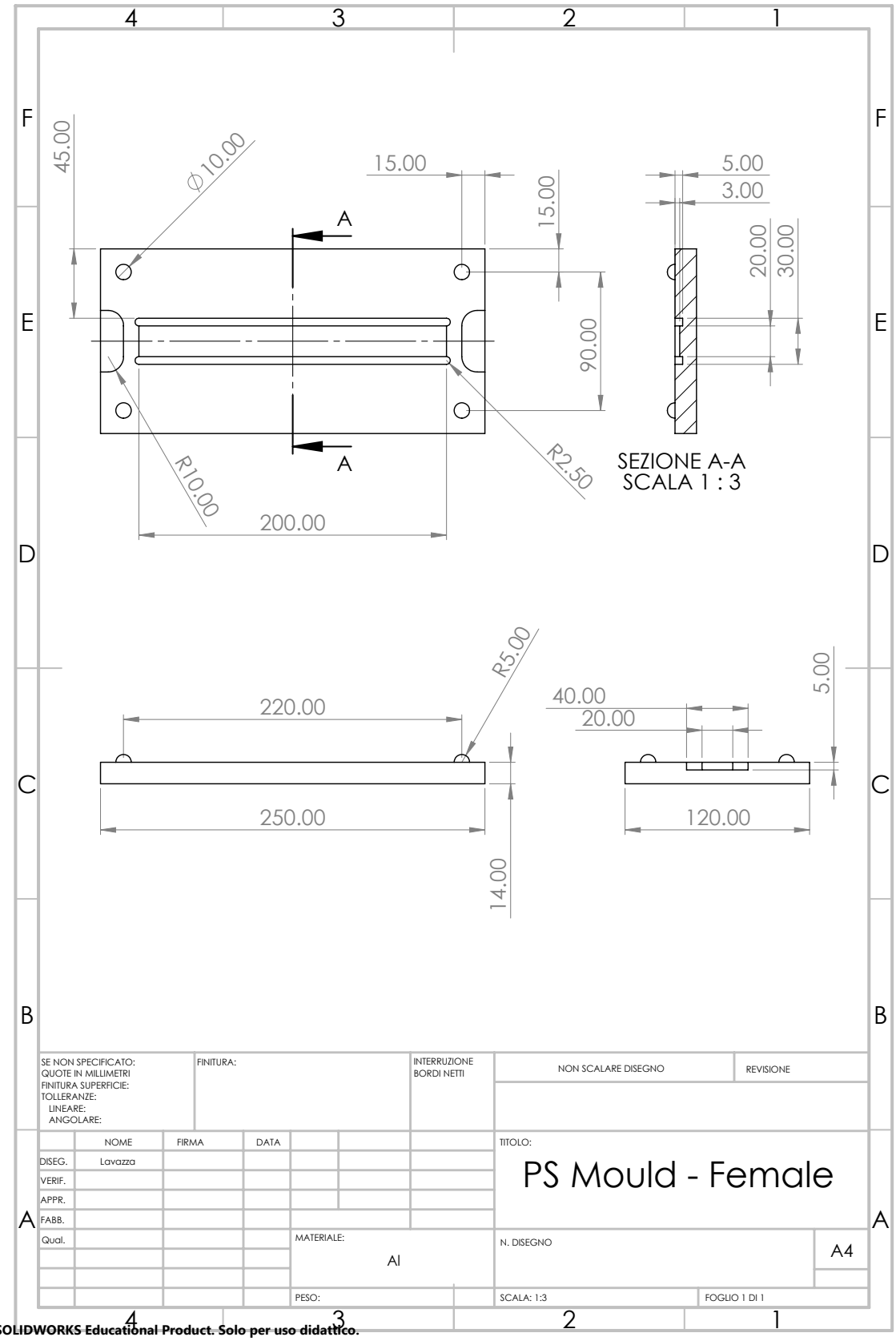

SE NON SPECIFICATO: QUOTE IN MILLIMETRI FINITURA SUPERFICIE: TOLLERANZE: LINEARE: ANGOLARE:		FINITURA:		INTERRUZIONE BORDI NETTI		NON SCALARE DISEGNO	REVISIONE	
	NOME	FIRMA	DATA				TITOLO:	
DISEG.	Lavazza						PS Mould - Female	
VERIF.								
APPR.								
FABB.								
Qual.				MATERIALE:			N. DISEGNO	A4
				Al				
				PESO:			SCALA: 1:3	FOGLIO 1 DI 1

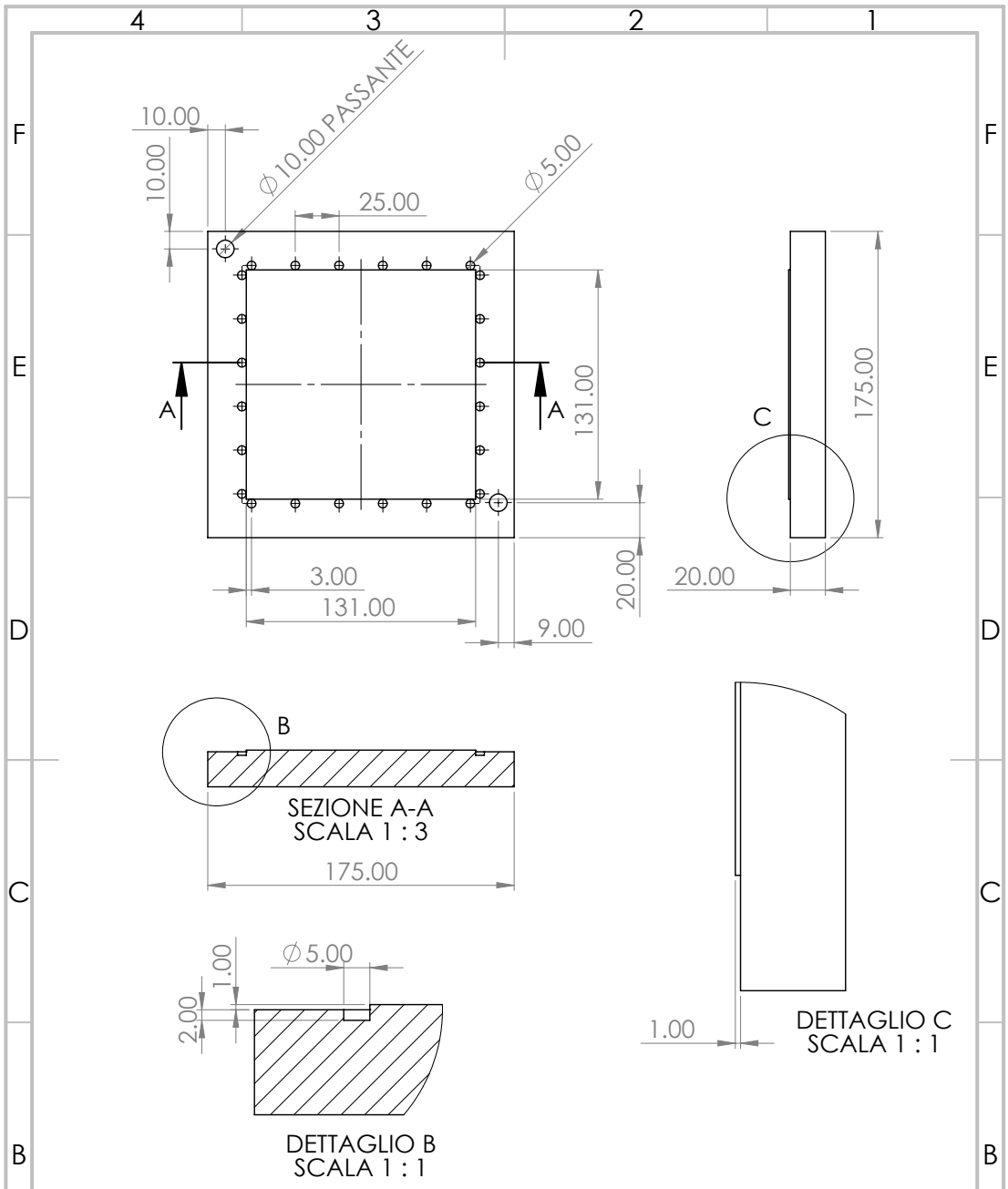

SE NON SPECIFICATO: QUOTE IN MILLIMETRI FINITURA SUPERFICIE: TOLLERANZE: LINEARE: ANGOLARE:	FINITURA:		INTERRUZIONE BORDI NETTI	NON SCALARE DISEGNO	REVISIONE		
	NOME	FIRMA	DATA	TITOLO:			
DISEG.	Lavazza			Biaxial Mould - Male			
VERIF.							
APPR.							
FABB.							
Qual.				MATERIALE:	N. DISEGNO		A4
				Al			
				PESO:	SCALA 1:3	FOGLIO 1 DI 1	

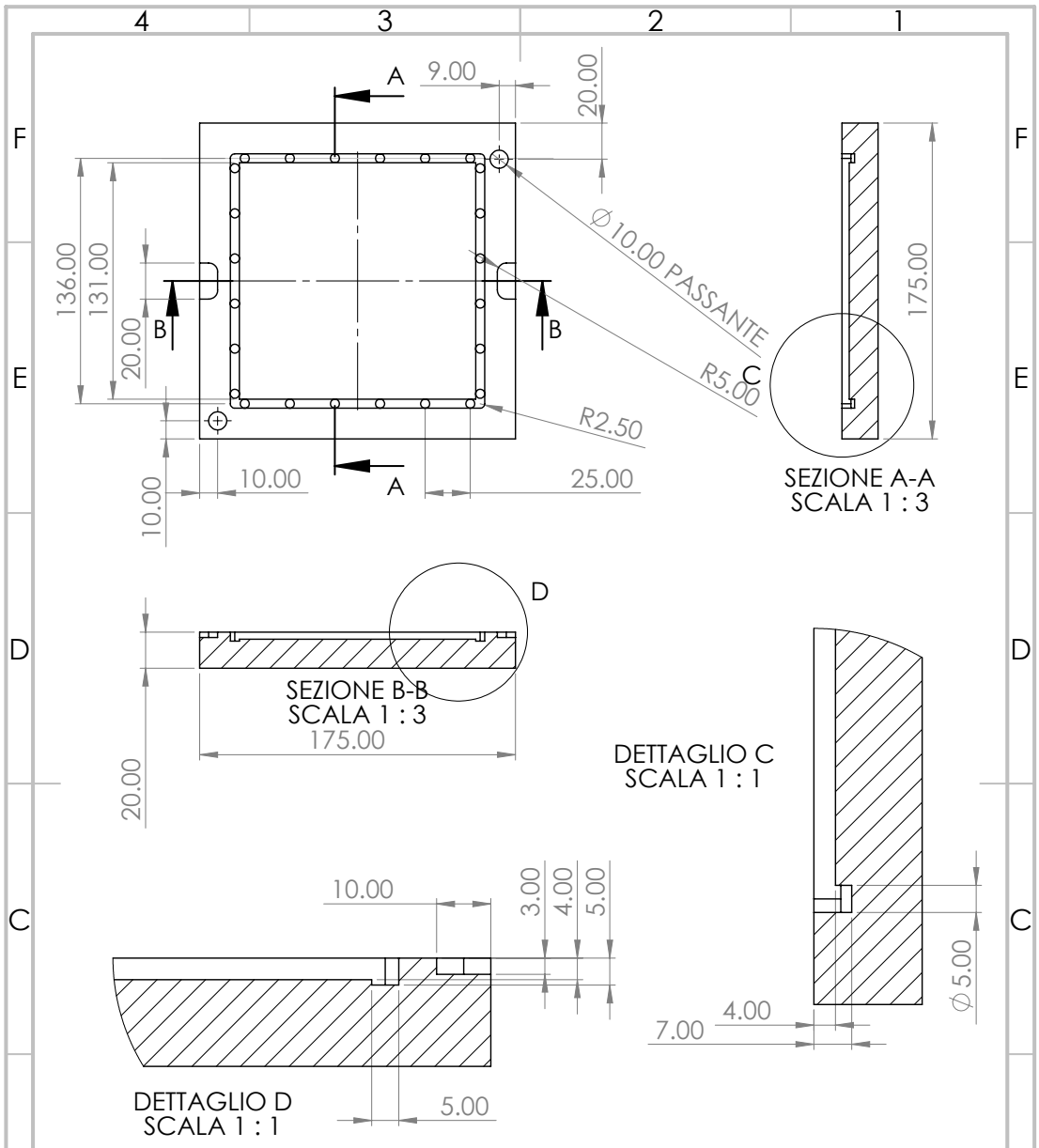

SE NON SPECIFICATO: QUOTE IN MILLIMETRI FINITURA SUPERFICIE: TOLLERANZE: LINEARE: ANGOLARE:		FINITURA:		INTERRUZIONE BORDI NETTI	NON SCALARE DISEGNO		REVISIONE
	NOME	FIRMA	DATA				TITOLO:
DISEG.	Lavazza						Biaxial Mould - Female
VERIF.							
APPR.							
FABB.							
Qual.				MATERIALE:	N. DISEGNO		A4
				Al			
				PESO:	SCALA: 1:3	FOGLIO 1 DI 1	

Bibliography

[1] L. R. G. Treloar. *The Physics of Rubber Elasticity, 3rd ed.* Oxford University Press, Oxford, 2009.

[2] J. E. Mark, B. Erman, and F. R. Eirich. *Science and Technology of Rubber*. Elsevier Academic Press, 2005.

[3] S. J. Clarson. Silicones and silicone-modified materials: A concise overview. *ACS Symposium Series*, pages 1–10, 2003.

[4] A. M. Stricher, R. G. Rinaldi, C. Barrès, F. Ganachaud, and L. Chazeau. How i met your elastomers: from network topology to mechanical behaviours of conventional silicone materials. *RSC Advances*, 5(66):53713–53725, 2015.

[5] Z. Liao, M. Hossain, X. Yao, R. Navaratne, and G. Chagnon. A comprehensive thermo-viscoelastic experimental investigation of ecoflex polymer. *Polymer Testing*, 86:106478, 2020.

[6] Z. Liao and M. Hossain. An additively manufactured silicone polymer: Thermo-viscoelastic experimental study and computational modelling. *Additive Manufacturing*, 35:101395, 2020.

[7] E. Luis, H. M. Pan, A. K. Bastola, R. Bajpai, S. L. Sing, J. Song, and W. Y. Yeong. 3d printed silicone meniscus implants: Influence of the 3d printing process on properties of silicone implants. *Polymers*, 138(9):2136, 2020.

[8] P. Mazurek, S. Vudayagiri, and A. L. Skov. How to tailor flexible silicone elastomers with mechanical integrity: a tutorial review. *Chemical Society Reviews*, 48(6):1448–1464, 2019.

[9] E. L. Warrick, O. R. Pierce, K. E. Polmanteer, and J. C. Saam. Silicone elastomer developments 1967–1977. *Rubber Chemistry and Technology*, 52(3):437–525, 1979.

[10] L. Bokobza. Elastomeric composites. i. silicone composites. *Journal of Applied Polymer Science*, 93(5):2095–2104, 2004.

[11] A. N. Gent. *Engineering with Rubber, 3rd ed.* Hanser Publications, 2012.

[12] L. Chevalier and Y. Marco. Tools for multiaxial validation of behavior laws chosen for modeling hyper-elasticity of rubber-like materials. *Journal of Polymer Engineering and Science*, 42(2):280–298, 2002.

[13] S. R. E. Turri. *Principles of Polymer Chemistry Course Lecture Notes.* Politecnico di Milano, 2020.

[14] R. W. Ogden. *Non-linear elastic deformations.* Dover Publications, 1984.

[15] R. S. Rivlin. *Large elastic deformations of isotropic materials. IV. Further developments of the general theory.* hilos. Trans. Roy. Soc. Lond. Ser., 1948.

[16] R. Piazza. *Soft Matter Course Lecture Notes.* Politecnico di Milano, 2020.

[17] R. Dargazany, V. N. Khiêm, and M. Itskov. A generalized network decomposition model for the quasi-static inelastic behavior of filled elastomers. *International Journal of Plasticity*, 63:94–109, 2014.

[18] J.T Bauman. *Fatigue, Stress, and Strain of Rubber Components.* Hanser Publications, 2008.

[19] V. S. Papkov and Y. K. Godovskii. Energy investigation of the softening of siloxane rubbers. *Polymer Mechanics*, 11(3):329–333, 1975.

[20] H. Lorenz and M. Klüppel. Microstructure-based modelling of arbitrary deformation histories of filler-reinforced elastomers. *Journal of the Mechanics and Physics of Solids*, 60(11):1842–1861, 2012.

[21] L. Mullins. Softening of rubber by deformation. *Rubber Chemistry and Technology*, 42(1):339–362, 1969.

[22] L. Mullins and N. R. Tobin. Theoretical model for the elastic behavior of filler-reinforced vulcanized rubbers. *Rubber Chemistry and Technology*, 30(2):555–571, 1957.

[23] R. Houwink. Slipping of molecules during the deformation of reinforced rubber. *Rubber Chemistry and Technology*, 29(3):888–893, 1956.

[24] L. Mullins. Effect of stretching on the properties of rubber. *Journal of Rubber Research*, 16(2):281–300, 1947.

[25] G. Machado, G. Chagnon, and D. Favier. Experimental observation of induced anisotropy of the mullins effect in particle-reinforced silicone rubber. *Constitutive Models for Rubber VI*, pages 511–515, 2009.

[26] J. Diani, B. Fayolle, and P. Gilormini. A review on the mullins effect. *European Polymer Journal*, 45(3):601–612, 2009.

[27] G. Kraus, C. W. Childers, and K. W. Rollmann. Stress softening in carbon black-reinforced vulcanizates. strain rate and temperature effects. *Applied Polymer Science*, 10(2):229–244, 1966.

[28] D. E. Hanson, M. Hawley, R. Houlton, K. Chitanvis, P. Rae, E. B. Orler, and D. A. Wrobleski. Stress softening experiments in silica-filled polydimethylsiloxane provide insight into a mechanism for the mullins effect. *Polymer*, 46(24):10989–10995, 2005.

[29] Y. Fukahori. New progress in the theory and model of carbon black reinforcement of elastomers. *Journal of Applied Polymer Science*, 95(1):60–67, 2004.

[30] L. Mullins. Permanent set in vulcanized rubber. *Rubber Chemistry and Technology*, 22(4):1036–1044, 1949.

[31] S. R. Rickaby and N. H Scott. Transversely isotropic cyclic stress-softening model for the mullins effect. *Proceedings of the Royal Society A: Mathematical, Physical and Engineering Sciences*, 468(2148):4041–4057, 2012.

[32] A. Dorfmann and R. W. Ogden. A constitutive model for the mullins effect with permanent set in particle-reinforced rubber. *International Journal of Solids and Structures*, 41(7):1855–1878, 2004.

[33] R. Andrews, A. Tobolsky, and E. Hanson. The theory of permanent set at elevated temperatures in natural and synthetic rubber vulcanizates. *Journal of Applied Physics*, 19(4):1099–1112, 1946.

[34] A. Tobolsky and R. Andrews. Systems manifesting superposed elastic and viscous behavior. *The Journal of Chemical Physics*, 13(1):3–27, 1945.

[35] H. Pouriayevali, Y. B Guo, and V. P. W. Shim. A constitutive description of elastomer behaviour at high strain rates - a strain-dependent relaxation time approach. *International Journal of Impact Engineering*, 47:71–78, 2012.

[36] M. S. H. Fatt and X. Ouyang. Integral-based constitutive equation for rubber at high strain rates. *International Journal of Solids and Structures*, 44(20):6491–6506, 2007.

[37] T. Tada, K. Urayama, T. Mabuchi, K. Muraoka, and T. Takigawa. Nonlinear stress relaxation of carbon black-filled rubber vulcanizates under various types of deformation. *Journal of Polymer Science: Part B - Polymer Physics*, 48(12):1380–1387, 2010.

[38] S. Farzaneh, J. Fitoussi, A. Lucas, W. Bocquet, and A. Tcharkhtchi. Shape memory effect and properties memory effect of polyurethane. *Journal of Applied Polymer Science*, 125(5):3240–3249, 2013.

[39] R.N. Rothon. *Particulate Fillers for Polymers*. Smithers Rapra Technology, 2001.

[40] X. Li, T. Bai, Z. Li, and L. Liu. Influence of the temperature on the hyper-elastic mechanical behavior of carbon black filled natural rubbers. *Mechanics of Materials*, 95:136–145, 2016.

[41] S. Krpovic, K. Dam-Johansen, and A. L. Skov. Importance of mullins effect in commercial silicone elastomer formulations for soft robotics. *Journal of Applied Polymer Science*, 138(19):50380, 2020.

[42] Z. Liao, M. Hossain, and Y. Xiaohu. Ecoflex polymer of different shore hardnesses: Experimental investigations and constitutive modelling. *Mechanics of Materials*, 144:103366, 2019.

[43] Z. Liao, J. Yang, M. Hossain, G. Chagnon, L. Jing, and Y. Xiaohu. On the stress recovery behaviour of ecoflex silicone rubbers. *International Journal of Mechanical Sciences*, 206:106624, 2021.

[44] Smooth-On Inc. Ecoflex series data sheet. Technical report, https://www.smooth-on.com/products/ecoflex-00-50/, 2019.

[45] S. Lee and M. Pharr. Sideways and stable crack propagation in a silicone elastomer. *Proceedings of the National Academy of Sciences*, 116(19):9251–9256, 2019.

[46] G. Camino, S.M. Lomakin, and M. Lazzari. Polydimethylsiloxane thermal degradation part 1. kinetic aspects. *Polymer*, 42(6):2395–2402, 2000.

[47] A. Ručigaj, M. Krajnc, and U. Šebenik. Kinetic study of thermal degradation of polydimethylsiloxane: The effect of molecular weight on thermal stability in inert atmosphere. *Polymer Sciences*, 3(2), 2017.

[48] S. Doti, A. Galesso, M. Ghidoli, C. Giacalone, A. Pulici, and S. Scolari. *Cosa succede quando si stira un elastomero? Applicazione di analisi spettroscopica per comprendere il meccanismo alla nanoscala*. Bachelor degree thesis, Politecnico di Milano, 2021.

[49] EN ISO 527-2:2012. *Plastics - Determination of tensile properties - Part 2: Test conditions for moulding and extrusion plastics.*

[50] R. Calabrò. *Mechanical characterization of elastomers under quasi-static and dynamic biaxial loading conditions.* PhD thesis, Politecnico di Milano, 2013.

[51] M. A. Sutton, J.J. Orteu, and H. W. Schreier. *Image correlation for shape, motion and deformation measurements.* Springer, 2009.

[52] B. Pan, Z. Xie, H. ans Wang, K. Qian, and Z. Wang. Study on subset size selection in digital image correlation for speckle patterns. *Optics Express*, 16(10):7037–7048, 2008.

[53] L. A. Mihai and A. Goriely. How to characterize a nonlinear elastic material? a review on nonlinear constitutive parameters in isotropic finite elasticity. *Proceedings of the Royal Society A: Mathematical, Physical and Engineering Sciences*, 473(2207):20170607, 2017.

[54] L. R. G. Treloar. Stress-strain data for vulcanised rubber under various types of deformation. *Transactions of the Faraday Society*, 40:59, 1944.

[55] S. Dogru, B. Aksoy, H. Bayraktar, and B. E. Alaca. Poisson's ratio of pdms thin films. *Polymer Testing*, 69:375–384, 2018.

[56] O. H. Yeoh. Some forms of the strain energy function for rubber. *Rubber Chemistry and Technology*, 66(5):754–771, 1993.

[57] R.W. Ogden and D.G. Roxburgh. A pseudo–elastic model for the mullins effect in filled rubber. *Proceedings of the Royal Society of London. Series A: Mathematical, Physical and Engineering Sciences*, 455(1988):2861–2877, 1999.

[58] A. Dorfmann and R. W. Ogden. A pseudo-elastic model for loading, partial unloading and reloading of particle-reinforced rubber. *International Journal of Solids and Structures*, 40(11):2699–2714, 2003.

[59] T. Rey, G. Chagnon, J. B. Le Cam, and B. Favier. Influence of the temperature on the mechanical behaviour of filled and unfilled silicone rubbers. *Polymer Testing*, 32(3):492–501, 2013.

[60] T. L. Smith. Ultimate tensile properties of elastomers. i. characterization by a time and temperature independent failure envelope. *Polymer Science Part A: General Papers*, 1(12):3597–3615, 1963.

[61] T. L. Smith. Ultimate tensile properties of elastomers. ii. comparison of failure envelopes for unfilled vulcanizates. *Journal of Applied Physics*, 35(1):27–36, 1964.

[62] F. Beuche and J. C. Halpin. Molecular strength of the tensile strength of gum elastomers. *Journal of Applied Physics*, 35(1):36–41, 1964.

[63] J. C. Halpin. Fracture of amorphous polymeric solids: Time to break. *Journal of Applied Physics*, 35(11):3133–3141, 1964.

[64] G. M. Martin, F. L. Roth, and R. D. Stiehler. Behavior of pure-gum rubber vulcanizates in tension. *Rubber Chemstry and Technology*, 30(3):876–888, 1957.

[65] M. Contino, L. Andena, M. Rink, G. Marra, and S. Resta. Time-temperature equivalence in environmental stress cracking of high-density polyethylene. *Engineering Fracture Mechanics*, 203:32–43, 2018.